MATERIALS AND PROCESSING TECHNIQUES FOR SUPERCAPACITORS

SYNTHESIS AND PROCESSING TECHNIQUES OF ADVANCED ELECTRODE MATERIALS FOR SUPERCAPACITOR APPLICATIONS

By JORDAN MILNE, B.Eng

A Thesis Submitted to the School of Graduate Studies in Partial Fulfilment of the Requirements for the Degree Master of Applied Science

McMaster University

McMaster University MASTER OF APPLIED SCIENCE (2019) Hamilton, Ontario (Materials Science & Engineering)

TITLE: Synthesis and Processing Techniques of Advanced Electrode Materials for Supercapacitor Applications

AUTHOR: Jordan Milne, B.Eng. (McMaster University)

SUPERVISOR: Dr. Igor Zhitomirsky, Distinguished Engineering Professor, Ph.D., P.Eng.

NUMBER OF PAGES: 108

Abstract

In a world that relies heavily on electricity and portable energy, the development of high performing energy storage devices is crucial. The ongoing push for energy storage devices such as batteries and supercapacitors to store more energy and charge/discharge faster has become exponentially stronger over the past decade. In order to meet the high demands, new materials and processing techniques must be developed.

A particle extraction through the liquid-liquid interface (PELLI) technique was used with a versatile extracting molecule, Octyl Gallate (OG). It was found that OG was able to extract a variety of materials including oxides, oxyhydroxides, and pure silver. The advantage of PELLI is that it circumvents the drying stage that occurs in many electrode synthesis techniques where metal oxides are synthesized in aqueous then dried and mixed with conductive additives dispersed in organic solvent. This drying stage causes a practically irreversible agglomeration which hinders mixing with conductive additives as well as reduces the surface area of the material, limiting its electrochemical performance. Using hydroxamates such as octanohydroxamic acid and bufexamac, a novel PELLI technique was developed based on the use of OHA as an extracting agent as well as a capping agent.

In addition, a preliminary investigation was started on advanced negative electrode material for supercapacitors. FeOOH-based electrodes exhibit high capacitance but low cyclic stability. Zn^{2+} ions were introduced during synthesis forming a doped Zn/FeOOH electrode which showed a significant increase in cyclic stability.

Acknowledgements

Firstly, I would like to recognize my supervisor Dr. Igor Zhitomirsky for his kind demeanour and seemingly endless pool of knowledge in chemistry and material science.

My lab mates Ryan Poon, Ricardo Silva, Amanda Clifford, and Aseeb Syed thank you for making everyday a little more entertaining. I am very grateful to my love Kathryn Passalent for giving me a wonderful life outside of graduate school.

Finally, I would like to thank my Mom, Dad, and sister for their endless support and encouragement.

Table of Contents

Table of Figures

Table of Tables

Table of Abbreviations and Symbols

Abbreviations

[Ox]	Concentration of **Ox**idized Species
[Red]	Concentration of **Red**uced Species
AC	**A**ctivated **C**arbon
CBD	**C**hemical **B**ath **D**eposition
CNT	**C**arbon **N**anotubes
CV	**C**yclic **V**oltammetry
EDLC	**E**lectrostatic **D**ouble-**L**ayer **C**apacitor
EIS	**E**lectrochemical **I**mpedance **S**pectroscopy
EPD	**E**lectro**p**horetic **D**eposition
ESR	**E**quivalent **S**eries **R**esistance
FTIR	**F**ourier **T**ransform **I**nfra**r**ed Spectroscopy
GCD	**G**alvanostatic **C**harge-**D**ischarge
IR loss/drop	**I** – current, **R** – resistance
LLI	**L**iquid-**L**iquid **I**nterface
MWCNT	**M**ulti-**W**all **C**arbon **N**ano**t**ubes
PELLI	**P**article **E**xtraction through the **L**iquid-**L**iquid **I**nterface
rGO	**R**educed **G**raphene **O**xide
SCE	**S**aturated **C**alomel **E**lectrode
SEM	**S**canning **E**lectron **M**icroscopy
XPS	**X**-Ray **P**hotoelectron **S**pectroscopy
XRD	**X**-**R**ay **D**iffraction

Symbols

°C	Degrees Celsius
A	Area
C	Capacitance
d	distance
F	Farad
g	Gram
I	Current
k	Boltzmann Constant
Q	Charge
$\bar{\mathbf{R}}$	Gas Constant
R	Resistance
T	Temperature
V	Volt
W	Watt
Z	Impedance

Declaration of Academic Achievement

This dissertation was used to fulfill the requirements of the degree: Master of Applied Science. The major research project ran from May 2017 to April 2019. The content of this dissertation was covered in three papers in which I was first author, published in peer-reviewed journals:

1. **J. Milne** and I. Zhitomirsky, "Application of octanohydroxamic acid for liquid-liquid extraction of manganese oxides and fabrication of supercapacitor electrodes," *J. Colloid Interface Sci.*, vol. 515, pp. 50–57, 2018.
2. **J. Milne**, R. M. E. Silva, Z. Z. Wang, and I. Zhitomirsky, "Phase transfer of oxide particles using hydroxamic acid derivatives and application for supercapacitors," *Ceram. Int.*, vol. 45, no. 2, pp. 2498–2503, 2018.
3. **J. Milne**, R. Marques Silva, and I. Zhitomirsky, "Surface modification and dispersion of ceramic particles using liquid-liquid extraction method for application in supercapacitor electrodes*," J. Eur. Ceram. Soc.*, IN PRESS

I also contributed to four additional papers, published in peer-reviewed journals, that will not be covered in this dissertation:

1. R. M. E. Silva, R. Poon**, J. Milne**, A. Syed, and I. Zhitomirsky, "New developments in liquid-liquid extraction, surface modification and agglomerate-free processing of inorganic particles," *Adv. Colloid Interface Sci.*, vol. 261, pp. 15–27, 2018.
2. M. S. Ata, R. Poon, A. M. Syed, **J. Milne**, and I. Zhitomirsky, "New developments in non-covalent surface modification, dispersion and electrophoretic deposition of carbon nanotubes," *Carbon N. Y.*, vol. 130, pp. 584–598, 2018.

3. M. S. Ata, **J. Milne**, and I. Zhitomirsky, “Fabrication of Mn3O4–carbon nanotube composites with high areal capacitance using cationic and anionic dispersants,” *J. Colloid Interface Sci.*, vol. 512, pp. 758–766, 2018.
4. R. M. Silva, B. S. Noremberg, N. H. Marins, **J. Milne**, I. Zhitomirsky, and N. L. V Carreño, “Microwave-assisted hydrothermal synthesis and electrochemical characterization of niobium pentoxide / carbon nanotubes composites,” *J. Mater. Res.*, pp. 1–8, 2018.
5. Z.Wang, A. Clifford, , **J. Milne**, I. Zhitomirsky, “Colloidal-electrochemical fabrication strategies for linear polyethylenimine composites,” *J. Colloid Interface Sci,* SUBMITTED

Chapter 1: Introduction

As a result of the escalating energy demands of modern society paired with intensifying environmental concerns, it has become necessary to discover and further develop advanced materials for energy storage systems. Some of the most practical and effective technologies for storage and conversion of electrochemical energy are electrochemical supercapacitors, batteries, and fuel cells.

Electrochemical supercapacitors, also called ultracapacitors or supercapacitors, are energy storage devices that bridge the gap between conventional capacitors and batteries. Supercapacitors have a power density above that of a battery while achieving an energy density above that of conventional capacitor, as seen in Figure 1-1[1]. This unique combination of power and energy density allows supercapacitors to be used in applications where neither battery nor capacitor are suitable, as well as applications where hybrid capacitor-battery systems are necessary.

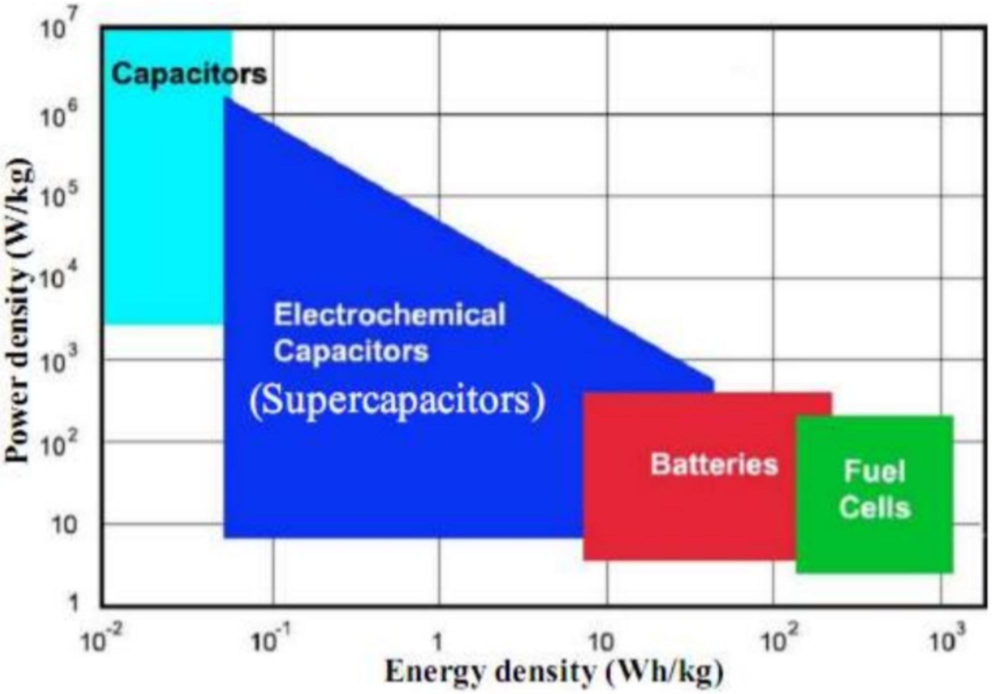

Figure 1-1: Ragone plot displaying power and energy densities of energy storage devices[1].

There are two types of supercapacitors: electrochemical double-layer capacitors (EDLCs) and pseudocapacitors, which are classified by their charge storage mechanisms. EDLCs store charge in a non-Faradaic manner that involves electrostatic charge accumulation and separation at the electrode/electrolyte interface of each electrode of the capacitor which results in what is called double-layer capacitance. Pseudocapacitors however, store charge by electron charge transfer from fast, highly reversible Faradaic redox reactions occurring at the surface and subsurface of the electrode resulting in pseudocapacitance.

The material in a supercapacitor electrode that contributes to charge storage is termed as the active material. A variety of active materials can be used for positive and negative electrodes of supercapacitors. High surface area carbon derivatives have dominated as active materials for EDLC type supercapacitors, as the amount of charge is proportional to surface area. Whereas transition metal oxides and hydroxides, as well as conducting polymers achieve exceptional pseudocapacitive performance and are becoming increasingly common in supercapacitors. Unfortunately, most oxides and hydroxides have intrinsically low electrical conductivity so high capacitances can only be achieved by thin film electrodes. In addition, metal oxides and hydroxides tend to agglomerate during drying after particle synthesis, resulting in the particle surface area becoming inaccessible to electrolyte and other electrode material additives.

Over the last decade, the majority of supercapacitor research and improvements have been on positive electrode materials, leaving the negative electrode to become the limiting factor of device performance. Activated carbon is a common negative electrode for supercapacitors[2] but it has a lower capacitance compared to the positive electrode in addition to being expensive. FeOOH is a promising negative electrode material due to its high capacitance[3] but its poor cycle life renders it impractical for commercial application.

The objective of this research was to develop a novel processing technique for the synthesis of non-agglomerated particles to enhance supercapacitor performance as well as to develop an advanced negative electrode material for asymmetric supercapacitors all with high active mass loadings. An innovative colloidal processing technique was developed that used a multifunctional molecule that acted as a capping agent and a dispersing agent.

The conceptually new approach resulted in reduced particle size and improved mixing with conductive additives giving exceptional electrochemical performance. In addition, a new negative electrode material was developed via doping FeOOH with Zn that exhibited impressive cyclic stability.

Chapter 2: Literature Review

2.1 Fundamentals of Conventional Capacitors

In energy storage applications, capacitors predate the invention of the battery. The first capacitor was built at the University of Leyden in the mid 1700s using a glass jar coated inside and out with silver foil[4]. A brief review of the fundamentals of simple conventional capacitors is necessary as the governing equations and principles carry into the more complex capacitor types. Figure 2-1 shows a simple capacitor that consists of two parallel conducting plates and a dielectric in between[5].

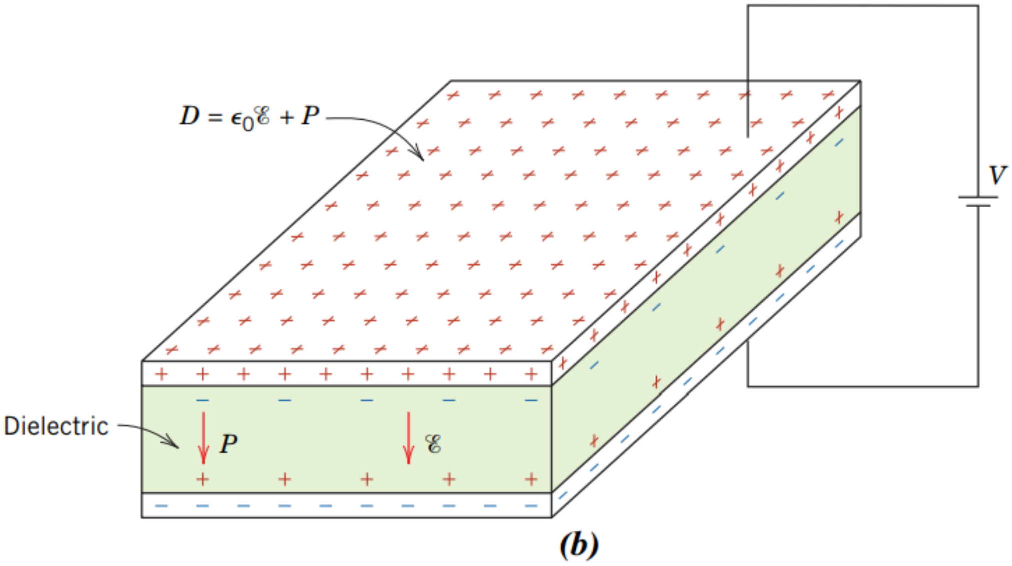

Figure 2-1: Diagram of a simple electrostatic capacitor.

In order for electrostatic charge to develop on the plate/electrodes of the capacitor, work must be done by an external driving force such as applying a potential difference.

Initially, the net charge between the plates of the capacitor is zero. In Figure 2-1 a battery provides an electromotive force generating a flow of electrons from one of the electrodes of the capacitor to the positive terminal of the battery, making that electrode positively charged. Simultaneously, electrons flow from the negative terminal of the battery and accumulate on the other electrode of the capacitor, making that electrode negatively charged. The charging continues until the potential between the plates of the capacitor is equal to the applied potential from the battery and the charge on each electrode of the capacitor is equal and opposite. The ratio between the electric charge on each electrode (Q), and the potential difference between the electrodes (V), is denoted as capacitance (C), as seen in Eq. 2.1.

$$C = \frac{Q}{V} = \frac{\varepsilon_0 \epsilon_r A}{d} \tag{2.1}$$

For a simple parallel plate capacitor as shown above, capacitance is dependent on the area (A) of the electrodes, the permittivity of free space (ε_0), the dielectric constant of the material between the plates (ε_r), and the distance (d) between the two electrodes.

To calculate the work done by the potential to store charge in a capacitor, an equation can be developed using the relation between the amount of incremental work (dW) required for an incremental change in charge (dQ):

$$dW = VdQ \tag{2.2}$$

The integral of this equation results in the amount of energy the capacitor can hold. To simplify integration, we can use the relation between charge, capacitance, and potential and remove capacitance from inside the integral because capacitance remains constant which results in:

$$E = \int dW = \int VdCV = C\int VdV = \left(\frac{1}{2}\right)CV^2 \tag{2.3}$$

In addition, the power density of a capacitor can be written as:

$$P = \frac{V^2}{4R_{ESR}} \tag{2.4}$$

Where R_{ESR} is the equivalent series resistance (ESR). It is clear from these equations that both power and energy density can be increased by increasing the operating voltage. In addition, energy density can be increased by increasing the capacitance. Regarding the deliverable power supplied by the capacitor, the power density can also be increased by reducing the ESR. In summary, by increasing the capacitance as well as the operating voltage and reducing the resistance, energy and power density can be increased.

2.2Types of Supercapacitors

2.2.1 Electrochemical Double-Layer Capacitors

EDLCs differ from pseudocapacitors due to the different charge storage mechanisms[6]. Similar to conventional electrostatic capacitors, EDLCs also store charge in a non-Faradaic method, meaning there is no charge transfer or redox reactions[7]. EDLCs are comprised of two electrodes which are typically made of high surface area carbon materials such as activated carbon. The two electrodes are physically separated by an ion permeable separator but remain connected ionically via an electrolyte. The electrolyte consists of both positive and negative ions dissolved in a solvent such as water. When a voltage is applied across the electrodes of an EDLC, 'double-layers' are formed at each electrode involving the charge on the surface of the electrode and solvated dissolved ions of the opposite charge in the electrolyte. A monolayer of solvent molecules, such as water, separate these two layers and charge is stored electrostatically. EDLCs work on the same principle as conventional capacitors but take advantage of the astonishingly large surface area of activated carbon and the nanoscale distance between the electrode surface and electrolyte ion which in this case would be the diameter of a water molecule.

Regarding modelling the double-layer phenomenon, there have been a series of models through history that have been accepted then improved upon which eventually led to the most correct, Grahame Model[8]. The first model of the double-layer was developed by Helmholtz, Figure 2-2(a), which illustrates the distribution of opposite charges, quasi-2-dimensionally, at the electrode-electrolyte interface. Applying a potential causes a controllable amount of charge buildup on the electrode surface due to an excess or deficiency of electrons and a corresponding accumulation of oppositely charged ions in solution complete the double-layer. Figure 2-2(b) is the Gouy-Chapman model, which introduced two modifications, (1) assume the electrolyte ions are point charges, (2) the double-layer would be subject to thermal fluctuations according to the Boltzmann principle[9]. The next development in the double-layer theory was by Stern and is shown in Figure 2-2(c). In his model, Stern combined the Helmholtz and Gouy-Chapman model to overtly define two regions of ion distribution, the diffuse layer/region and the compact/Helmholtz layer.

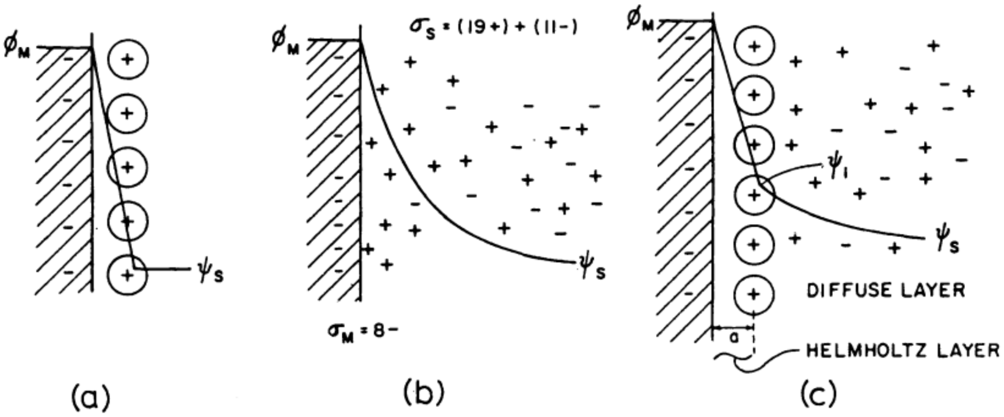

Figure 2-2: Models of the double-layer a) Helmholtz model, b) Gouy-Chapman model, and c) Stern model[9]

The Helmholtz layer containing a compact array of ions has a capacitance of C_H. The remaining ionic charge density past the Helmholtz layer is termed as the diffuse region, having a capacitance of C_{diff}. Combining these capacitances results in the overall double-layer capacitance (C_{dl}), governed by:

$$\frac{1}{C_{dl}} = \frac{1}{C_H} + \frac{1}{C_{diff}} \tag{2.5}$$

The Stern model was further improved by Grahame, as seen in Figure 2-3, who made an important distinction between an inner and outer Helmholtz layer due to the different distances of closest approach at the electrode surface for cations and anions.

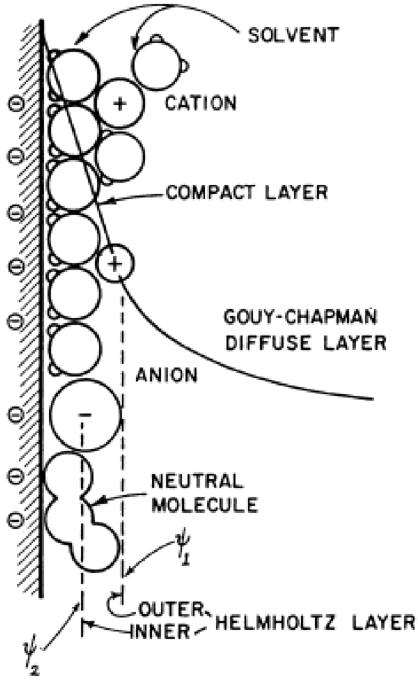

Figure 2-3: Grahame's representation of the double-layer structure defining different regions for adsorption of hydrated cations and less hydrated anions.[9]

Due to the fact that most cations have a stronger ion-solvent interaction, they retain a large solvation shell which hinders the accumulation of cations to the electrode interface increasing their distance of closest approach. This leads to anion distance of closest approach to usually be smaller than that of a cation's, causing the inner layer capacitance of positively charged electrodes to typically be higher than that of a corresponding negatively charged electrode surface[9].

2.2.2 Pseudocapacitors

Pseudocapacitors utilize extremely rapid and reversible Faradaic charge transfer reactions between the active material of the electrode and the ions from the electrolyte which gives a much larger energy density than that of EDLCs[10]. Although Faradaic by nature, the shape of the cyclic voltammograms (CV) of such devices are similar to that of capacitors – hence the name *pseudo*capacitance. Conway identified three Faradaic mechanisms that exhibit capacitive features: (1) redox pseudocapacitance, (2) underpotential deposition and (3) intercalation pseudocapacitance[9]. These mechanisms are displayed in Figure 2-4 [11]. Redox pseudocapacitance is a phenomenon that occurs when electrolyte ions are adsorbed onto the surface resulting in Faradaic charge transfer due to a redox reaction. Underpotential deposition arises when metal ions residing in the electrolyte solution form a monolayer on a different metal's surface above their redox potential. Intercalation pseudocapacitance is similar to that of Li-ion batteries and occurs when ions migrate into layers or tunnels of an electrode material’s lattice resulting in a highly reversible redox reaction without any crystallographic phase changes.

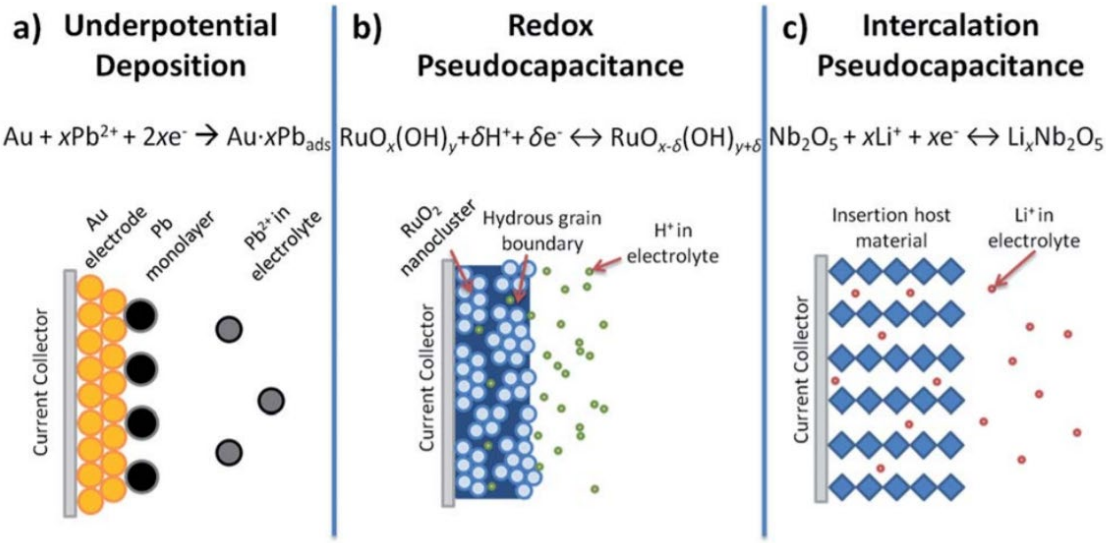

Figure 2-4: Different types of pseudocapacitive behaviour: (a) underpotential deposition, (b) redox pseudocapacitance, and (c) intercalation pseudocapacitance[12].

Each of the three examples above are mechanisms for an electron to be transferred between an oxidized species and a reduced species[9].

Thermodynamically, pseudocapacitance originates when some property β, that is proportional to charge passed caused by the conversion of a redox species, is related to potential expressed in this Arrhenius equation:

$$\frac{\beta}{1-\beta} = Ke^{\frac{zF}{RT}} \tag{2.6}$$

Since β is proportional to the charge passed the derivative of β, with respect to potential, dβ/dV, is related to a corresponding capacitance as:

$$\frac{d\beta}{dV} = \frac{F}{RT}\frac{Kexp\left(\frac{zF}{\bar{R}T}\right)}{\left[1 + Kexp\left(\frac{zF}{\bar{R}T}\right)\right]^2} \tag{2.7}$$

Conway continues to mention that this general equation above, Eq. 2.7, applies equivalently to the 3 pseudocapacitance mechanisms, however with a closer look it is realized that the Nernst equation is also suitable. For typical redox couple a simple redox reaction can be written as well as the corresponding Nernst equation:

$$Ox + ze^- \leftrightarrow Red \tag{2.8}$$

$$E = E^0 + \left(\frac{\bar{R}T}{zF}\right)\ln\frac{[Ox]}{[Red]} \tag{2.9}$$

Now, equation Eq. 2.8 can be rewritten using Q as a given molar quantity of reagent, Q = [Ox] + [Red]. If we rearrange Eq. 2.9 and write it in terms of [Ox] the result is:

$$\frac{\left[\frac{Ox}{Q}\right]}{1 - \left[\frac{Ox}{Q}\right]} = \exp\left(\frac{(E - E^0)F}{\bar{R}T}\right) = \exp\left(\frac{\Delta E \cdot F}{\bar{R}T}\right) \tag{2.10}$$

It is now more evident that the modified Nernst equation, Eq. 2.10, has the same structure as Eq. 2.6 and can be used as a universal function for this type of system. Conway provides an in-depth correlation of three types of systems that exhibit pseudocapacitance, which is summarized in Table 2-1.

Table 2-1: Types of pseudocapacitive systems and their corresponding Nernst type equations[9].

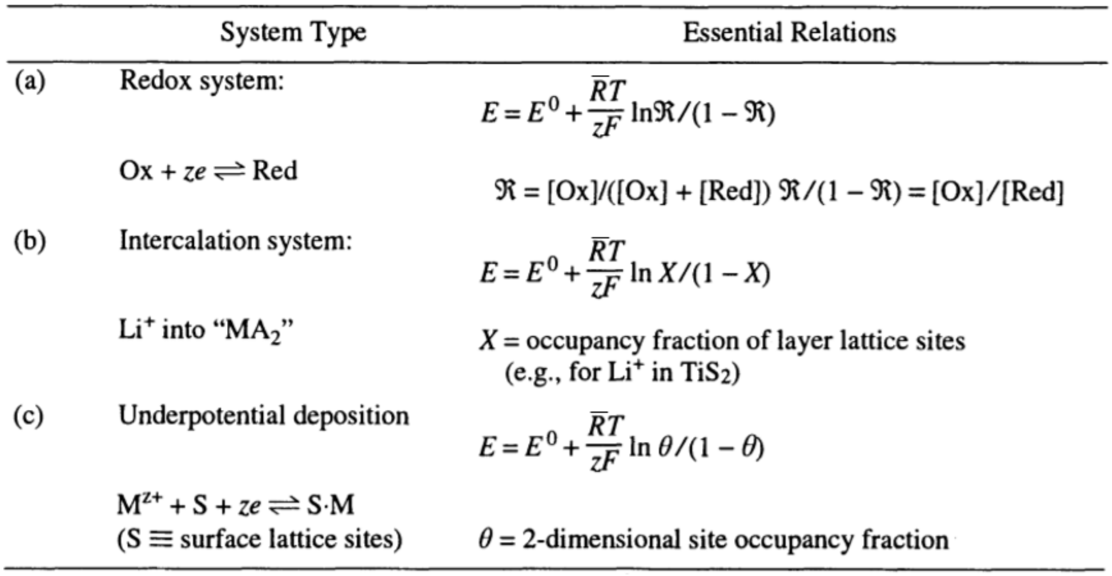

	System Type	Essential Relations
(a)	Redox system:	$E = E^0 + \frac{\bar{R}T}{zF} \ln \Re/(1-\Re)$
	$Ox + ze \rightleftharpoons Red$	$\Re = [Ox]/([Ox] + [Red])$ $\Re/(1-\Re) = [Ox]/[Red]$
(b)	Intercalation system:	$E = E^0 + \frac{\bar{R}T}{zF} \ln X/(1-X)$
	Li^+ into "MA_2"	X = occupancy fraction of layer lattice sites (e.g., for Li^+ in TiS_2)
(c)	Underpotential deposition	$E = E^0 + \frac{\bar{R}T}{zF} \ln \theta/(1-\theta)$
	$M^{z+} + S + ze \rightleftharpoons S \cdot M$ ($S \equiv$ surface lattice sites)	θ = 2-dimensional site occupancy fraction

2.3 Electrode Materials for Supercapacitors

This subchapter will discuss different supercapacitor electrode materials for both positive and negative electrodes in aqueous electrolytes. Qu et al.[13] completed a useful chart (Figure 2-5) of common electrode materials and the most promising will be discussed in the following sections.

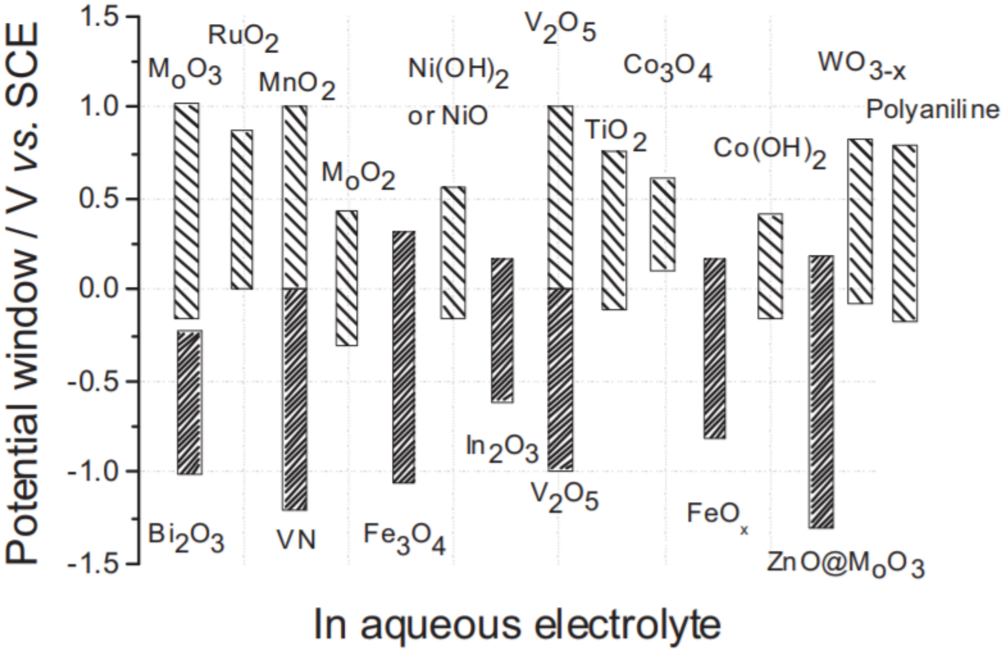

Figure 2-5: The potential windows of a variety of pseudocapacitive materials in aqueous electrolyte[13].

2.3.1 MnO_2

Manganese dioxide (MnO_2) is a promising positive electrode material as a result of its high theoretical capacitance (1370 F g^{-1}[12]), abundance, low cost, and environmentally benign nature. An in-depth insight of the charge storage mechanism of MnO_2 is of the utmost importance in order to understand the parameters that effect the charge storage process. MnO_2 stores charge mainly through redox and intercalation pseudocapacitive (Faradaic) reactions at the surface and subsurface of the material. MnO_2 is electrochemically active in the voltage window between 0 to 1.0 V (Vs. SCE) and exhibits an ideal rectangular shape during cyclic voltammetry. The redox reaction[14] that occurs in MnO_2 can be written as:

$$Mn(IV)O_2 + xC^+ + yH^+ + xe^- \leftrightarrow Mn(III)_{(x+y)}, Mn(IV)_{1-(x+y)}O_2C_xH_y \qquad (2.11)$$

Where C^+ is Li^+, Na^+, K^+, etc.

It is important to note that this reaction involves the incorporation of protons into the MnO_2 lattice which occurs reversibly and homogenously without any phase change[15]. This proton incorporation theory was solidified by Wen et al.[16] as their investigation included a series of experiments that focused on the effect of protons as well as cation species and respective concentrations. Wen et al. concluded that MnO_2 capacitance increases with increasing cation concentration up to a specific amount, albeit the difference between different alkaline species (Li, K, Na) showed little variation. On top of this, it was noted that the capacitance of MnO_2 drastically decreased in aprotic solvents when compared to water, rendering the effect of protons significant[16].

MnO_2 can exist in a variety of different crystallographic forms such as: α-MnO_2, β-MnO_2, γ-MnO_2, δ-MnO_2, λ-MnO_2[17]. The α and γ phase include one-dimensional (1D) tunnels in their structures whereas the δ phase is a 2D layered compound and the λ phase possesses a 3D spinel structure, which are all shown in Figure 2-6. In the previous section three types of pseudocapacitance were described: underpotential deposition, redox, and intercalation. The crystal structure has a significant effect on the intercalation/deintercalation of cations and in MnO_2[18]. Brousse et al.[19] studied the capacitance of different phases of MnO_2. It was concluded that certain crystallographic structures provided suitable gaps or tunnels to accommodate cations and protons which resulted in high capacitance, such as δ-MnO_2.

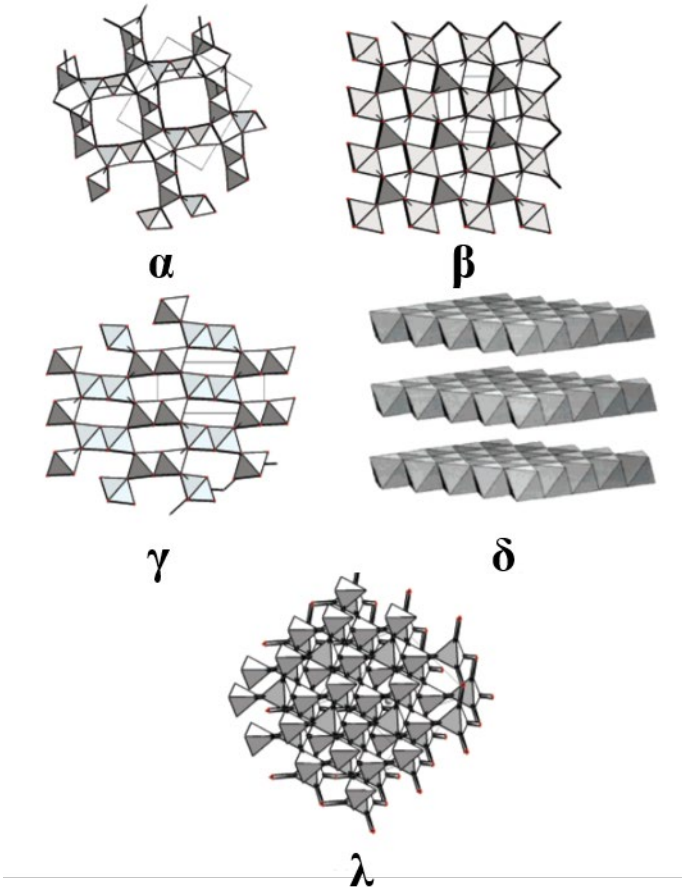

Figure 2-6: Crystal structures of α-, β-, γ-, δ-, and λ-MnO_2[17].

2.3.2 Mn_3O_4

It is known that manganese oxides can experience phase transformations during electrochemical cycling, resulting in an irreversible change in crystal structure causing a change in electrochemical performance[20][21]. In a recent study by Agrawal et al., anelectrostatic spray deposition was used to synthesize a thin film electrode of hausmannite-Mn_3O_4[22] . Agrawal reported a substantial increase in capacitance from 72 Fg^{-1} to 225 Fg^{-1} upon electrochemical cycling of the thin film Mn_3O_4 electrode, shown in Figure 2-7. The change in resistance and capacitance was attributed to the electrochemical phase transformation from the hausmannite-Mn_3O_4 to the more conducting birnessite-MnO_2, subsequently improving kinetics and conductivity[22]

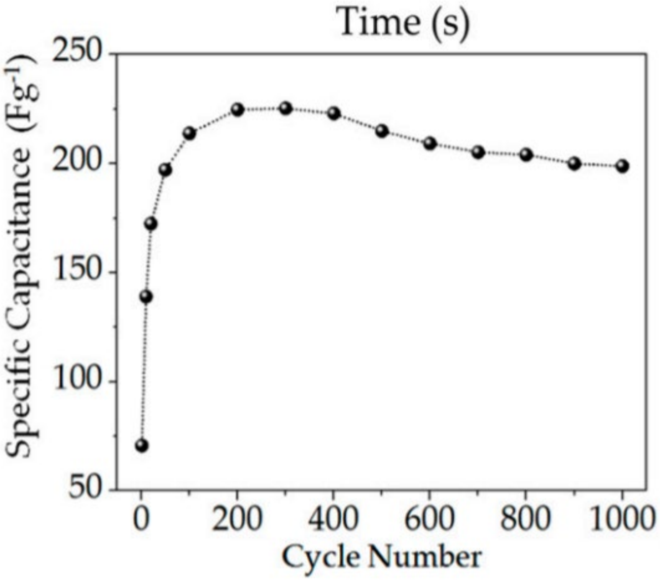

Figure 2-7: Cycling behavior of the Mn_3O_4 electrode[22].

Another major benefit of the electrochemical transformation from hausmannite-Mn_3O_4 to birnessite-MnO_2 is the variety of synthesis procedures available for Mn_3O_4 that are impractical for MnO_2 synthesis, specifically, the use of capping agents. It is well known that large agglomerated particles are detrimental to the performance of most energy storage devices, so nanoparticles and nanostructures have gained immense research attention[23]. Zhao et al. used poly(acrylic acid) as a capping agent for Mn_3O_4 and achieved an average particle size of 9.7 nm[24]. This highlights the weakness of the strong oxidizing precursor $KMnO_4$, that is practically unavoidable for synthesizing pseudocapacitive birnessite-MnO_2. $KMnO_4$ reacts strongly with organics, rendering additives such as capping agents during synthesis ineffective.

2.3.3 FeOOH

FeOOH is an iron oxyhydroxide that is used in many applications such as catalysts, electrode materials, and magnetic recording media. FeOOH is low cost, environmentally friendly, and offers pseudocapacitive behavior in aqueous electrolytes[25]. The charge storage mechanism can be written as the following[26]:

$$FeOOH + H_2O + e^- \leftrightarrow Fe(OH)_2 + OH^- \tag{2.12}$$

The charge/discharge process involves the Fe^{3+}/Fe^{2+} redox reaction in Eq. 2.12 resulting in Faradaic charge storage. FeOOH is electrochemically active between -0.8 and 0 V (Vs. SCE) which allows FeOOH electrodes to work in tandem as negative electrodes paired with positive electrodes such as MnO_2[27].

It has been reported that the amorphous phase provides superior supercapacitive performance than that of its crystalline counterparts because the electrostatic forces during charging and discharging can be easily released in the amorphous electrodes due to their disordered structures[28]. A study by Li et al. demonstrated that amorphous phase $Ni(OH)_2$ exhibited superior electrochemical performance because of its high structural disorder[29]. This finding has led to an increase in research of amorphous oxide/hydroxide electrode material, specifically FeOOH. Until recently, FeOOH has been ignored as a potential electrode material for supercapacitors because of its naturally high electrical resistance and low cyclability. That being said, many studies have reported excellent cyclability, such as Cheng et al., reporting 96% capacitance retention after 800 cycles[30] in high molar KOH as the electrolyte. Although Cheng and other authors achieved excellent cyclic performance with FeOOH they highlighted a new problem, which is many high performance positive electrodes work best in neutral electrolytes[31], not highly basic or acidic electrolytes. It is crucial that both positive and negative electrodes exhibit good electrochemical performance in the same electrolyte.

2.3.4 Other Metal Oxides

Other noteworthy metal oxide materials are RuO_2, Co_3O_4, $NiO/Ni(OH)_2$, and V_2O_5. RuO_2 has been studied as a positive electrode for supercapacitors for many years and has outstanding pseudocapacitive performance in both crystalline and amorphous phases[32]. One major benefit RuO_2 has over most other oxides is it has potentially three redox couples corresponding to four stable redox states, Ru^{2+}/Ru^{3+}, Ru^{3+}/Ru^{4+} and Ru^{4+}/Ru^{6+}[33]. The charge storage mechanism of RuO_2 involves proton intercalation in acidic and alkaline electrolytes as shown in the following equation[34].

$$RuO_2 + xH^+ + xe^- \leftrightarrow RuOH_x \qquad (2.13)$$

A hydrated $RuO_2 \cdot xH_2O$ amorphous compound was found to have a specific capacitance of 768 F g^{-1}[35]. While RuO_2 has exceptional electrochemical performance, the cost of RuO_2 is a major barrier for the commercialization of this material[36].

Another interesting positive electrode material that has gained research attention is Co_3O_4 due to its redox pseudocapacitance, impressive reversibility, and extremely high theoretical specific capacitance of 3580 F g^{-1}[37]. The charge storage mechanism for cobalt oxide is from the redox reactions of Co^{2+}/Co^{3+} which is[38]:

$$Co_3O_4 + OH^- + H_2O \leftrightarrow 3CoOOH + e^- \tag{2.14}$$

$$CoOOH + OH^- \leftrightarrow CoO_2 + H_2O + e^- \tag{2.15}$$

Xiang et al. synthesized Co_3O_4/reduced graphene oxide (rGO) composite through hydrothermal methods[39]. The authors reported a high specific capacitance of 472 F g^{-1} and 96% retention after 1000 cycles. An even more impressive result was then reported by Kumar et al. who synthesized graphene wrapped cobalt oxide via microwave irradiation forming a robust device with an impressive specific capacitance of 712 F g^{-1}[40]. Although Co_3O_4 has very high stability and capacitance values, it is limited not only by its high price, but also its high toxicity.

Nickel oxides and hydroxides are other well researched positive supercapacitor electrode materials. Nickel-based electrode materials are becoming more common in energy storage devices, specifically in supercapacitor research due to their higher theoretical capacitance, charge density, and chemical stability[41]. NiO and $Ni(OH)_2$ have similar charge/discharge mechanisms as FeOOH as they involve redox reactions with hydroxide groups as shown respectively[42], [43]:

$$NiO + zOH^- \leftrightarrow zNiOOH + (1 - z)NiO + ze^- \tag{2.16}$$

$$\alpha - Ni(OH)_2 \ + \ OH^- \leftrightarrow \gamma - NiOOH \ + \ H_2O + e^- \tag{2.17}$$

NiO has been synthesized in a plethora of ways including: heat treatment of electrodeposited nickel oxides/hydroxides[44], sol-gels[45], and precipitation[46]. Dar et al. used a thermally treated electrodeposition method to synthesize a thin film electrode resulting in the highest recorded specific capacitance for NiO of 2093 F g^{-1}[47]. Chai et al. used a chemical precipitation and ultrasonication with rGO to synthesize a $Ni(OH)_2$-rGO composite electrode which attained an impressive specific capacitance of 2053 F g^{-1}[43].

Another material of particular interest is V_2O_5, due to the structure of its valence electron layer, which can be written as $3d^34s^2$. This electron configuration has five valence electrons which can participate in bonding and provide impressive pseudocapacitance[48]. These multiple valence states give an unusually large potential window range seen in Figure 2-5. In addition to the large potential window, V_2O_5 is low cost, abundant, and has high theoretical pseudocapacitance (2120 F g^{-1})[49]. Pan et al. took advantage of the quasi-metallic phase of vanadium oxide, V_2O_3, which has a resistance lower than that of V_2O_5 by over 6 orders of magnitude shown in Figure 2-8[50].

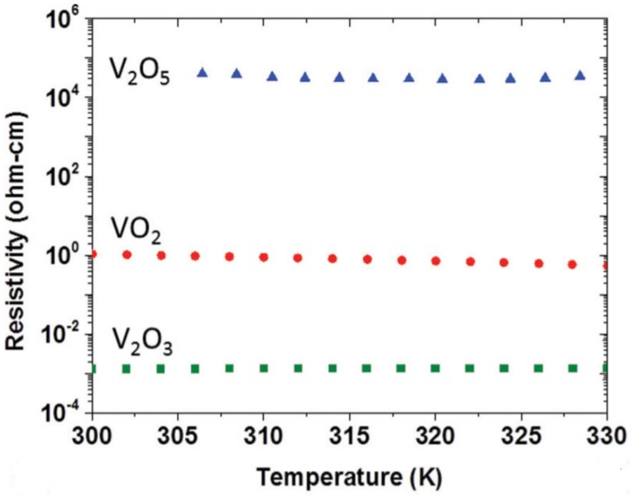

Figure 2-8: Representative resistivity of V_2O_5, VO_2, and V_2O_3[50].

Pan et al. fabricated V_2O_3/V_2O_5 core-shell nanostructures by synthesizing V_2O_3 particles in which the surface of these particles naturally oxidizes to a more stable 4^+ or 5^+ state, which also happens to have superior pseudocapacitive properties. V_2O_5 stores charge through pseudocapacitive redox reactions as well as intercalation which can be written as[51]:

$$V_2O_5 + xC^+ + xe^- \leftrightarrow V_2O_5C_x \tag{2.18}$$

A remarkably high specific capacitance of 2590 F g^{-1} was reported by Shakir et al. in thin films deposited using a layer-by-layer technique. One layer consisted of multi-walled carbon nanotubes (MWCNT) with an ultra thin film (3 nm) of V_2O_5 grown on them while a graphene layer was alternatively inserted[52].

2.3.5 Carbon Materials

A variety of carbon-based materials ranging from carbon nanotubes (CNT) to activated carbon (AC) are the most widely used EDLC electrodes and are common among other types of supercapacitors as well[53]. On top of being the sixth most abundant element in the earth's crust, most carbonaceous materials are highly conductive and can achieve enormously high specific surface area[54]. Carbon-based supercapacitors can store impressive amounts of energy through the utilization of the large surface area (A), combined with the atomic range of charge separation distances (d), explained in Eq. 2.1[55]. Carbon electrodes offer high power density, excellent cycle life, and excellent dependability[56]. However, their main drawbacks are low energy density and high self discharge[57].

Over the last decade, graphene and reduced graphene oxide have been heavily researched and show promising potential for supercapacitor applications. Graphene is a two-dimensional structure (one carbon atom in thickness) that is remarkably conductive as well as chemically stable, resulting in excellent energy storage capability[58]. rGO has the ability to introduce surface functional groups including alcohols, epoxides, carbonyls and carboxylic acids which can act as redox sites and contribute to pseudocapacitance[59]. A study by Wu et al. displayed a synergistic performance improvement when coupling rGO with RuO_2. Wu anchored RuO_2 nanoparticles on rGO surface via a precipitation method. Wu reported superior capacitance from the RuO_2–rGO composite compared to the results of pure rGO or pure RuO_2. The authors concluded that the rGO sheets aided in separating in separating the RuO_2 nanoparticles, avoiding the agglomeration of the RuO_2 nanoparticles while simultaneously providing a conductive pathway[60].

2.3.6 Conductive additives

A common factor in the aforementioned electrode materials is conducting additives. Homogenous electrode materials give inadequate performance due to their intrinsically weaker material properties such as conductivity, cyclic and mechanical stability, unless expensive and/or unscalable nanosynthesis techniques are used[61]. Most metal oxides are electrically resistive by nature[62], increasing both sheet resistance and charge transfer resistance causing a notable IR loss at higher current densities. The rapidly evolving field of nanotechnology has provided an impetus for advancements in supercapacitor electrode materials. A variety of carbon materials such as activated carbon[63], graphene[64], reduced graphene[65], and carbon nanotubes[66] are used in composite metal oxide electrodes to enhance conductivity and mechanical strength. Zhao et al. synthesized nanostructured graphene/NiO material for high performance composite supercapacitor electrodes[67]. As shown in Figure 2-9, Zhao increased the capacitance of pure NiO by 172% by adding a graphene matrix improving the conductivity of the composite.

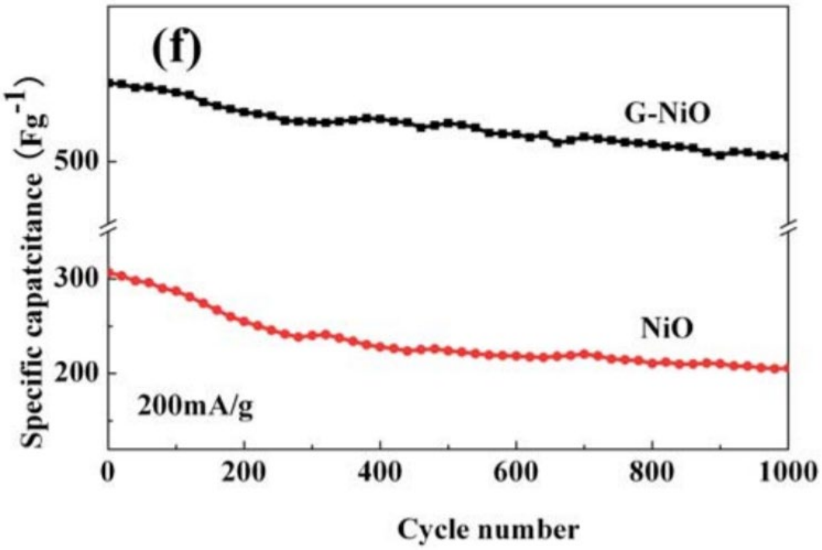

Figure 2-9: Specific capacitance over 1000 cycles of pure NiO and graphene/NiO[67].

MWCNT is another conducting material used to mitigate the conductivity problem that persists in most metal oxides owing to MWCNT's large surface area, superior conductivity and intertwined mesoporous structure[68]. Xia et al. investigated hydrothermally synthesized MnO_2 deposited onto MWCNT which resulted in a specific capacitance of 310 F g^{-1} and improved rate capability which significantly exceeds that of pure MnO_2 or pure MWCNT. The improved rate capability and capacitance of the MnO_2/MWCNT composite electrode over that of the pure MnO_2 electrode is due to the lower charge transfer resistance and diffusion related resistance reported in Xia's electrochemical impedance spectroscopy (EIS) analysis. Xia et al. concluded that the 3D electron path network provided by the MWCNT facilitate faster electron transport and mechanical stability.

2.4 Asymmetric Supercapacitors

In order to fully appreciate the potential of asymmetric supercapacitors, an understanding of electrolyte selection is necessary. Firstly, electrolytes used in supercapacitor applications should ideally be inexpensive and have: stability over a wide potential range, high ionic conductivity, low toxicity, as well as a small solvated ionic radius [69]. The most important property of the electrolyte is its stability over a potential range since the energy storage in supercapacitors is proportional to the square of applied voltage (Eq. 2.3). It is well known that the thermodynamic potential window of water is 1.23 V, restricting the use of aqueous electrolytes for commercialized “symmetric” supercapacitor technology (two identical carbon electrodes). For this reason, organic electrolytes have been commercially used for EDLC type devices as organic electrolytes are stable above 2.5 V[70].

Moreover, an asymmetric supercapacitor is a device that consists of two dissimilar electrodes that are electrochemically active in different potential windows[71]. Until recently, asymmetric supercapacitors were not well researched, as seen in Figure 2-10.

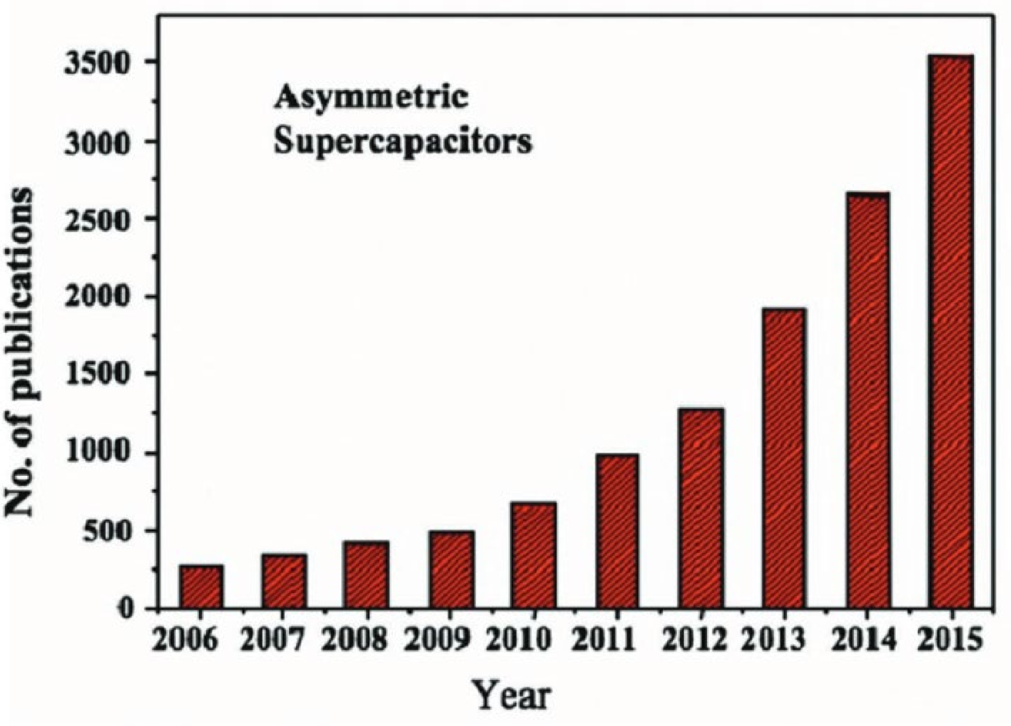

Figure 2-10: Asymmetric supercapacitor publications since 2006[71].

The driving force of this exponential increase in research of asymmetric supercapacitors is due to the high energy density achieved by pseudocapacitors in various potential ranges. The potential windows of the positive and the negative electrodes are limited by the oxygen and the hydrogen evolution reactions in aqueous electrolytes. Careful selection of positive and negative electrodes with high overpotentials allow aqueous-based asymmetric supercapacitors to achieve a voltage up to 2 V, eliminating the main advantage organic electrolytes hold.[72]. Other advantages of using aqueous electrolytes are they have low ESR, are cost-effective, and eco-friendly[73].

Unfortunately, a major roadblock for the development of asymmetric supercapacitors is the inferior capacitances of negative electrode materials, displayed in

Figure 2-11. The low capacitance of the negative electrode leads to low capacitance of the cell (C_{cell}) according to the fundamental equation, where C_+ and C_- are specific capacitances of positive and negative electrodes respectively[69]:

$$\frac{1}{C_{cell}} = \frac{1}{C_+} + \frac{1}{C_-} \tag{2.19}$$

It is clear that in order to fabricate practical asymmetric supercapacitors improved negative electrode materials are necessary.

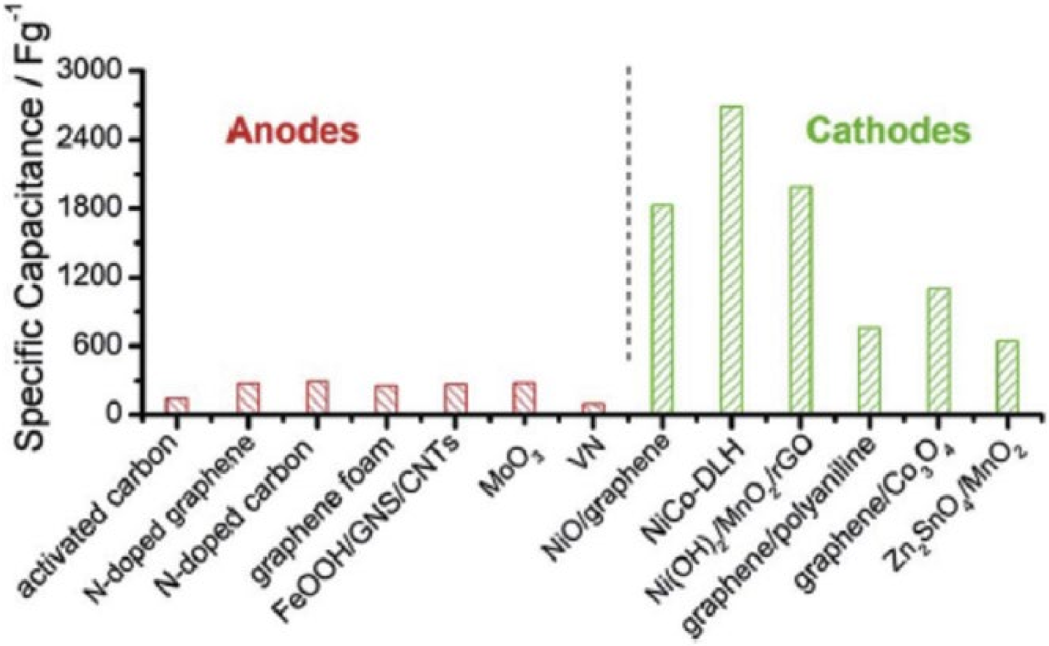

Figure 2-11: Specific capacitance of selected anode and cathode materials[69].

2.5 Mass Loading

Although the specific capacitances reported in the previous subchapters are impressive, there is a fundamental problem that must be addressed. Supercapacitor electrodes and devices reporting exceptional electrochemical performances typically have a mass loading of active material (pseudocapacitive material) less than 0.2 mg cm^2[74]. Since pseudocapacitive reactions occur mostly at the surface, electrolyte ions have easy access and short diffusion distance to active material of thin film (low mass loading) electrodes. For this reason, low mass loading electrodes have high specific capacitance and rate capability results. More importantly, low mass loading electrodes have low areal capacitance and low areal energy and power densities restricting their practicality in supercapacitors for energy storage applications[75]. In addition, an important characteristic of supercapacitor electrodes is the ratio (R_m) of active mass to the mass of the current collector[76]. Many thin film electrodes have micrograms of active material on heavy metallic current collectors.

$$R_m = \frac{mass\ of\ active\ material}{mass\ of\ current\ collector} \tag{2.20}$$

R_m values for thin film electrodes are typically below 1–2%, but for practical applications this percentage must be much higher[77].

2.6 Fabrication Methods

A major challenge in supercapacitor electrode fabrication is to achieve high capacitance, capacitance retention at high charge-discharge rates, and adequate cycle life for electrodes with high active mass loadings[78]. In order to synthesize high performing practical supercapacitor electrodes with high mass loadings, innovative fabrication methods must be utilized to synthesize composite electrode materials. These fabrication methods will be discussed in the following subchapters.

2.6.1 Electrophoretic Deposition

An electrode fabrication technique that is used for a variety of electrode materials is electrophoretic deposition (EPD). This method uses an electric field which moves charged particles towards an electrode serving as the deposition surface[79]. EPD is an established, economical, and scalable process that has been successfully used for the deposition of activated carbon, CNT, graphene, and transition metal oxides. EPD has numerous advantages for the fabrication of films from charged colloidal suspensions, including controllable thickness, high deposition rates, uniformity, and simplicity in terms of equipment[80].

A major catalyst for the increased use of electrophoretic deposition for supercapacitor electrodes stems from the power density equation Eq. 2.4, where minimizing the ESR increases the power density. Du et al. used EPD to deposit MWCNT which resulted in a uniform deposition that was efficiently bonded to the current collector[81]. This produced a direct conductive path from MWCNT film to the current collector, reducing contact and internal resistance of the electrode. An interesting study by An et al. reported a simple, high yield, large surface area, inexpensive, and environmentally benign fabrication of films comprised of rGO platelets using EPD shown in Figure 2-

21[82]. The oxygen functional groups of rGO were substantially removed by the EPD process, and the deposited film displayed improved electrical conductivity compared to rGO papers made by the filtration method[83].

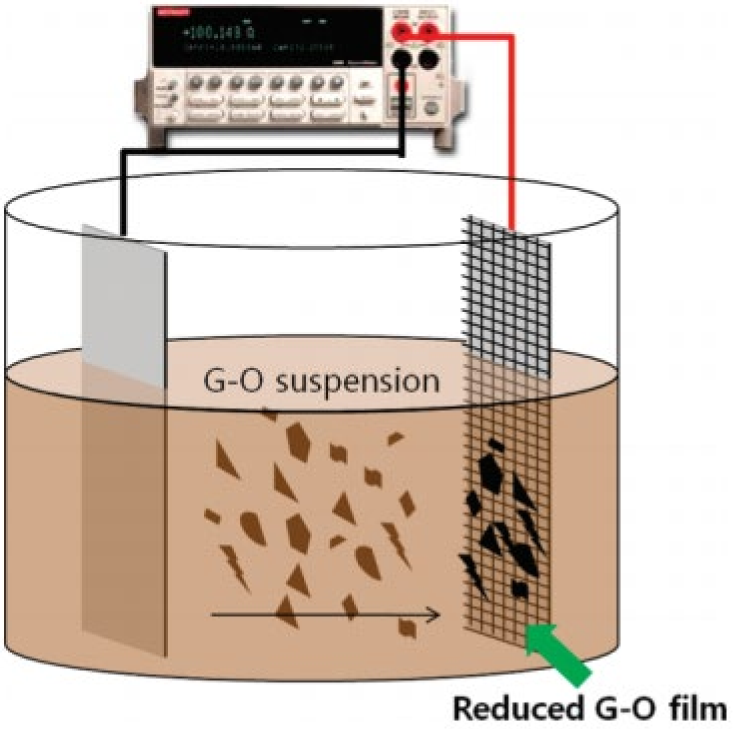

Figure 2-12: Schematic diagram of the simple EPD process[82].

In addition to homogenous films, nanocomposite films can also be deposited using EPD. In an article by Wang et al., charging additives were added to the EPD solution adsorbing onto both MnO_2 and MWCNT causing both species to become charged[84]. The nanocomposite films were studied in supercapacitor applications and resulted in a high specific capacitance of 553 Fg^{-1}.

2.6.2 Chemical Bath Deposition

Similar to EPD, chemical bath deposition (CBD) is a low temperature, simple, and inexpensive synthesis method[85]. Thin films are formed in CBD when the solution is saturated. To clarify, the ionic product of anions and cations in the synthesis solution is equal to the solubility product of the metallic precursors and when the latter is surpassed, ions combine and precipitation occurs on the substrate[86]. A notable advantage of CBD is that electrical conductivity is not a requirement for the substrate, in fact, any insoluble material to which the synthesis solution has ionic access to is an appropriate substrate[87].

An example of CBD reactions to form nickel-cobalt sulfide supercapacitor electrodes can be seen in a detailed report by Zhao et al.[88]. Firstly, Zhao dissolved nickel and cobalt salts with hexamethylenetetramine in a mix of deionized water and ethanol, as seen in Eq.2.21.

Zhao et al. then reacted the nickel-cobalt-hydroxide product with a certain amount of thioacetamide which acted as the sulfur supply shown in Eq. 2.22, which produced the final electrode material $NiCo_xS_y$.

$$Ni^{2+} + 2xCo^{2+} + 3\,CO_2 + 12OH^- \rightarrow\ 2NiCo_x(CO_3)_{1.5}(OH)_3 + 3H_2O \tag{2.21}$$

$$\begin{gathered} 2NiCo_x(CO_3)_{1.5}(OH)_3 + 2yH_2S + (y-3)O_2 \rightarrow \\ 2NiCo_xS_y + (3+2y)H_2O + 3CO_2 \end{gathered} \tag{2.22}$$

This CBD synthesis procedure produced a thin film flaky nickel cobalt sulfide electrode which had a specific capacitance of 1196 F g^{-1}.

The freedom in substrate material selection given by CBD allowed for layered birnessite-MnO_2 films to be deposited on flexible transparent plastic substrates[89]. Compressive and tensile bending tests displayed that the MnO_2 film electrodes retain exceptional electrochemical stability as well as mechanical flexibility. In addition to metal oxides, CBD can also be used to synthesize conducting polymer electrodes. Polyaniline (PANI) is a conductive polymer that exhibits pseudocapacitive behavior[90]. In an impressive study by Deshmukh et al., PANI thin films were synthesized by chemical oxidization of the monomer aniline with ammonium persulfate in a sulfuric acid solution[91]. One disadvantage of CBD is the reaction-based deposition can be time consuming, hindering its practicality. A technique used by Deshmukh et al. was to use microwaves to enhance the CBD process. This technique reduced synthesis time significantly producing a high-performing PANI electrode with a specific capacitance of 753 F g^{-1}. A key advantage of CBD is that composite electrodes can be synthesized with desirable morphologies and low ESR. For example, Qui et al. synthesized graphene-NiO core-shell nanosheets through a simple CBD method. The interconnections among the nanosheets exhibited excellent electrical conductivity and a high energy density of 19.5 Wh kg^{-1}.

2.6.3 Heterocoagulation

As mentioned previously, thin film electrodes are not practical for supercapacitor electrodes for energy storage applications. To maintain low internal resistance of the electrode conductive additives are necessary. Heterocoagulation is a recent innovative fabrication route used to link CNT to pseudocapacitive materials. This method uses a dispersing agent for the dispersion of oxide nanoparticles and an oppositely charged dispersing agent for the dispersion of CNT forming a composite with low internal resistance, as shown in Figure 2-13[92].

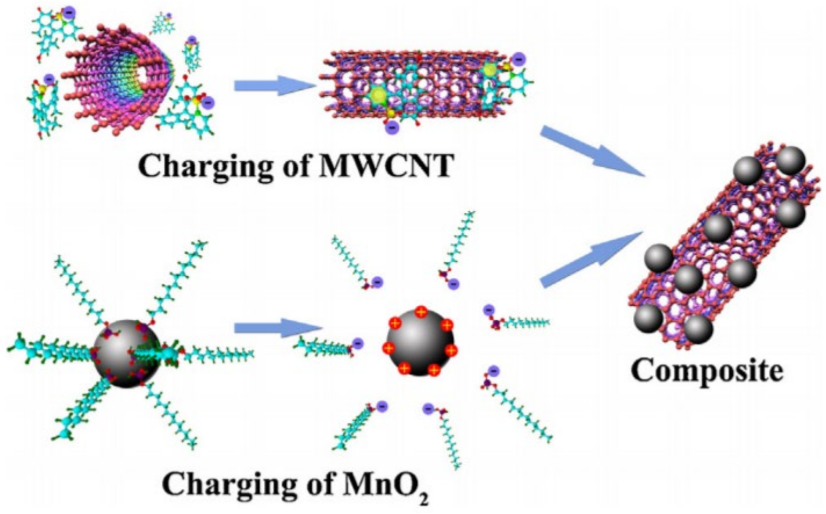

Figure 2-13: Synthesis process for heterocoagulation using MWCNT and MnO_2[92].

From the previous studies, it has been made clear that covalent functionalization methods for the dispersion of CNT are not ideal due to the degradation of MWCNT structure and properties from such techniques[93]. In a heterocoagulation method used by Ata et al., the surface of MWCNT was modified using small charged aromatic molecules adsorbed on the surface with π-π staking and hydrophobic interactions, improving the MWCNT dispersion[94]. Ata selected Mn_3O_4 as the active material for the electrode which was dispersed using a molecule called P(SSA-MA). This unique multifunctional molecule allowed efficient adsorption on Mn_3O_4 imparted by the MA monomer, whereas SSA monomers provided a negative charge. Enhanced dispersion of the individual electrode components and their electrostatic heterocoagulation facilitated improved mixing of these components, producing a well mixed composite electrode with high active mass loading.

2.6.4 Particle Extraction Through the Liquid-Liquid Interface

The Liquid-liquid interface (LLI) provides a unique two-dimensional environment different from that of a bulk fluid. Novel methods of particle synthesis and surface functionalization of material at the LLI have combined the advantages of material synthesis in organic and aqueous phases[95]. In particle extraction through the liquid-liquid interface (PELLI), inorganic particles are synthesized in an aqueous solution and transferred to an immiscible organic solvent as seen in Figure 2-14[96].

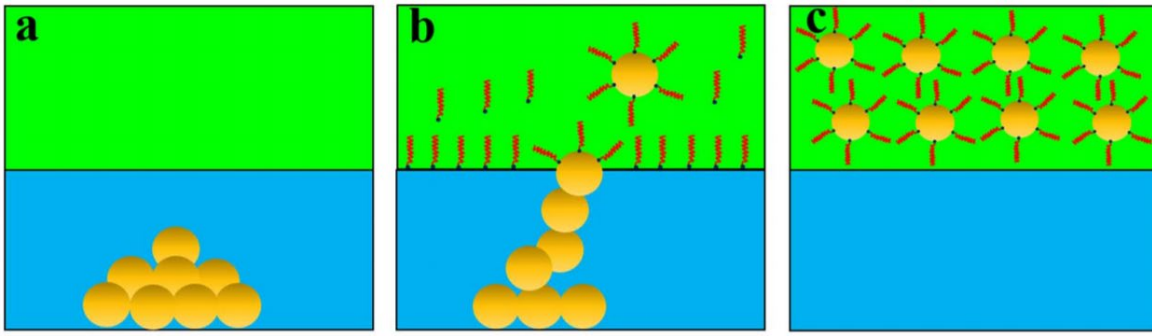

Figure 2-14: Schematic of (a) precipitation of particles in aqueous solution, (b,c) different stages in extraction[96].

PELLI addresses a major difficulty for the synthesis of nanoparticles by wet chemical methods, which is the agglomeration of nanoparticles after removal from the solution after synthesis. Hydroxide groups on the particle surface can undergo condensation, forming oxo-bridges which results in the agglomeration of oxide and hydroxide particles while drying. In many applications, co-dispersion of non-agglomerated nanoparticles with other materials is necessary[97]. Specifically, in supercapacitor electrode fabrication, active material must be combined with conductive additives and water insoluble polymer binders[98]. To clarify, PELLI is used to co-disperse active materials prepared in aqueous solutions by transferring the particles to an immiscible organic solvent by using multifunctional extractor molecules. These extracted particles are then mixed with conductive additives avoiding the agglomeration that occurs during the drying stage. The extractor molecules typically consist of a hydrophobic carbon chain as well as a functional group that facilitates adsorption to the active material.

In a study by Chen et al., multiple distinct molecules were used to transfer MnO_2 particles from the aqueous synthesis solution and disperse them in an organic phase[99]. In the PELLI fabrication technique the agglomeration of oxide particles during drying was avoided and improved mixing of MnO_2 and MWCNT occurred in the organic phase. The reduction in agglomeration using PELLI facilitated mixing of components resulting in significantly lower resistance shown in Figure 2-15. Not only was the ESR reduced using PELLI but the capacitance of the electrode using the most suitable extractor molecule doubled the capacitance of the electrode synthesized without PELLI.

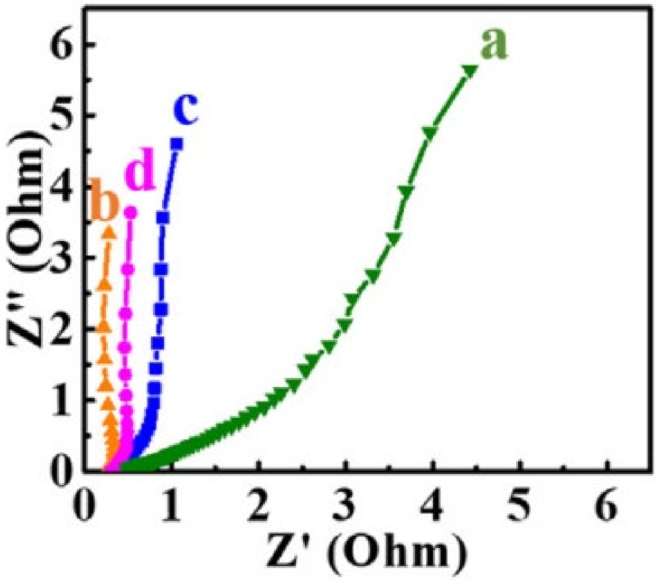

Figure 2-15: Nyquist plot of complex impedance for MnO_2-MWCNT electrodes prepared (a) without extraction and (b–d) by PELLI using (b) 16-phosphonohexadecanoic acid, (c) octadecylphosphonic acid, and (d) stearic acid extractors[99].

Chapter 3: Problem Statements and Objectives

To meet the ever-increasing energy storage requirements, supercapacitors with high active mass loadings are necessary to achieve high energy and power densities. High mass electrodes suffer from particle agglomeration causing poor electrolyte access to active material. On top of this, the agglomeration of active material such as oxides and hydroxides cause poor mixing with conductive additives, reducing the overall electrochemical performance of the device. Furthermore, the lack of research in the area of negative electrodes for supercapacitor devices has caused the improvements in negative electrode performance to lag behind that of positive electrodes.

One objective of this investigation is to fabricate high mass electrodes with good electrochemical performance and rate capability. To achieve this, the development a novel processing technique for the synthesis of non-agglomerated particles is necessary. A second objective of this investigation is to develop an advanced negative electrode for the fabrication of asymmetric supercapacitors

Chapter 4: Experimental Procedures

4.1 Chemicals and Materials

Table 4-1: Table of materials used.

Material Use	**Material Name**	**Source**
Active Materials	Potassium permanganate (KMnO4)	Sigma-Aldrich
	Iron chloride hexahydrate ($FeCl_3·6H_2O$)	Sigma-Aldrich
	Manganese nitrate tetrahydrate ($Mn(NO)_3·4H_2O$)	Sigma-Aldrich
Dopant	Zinc chloride ($ZnCl_2$)	Anachemia
Extracting Agents	Octyl gallate (OG)	Sigma-Aldrich
	Octanohydroxamic acid (OHA)	TCI Chemicals
	Bufexamac (BF)	TCI Chemicals
Organic Solvents	Ethanol	Commercial Alcohols
	n-butanol	Fisher Chemical
Conductive Additive	Multi-walled carbon nanotubes (MWCNT) (ID: 4 nm, OD: 13 nm, Length: 1-2 µm)	Bayer
Binder	Poly(vinyl butyral-co-vinyl alcohol-co-vinyl acetate, Average Mw = 50000- 80000 (PVB)	Sigma-Aldrich
Dispersing Agent	Methyl Violet 3RAX	Sigma-Aldrich
	Calconcarboxylic acid (CA)	Sigma-Aldrich
Electrolyte	Sodium sulfate (Na_2SO_4)	Caledon Laboratory Chemicals
Current Collector	Nickel foam	Vale
Reference Electrode	Potassium chloride (KCl)	Fisher Chemical
Base (pH Adjustment)	Sodium Hydroxide (NaOH)	Caledon Laboratory Chemicals

4.2 Synthesis of Electrode Materials Using Octyl Gallate for PELLI

A simple multiple-step procedure was performed to obtain the oxide nanoparticles extracted by the liquid-liquid extraction method using Octyl Gallate (OG). For the α-FeOOH: (i) 330 mg of $FeCl_3·6H_2O$ was dissolved in 50 mL of deionized (DI) H_2O using mild stirring. (ii) 1M NaOH was added to the solution until pH 7 was reached under continuous stirring. (iii) A new solution with 33 mg of OG was dissolved in 20 mL of n-butanol using ultrasonic bath. (iv) Both solutions were mixed under stirring for 2 min and set to rest for 2 min for phase transfer to occur. (v) The solution was poured into a separation funnel and the bottom aqueous phase was removed. (vi) The remaining nanoparticles in the n-butanol phase were mixed using ultrasonic bath with a fresh solution containing 25 mg of MWCNT already dispersed with 25 mg of calconcarboxylic acid in 20 mL of n-butanol. (vii) The final solution was washed with 750 mL of water followed by 250 mL of ethanol under vacuum pump-filtration then stored in a desiccator.

For the Mn_3O_4: (i) 330 mg of $Mn(NO_3)_2 \cdot 4H_2O$ was dissolved in 50 mL of H_2O using ultrasonic bath. (ii) 2M NaOH solution was added dropwise under ultrasonic bath until a pH of 10 was achieved. The steps from (iii) to (vii) were the same previously described.

For the MnO_2: (i) 180 mg of $KMnO_4$ was dissolved in a solution containing 100 mL of H_2O and 20 mL of n-butanol by stirring overnight. (ii) 25 mg of OG was dissolved in 20 mL of n-butanol using ultrasonic bath. The subsequent steps are described above as (iv) to (vii).

ZnO was prepared by chemical precipitation from 0.26 M $Zn(NO_3)_2$ solutions (100 mL) in water at a temperature of 70 °C and pH of 8. The pH of the solutions was adjusted using 1 M NaOH.

4.3 Synthesis of Electrode Materials Using Octanohydroxamic Acid for PELLI

For the Mn_3O_4: (i) 330 mg of $Mn(NO_3)_2·4H_2O$ was dissolved in 50 mL of H_2O using an ultrasonic bath. (ii) 33 mg of OHA was dissolved in 2M NaOH solution which was then added dropwise into the dissolved $Mn(NO_3)_2$ solution under ultrasonic bath until pH 10 was reached. (iii) 20 mL of pure n-butanol was added to the solution. (iv) The solution was mixed under stirring for 2 min and set to rest for 2 min for phase transfer to occur. (v) The solution was poured into a separation funnel and the bottom aqueous phase was removed. (vi) The remaining nanoparticles in the n-butanol phase were mixed using an ultrasonic bath in a fresh solution containing 25 mg of MWCNTs already dispersed in 20 mL of n-butanol with 25 mg of OHA. (vii) The final solution was washed with 750 mL of water followed by 250 mL of ethanol under vacuum pump-filtration then stored in a desiccator.

For the MnO_2: (i) 180 mg of $KMnO_4$ was dissolved in a solution containing 100 mL of H_2O and 20 mL of n-butanol by stirring overnight. (ii) 33 mg of OHA was dissolved in 20 mL of n-butanol using an ultrasonic bath. (iv) Both solutions were mixed under stirring for 2 min and set to rest for 2 min for phase transfer to occur. The steps from (v) to (vii) were the same as previously described.

4.4 Synthesis of Zn/FeOOH Electrode Materials

For the Zn/FeOOH: (i) 330 mg of $FeCl_3·6H_2O$ and 30 mg of $ZnCl_2$ was dissolved in 12.5 mL of H_2O using mild stirring. (ii) 4M NaOH was added to the solution until pH

13 was reached under continuous stirring. (iii) The freshy precipitated Zn doped FeOOH particles were filtered with DI water until pH returned to 7. (iv) The particles were re-dispersed in DI water and mixed with a solution containing 23 mg of MWCNT already dispersed in 75 mL of DI water with 23 mg of Methylene Violet 3RAX as a dispersant. (vii) The solution of Zn/FeOOH and MWCNT was ultrasonicated for 100 min. (viii) The final solution was washed with 750 mL of water followed by 250 mL of ethanol using vacuum pump-filtration then stored in a desiccator.

The Pure FeOOH electrode was prepared in an identical manner excluding the 30mg of $ZnCl_2$ in step (i) and only a pH of 7 was reached in step (ii).

4.5 Characterization of Electrode Materials

4.5.1 SEM

The microstructures of the composite electrodes were qualitatively analyzed using scanning electron microscopy (SEM) at the Canadian Centre for Electron Microscopy using a JEOL JSM-7000F. The beam current was set to the auto-low or auto-medium setting for the instrument depending on the sample. Electrodes were prepared for SEM analysis by adhering a small cut-off of the electrode on the centre of a piece of double-sided copper tape on a stainless-steel sample stub. Silver or nickel paste was applied along the edges of the copper tape to improve conductivity to the stub. Due to the conductivity needed for enhanced SEM images the samples were coated with a 5 nm layer of platinum.

4.5.2 FTIR and XPS

Fourier transform infrared spectroscopy (FTIR) was performed at the McMaster Biointerfaces Institute- to obtain an infrared spectrum of absorption from dispersing agents used in the PELLI experiments. The instrument used was a Bio-Rad FTS-40. X-ray photoelectron spectroscopy (XPS) was used to study the difference in oxidation states of Mn_3O_4 before and after cycling procedures. The instrument used was a Physical Electronics Quantera II.

4.5.3 XRD

2D diffraction data was collected at the MAX Diffraction Facility at McMaster University, Hamilton, ON.

For iron-containing samples X-Ray diffraction (XRD) testing was performed using the Bruker D8 DISCOVER with DAVINCI.DESIGN diffractometer, equipped with Cobalt Sealed Tube Source (λ avg = 1.79026 Å), Vantec 500 (MiKroGap TM technology) area detector. 5 frames were captured with an exposure time of 420 seconds per frame with a power setting of 35 kV, 45 mA.

For manganese containing samples instrumentation with Bruker Smart6000 CCD area detector and a Rigaku RU200 Cu $K\bar{\alpha}$ rotating anode was used. 7 frames were used with 300 seconds per frame and a power setting of 50 kV, 90 mA.

2D frames were collected with DIFFRAC-Measurement Centre version 4.2 software and integrated to 1D using DIFFRAC.EVA Version 4.0. Phase identification was performed using the integrated ICDD PDF-4 + 2018 powder database in DIFFRAC.EVA.

4.6 Fabrication of Electrodes

The supercapacitor electrodes were synthesised via slurry impregnation. To begin, a piece of 95% porosity nickel foam was cut into 1.5 cm by 1cm rectangular pieces and cleaned using DI water and ethanol. The mass of the nickel foam was obtained using a Toledo AX105 scale prior to impregnation. The composite electrode material previously synthesized was ground in a mortar with 3 wt% of binder (PVB) dissolved in ethanol. The desired mass loading was then loaded onto a 1 cm by 1cm section of the nickel foam. The impregnated nickel foam was dried and then placed on the scale to determine if more mass loading was necessary. Once the nickel foam was loaded with the desired mass it was rolled in three steps to around 30% of the original thickness resulting in an electrode approximately 0.37 mm thick. After rolling, the mass of the electrode was measured again and the difference from the unimpregnated nickel foam was the mass loading of the electrode. Copper wire was soldered to the unimpregnated area of the nickel foam and wired through a glass tube. The glass tube, soldered copper joint, and exposed nickel foam were sealed using LePage Speed Set Epoxy.

4.7 Electrochemical Characterization of Electrodes

To get an in-depth analysis of multiple aspects of the electrodes, various electrochemical characterization techniques were used. Single electrodes were tested using a three-electrode setup with the counter electrode as platinum gauze and the reference as a saturated calomel electrode (SCE). All tests were performed in 0.5 M Na_2SO_4 aqueous electrolyte at room temperature.

4.7.1 Cyclic Voltammetry

Cyclic Voltammetry (CV) is a potentiodynamic electrochemical technique which measures the current that develops in an electrochemical cell in response to a liner change in voltage. Capacitors have a distinct "box shape" CV curve due to their governing equation as shown:

$$Q = CV \rightarrow \frac{dQ}{dt} = I = \frac{d}{dt}(CV) \tag{4.1}$$

Taking the derivative of both sides of the equation with respect to time results in current on one side because (dQ/dt) is current (I). Since capacitance does not depend on time, it can be removed from the derivative as a constant. On the other hand, voltage is varying *linearly* with time so its derivative will just be a constant which is denoted as scan rate (υ), as shown:

$$I = C\frac{dV}{dt} = C\upsilon \tag{4.2}$$

It is important to note that during cyclic voltammetry the scan rate is kept constant, for example, 5 mV s^{-1}. Since both capacitance and scan rate are constant the current response will be constant as well resulting in the rectangular box shape shown in Figure 4-1.

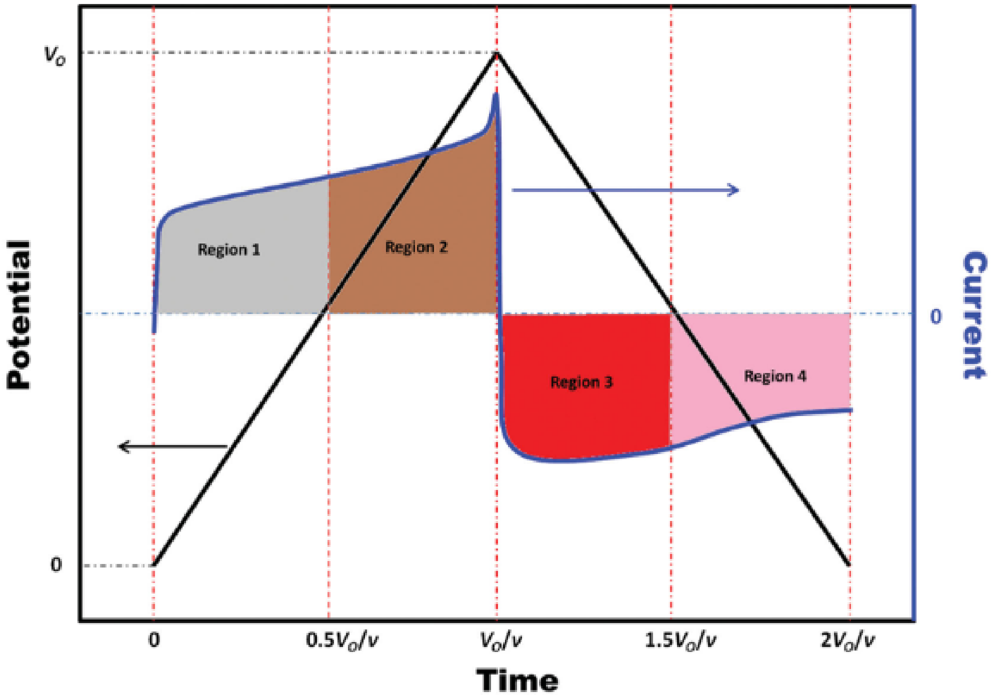

Figure 4-1: A typical CV for supercapacitors displayed in linear form to display the effect increasing the potential (black) induces current (blue)[100].

The scan rates used for CV were 2, 5, 10, 20, 50, and 100 mV s^{-1}. The manganese-based electrodes were tested in a voltage range of 0 to 0.9 V vs SCE and FeOOH-based electrodes were analyzed in a voltage range of -0.8 to 0 V vs SCE. The capacitance values were calculated using the area of the CV curves with the following equations where C_g is specific capacitance (F g^{-1}) and C_s is areal capacitance (F cm^{-2}):

$$C_g = \frac{Q}{2mv\Delta V} \tag{4.3}$$

$$C_s = \frac{Q}{2v\Delta V} \tag{4.4}$$

4.7.2 Electrochemical Impedance Spectroscopy

Electrochemical impedance spectroscopy uses a small amplitude sinusoidal alternating current (AC) excitation signal to determine the resistive properties of an electrochemical system. Voltage signals were applied in succession from 10 mHz to 100 kHz with an AC voltage amplitude of 5 mV. The amplitude and the phase shift of the current response (Eq. 4.6) from the applied AC voltage (Eq. 4.5) provides information on the real and imaginary components of the impedance (Eq. 4.7)

$$E(t) = E_0 exp(j\omega t) \tag{4.5}$$

$$I(t) = Aexp\big(j(\omega t - \varphi)\big) \tag{4.6}$$

$$Z = \frac{V}{I} = \frac{E_0}{A} exp(j\varphi) = Z' + jZ'' \tag{4.7}$$

Nyquist plots are created by plotting Z′ vs Z″ of each frequency point as seen in Figure 4-2. At high frequencies, R_E is mainly the result of the electric resistance from connections such as contact resistance between the active material and current collector, the measurement connections, and the resistance of the electrolyte[101]. At medium frequencies (R_C), the semicircle diameter is correlated to the resistance at the interface between the electrolyte and the porous electrode surface as well as charge transfer resistance. For lower frequencies (R_D), the resistance from the diffusion of ions creates a 45° angle line which is commonly denoted as Warburg impedance. At even lower frequencies the electrode is able to act as a capacitor due to the full penetration of ions in the porous microstructure producing a vertical line on the Nyquist plot.

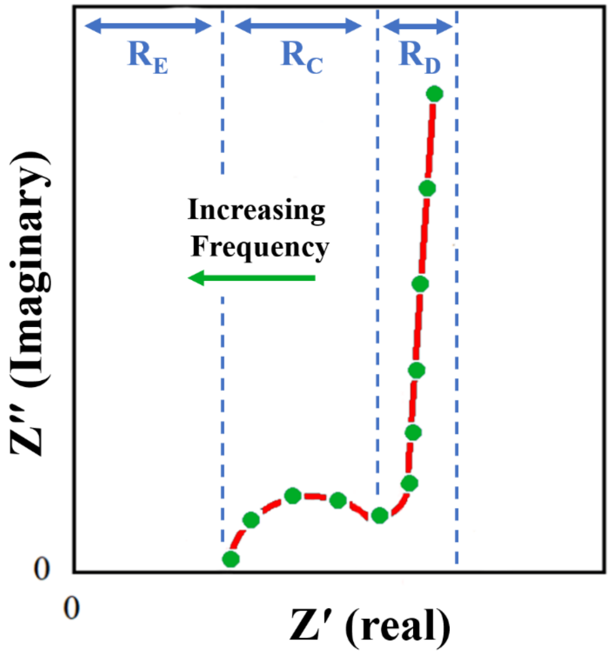

Figure 4-2: Typical Nyquist plot for supercapacitors.

As mentioned above, at low frequencies, capacitive processes are leading. Complex capacitance can be derived from impedance as seen in the equations below, Eq. 4.8 to Eq. 4.12. Plotting C′ against frequency provides data about the capacitance of the overall system and reports similar values to that of the capacitance values calculated from the CV curves or GCD. In addition, C″ versus frequency typically displays a plot with a maximum at a certain frequency which pertains to a relaxation time. The relaxation time is at a frequency where the resistive and capacitive components are equal and gives information on the rate capability of the electrode.

$$Z = Z' + jZ'' = \frac{1}{i\omega C} = \frac{-i}{\omega C} \rightarrow C = \frac{-i}{\omega Z} \tag{4.8}$$

$$C = \frac{-i}{\omega(Z' + jZ'')} = -\frac{i(Z' + jZ'')}{\omega|Z|^2} = \frac{Z''}{\omega|Z|^2} - \frac{iZ'}{\omega|Z|^2} \tag{4.9}$$

$$C = C' - iC'' \tag{4.10}$$

$$C' = \frac{Z''}{\omega|Z|^2} \quad , \quad C'' = \frac{iZ'}{\omega|Z|^2} \tag{4.11 \& 4.12}$$

4.7.3 Galvanostatic Charge-Discharge

Galvanostatic charge-discharge (GCD) is a common technique used to test the performance and cycle-life of supercapacitors using constant current to charge and discharge the electrode or device. Building off Eq. 4.2 from the previous subchapter, the equation can be integrated accordingly:

$$\frac{dV}{dt} = \frac{I}{C} \rightarrow \int_0^V dV = \int_0^t \frac{I}{C} dt \tag{4.13}$$

$$V(t) = \frac{I}{C} t + Constant \tag{4.14}$$

It has been mentioned previously that capacitance does not vary with time, so it can be removed from the integral. In GCD, current is applied at a constant rate which according to Eq. 4.9, will result in a linear profile depending on the direction of the current, seen in Figure 4-3.

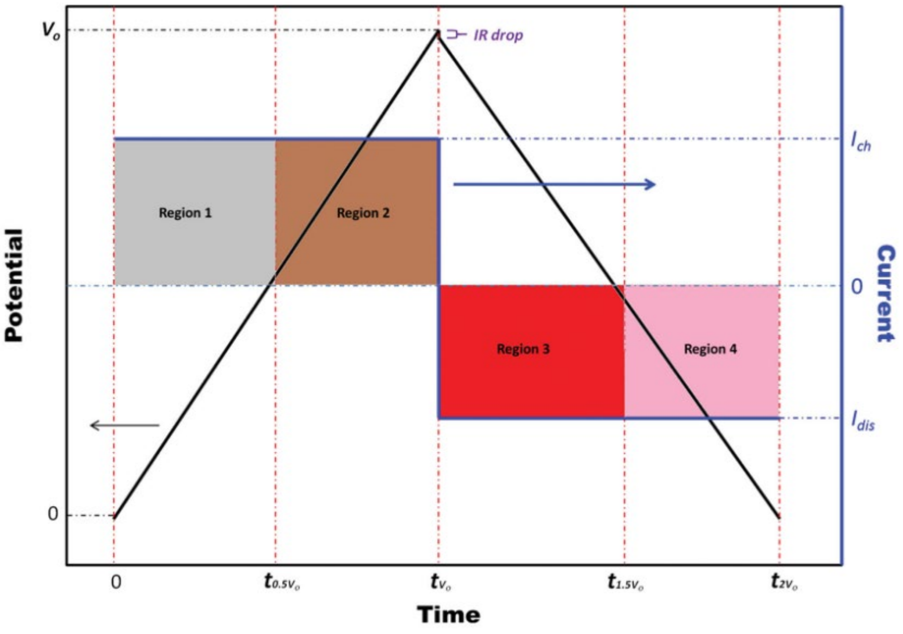

Figure 4-3: GCD of a supercapacitor[100].

As the electrode is polarized an "IR drop" is observed, which is a common feature on GCD curves. IR drop is caused by the internal resistance of the electrode or cell and increases at higher charge/discharge rates as it is a function of current.

GCD provides charge-discharge time (Δt), current (I), and voltage window ($V_1 - V_2$). Using these values as well as the mass loading the energy (S_E) and power (S_p) density of an electrode or cell can be calculated using the following equations.

$$S_E = \frac{I\Delta t(V_1 - V_2)}{2m} \tag{4.15}$$

$$S_P = \frac{I(V_1 - V_2)}{2m} \tag{4.16}$$

Chapter 5: Surface Modification and Dispersion of Ceramic Particles Using Liquid-Liquid Extraction Method for Application in Supercapacitor Electrodes

Reprinted article with permission from J. Milne, R. Marques Silva, and I. Zhitomirsky, "Surface modification and dispersion of ceramic particles using liquid-liquid extraction method for application in supercapacitor electrodes," *J. Eur. Ceram. Soc.*, IN PRESS. DOI: 10.1016/j.jeurceramsoc.2018.12.023

Author's Contribution:

- Synthesis of electrode materials
- Electrochemical testing of electrodes
- FTIR and XRD of materials
- Literature evaluation
- Preparation of manuscript draft

ARTICLE IN PRESS

Journal of the European Ceramic Society xxx (xxxx) xxx–xxx

Contents lists available at ScienceDirect

Journal of the European Ceramic Society

journal homepage: www.elsevier.com/locate/jeurceramsoc

Original Article

Surface modification and dispersion of ceramic particles using liquid-liquid extraction method for application in supercapacitor electrodes

Jordan Milne, Ricardo Marques Silva, Igor Zhitomirsky*

Department of Materials Science and Engineering, McMaster University, 1280 Main Street West, Hamilton, Ontario L8S 4L7, Canada

ARTICLE INFO

Keywords:
Adsorption
Extraction
Octyl gallate
Oxide
Supercapacitor
Ceramic

ABSTRACT

Particle extraction through liquid-liquid interface (PELLI) was used for the extraction of MnO_2, Mn_3O_4, FeOOH and ZnO particles from an aqueous synthesis medium to the n-butanol phase. The benefits of PELLI were demonstrated by the fabrication of supercapacitor electrodes, which showed good electrochemical performance at high active mass loadings. Octyl gallate (OG) was found to be an efficient and versatile extractor for the ceramic particles. The phase transfer of the particles resulted in reduced agglomeration, which allowed for improved electrolyte access to the particle surface and facilitated their mixing with conductive multiwalled carbon nanotube (MWCNT) additives. It was shown that OG is a promising extractor material for the fabrication of ceramic-ceramic, ceramic-metal and ceramic-MWCNT nanocomposites. The strong adsorption of OG on the particle surface involved bridging or chelating bidentate bonding of the catechol group to the metal atoms. The capacitive properties of FeOOH-MWCNT electrodes were tested in the negative potential window. MnO_2-MWCNT and Mn_3O_4-MWCNT electrodes were investigated for charge storage in the positive potential window. The highest capacitance of 5.7 F cm^{-2} for positive electrodes was achieved using MnO_2-MWCNT composites with active mass loading of 36 mg cm^{-2}. The Mn_3O_4-MWCNT electrodes exhibited improved capacitance retention at high charge-discharge rates.

1. Introduction

Chemical precipitation methods are widely used for the synthesis of ceramic materials from aqueous solutions of metal salts [1–3]. However, colloidal processing in organic solvents is critical for many applications, which require the use of water-insoluble binders, film forming agents and other functional organic materials. The use of water-insoluble organic binders is necessary for the fabrication of electrodes of aqueous supercapacitors, batteries and sensors. Water-insoluble binders allow stable performance of the electrodes in aqueous electrolytes [4]. Binder materials must be dissolved in an organic solvent and combined with ceramic particles for the fabrication of slurries for electrode fabrication. In traditional approaches, the particle transfer from the aqueous synthesis medium to an organic medium involves particle drying and re-dispersion [5–7]. However, drying procedures usually result in significant particle agglomeration due to the condensation reactions of surface OH groups. The reduction of surface energy is another driving force for the particle agglomeration. One of the great challenges of the supercapacitor technology is transfer of non-agglomerated particles from water to an organic solvent, containing a dissolved binder, and particle co-dispersion with conductive additives.

Recently, significant interest has been generated in particle extraction through liquid-liquid interface (PELLI), which offers benefits of direct particle transfer from water to an organic solvent and involves particle modification in an aqueous phase or at the liquid-liquid interface [8–12]. The success of this technology will depend largely on the development of advanced extractors, which must be strongly adsorbed on particle surface. Of particular interest are head-tail surfactants, containing an anchoring hydrophilic group and a hydrophobic hydrocarbon group [12]. The strong bonding of the anchoring groups to the particle surface is critical for an efficient extraction. Moreover, the strong bonding is necessary in order to minimize the extractor concentration. The hydrocarbon groups facilitate extractor dissolution in organic solvents. The investigation of different extractor molecules provides an insight into the influence of their molecular structure on the extraction of ceramic materials [8,12].

Of particular interest are molecules, containing catechol or galloyl groups, which allow for a catecholate-type bidentate bonding to metal atoms on the particle surface. The interest in catecholate-type bonding resulted from the investigation of strong mussel adhesion to different surfaces, which involves proteins, containing catecholate monomers [13–15]. The fundamental investigations of mussel protein adsorption

---

* Corresponding author.
E-mail address: zhitom@mcmaster.ca (I. Zhitomirsky).

https://doi.org/10.1016/j.jeurceramsoc.2018.12.023
Received 9 November 2018; Received in revised form 1 December 2018; Accepted 10 December 2018

[16–18] have stimulated the development of various cationic and anionic dispersants from the catechol and gallic acid families for surface modification and dispersion of oxide materials [19–23]. These studies revealed strong adsorption of small organic molecules, containing single catechol or galloyl groups to different oxide particles [24–27]. Therefore, the investigation of surfactants with galloyl anchoring groups is a promising strategy for the development of advanced extractors for PELLI technology. Previous investigations [28] highlighted the need for good dispersion of active materials, which allow better utilization of their charge storage properties in supercapacitors. Therefore, PELLI is a promising method for the fabrication of supercapacitor electrodes.

The goal of this investigation was the application of PELLI for the extraction of different ceramic materials and application for supercapacitors. The approach was based on the use of octyl gallate (OG) as a new extractor for PELLI. The results presented below showed strong adsorption of OG on nanoparticles of MnO_2, Mn_3O_4, FeOOH and ZnO. OG is a versatile extractor, which facilitated efficient transfer of the nanoparticles from an aqueous synthesis medium to the n-butanol phase. The use of PELLI allowed the fabrication of advanced supercapacitor electrodes, which showed good electrochemical performance at high active mass loadings.

2. Experimental procedures

$FeCl_3 \cdot 6H_2O$, $Mn(NO_3)_2 \cdot 4H_2O$, $KMnO_4$, $Zn(NO_3)_2 \cdot 6H_2O$, NaOH, Na_2SO_4, octyl gallate (OG), *n*-butanol, polyvinyl butyral (PVB), calconcarboxylic acid (Aldrich, USA), multiwalled carbon nanotubes (MWCNT, ID 4 nm, OD 13 nm, length 1– 2 µm, Bayer, Germany) and Ni foam (95% porosity, Vale, Canada) were used. Synthesis of MnO_2 was performed at 20 °C using 50 ml of aqueous 0.01 M $KMnO_4$ solution and 20 ml n-butanol as a reducing agent. In this method, the formation of MnO_2 was achieved at the liquid-liquid interface and after stirring the obtained MnO_2 particles precipitated in the aqueous phase. FeOOH was prepared at 20 °C by chemical precipitation from aqueous 0.024 M $FeCl_3$ solutions (100 ml) at pH = 7. Mn_3O_4 was synthesized at 20 °C from aqueous 0.026 M $Mn(NO_3)_2$ solutions (100 ml) at pH = 10. ZnO was prepared by chemical precipitation from 0.26 M $Zn(NO_3)_2$ solutions (100 ml) in water at a temperature of 70 °C and pH = 8. The pH of the solutions was adjusted using 1 M NaOH. Liquid-liquid extraction was performed by adding OG solutions in n-butanol to the aqueous phases, containing precipitated particles. The mass ratio of oxide or hydroxide material to OG was 4:1. MWCNT were dispersed in n-butanol using calconcarboxylic acid as a dispersant. The suspensions of metal oxide or hydroxide particles and MWCNT in n-butanol were mixed and used for the impregnation of Ni-foam current collectors. The mass ratio of oxide/hydroxide particles and MWCNT was 4:1. The slurries contained a PVB binder, dissolved in n-butanol. The mass of PVB was 3% of the total mass of metal oxide/hydroxide material and MWCNT. The mass loading of the electrode material in the Ni-foam current collectors was 36 mg cm^{-2}.

The prepared materials were characterized by X-ray diffraction (Smart 6000, Bruker, USA, CuK_α radiation), FTIR spectroscopy (FTS-40, Bio-Rad, USA) and scanning electron microscopy (SEM, microscope JEOL, JSM-7000 F, Japan). The samples for the FTIR studies were obtained from powder materials, which were prepared by filtration, washing and drying of the suspensions, containing extracted particles. Cyclic voltammetry (CV) and electrochemical impedance spectroscopy (EIS) investigations were carried out using a potentiostat (PARSTAT 2273, Princeton Applied Research, USA). The capacitive behavior of the electrodes was investigated in three-electrode cells using 0.5 M Na_2SO_4 aqueous electrolyte solution. The area of the working electrode was 1 cm^2. The counter electrode was a platinum gauze and the reference electrode was a saturated calomel electrode (SCE). CV studies were performed at scan rates of 2–100 mV s^{-1}. The areal (C_S) and gravimetric (C_M) specific capacitances were calculated using Eqs. 1 and 2, respectively:

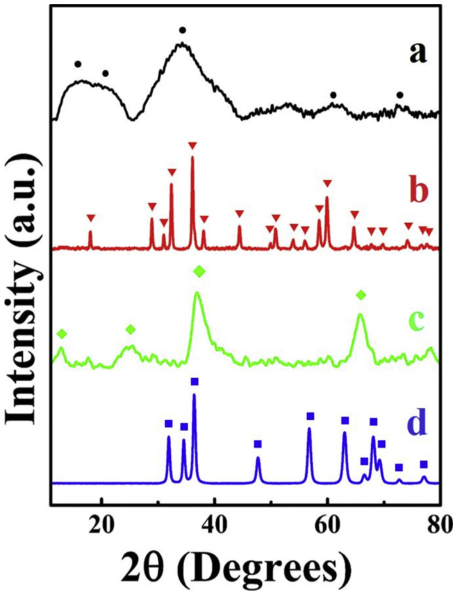

Fig. 1. X-ray diffraction pattern of the as-prepared materials (a) FeOOH (● - JCPDS card 29-713), (b) Mn_3O_4 (▼ - JCPDS card 24-0734), (c) MnO_2 (◆ - JCPDS card 23-1046), (d) ZnO (■ - JCPDS card 36-1451).

$$C_S = Q/\Delta VS \tag{1}$$

$$C_M = Q/\Delta Vm \tag{2}$$

The half of the CV area was used for the calculation of the charge (Q) in the voltage window ΔV for electrodes with area S and active material mass m.

Complex impedance $Z = Z' - iZ''$ measurements were performed in the frequency range of 10 mHz-100 kHz using a signal with amplitude of 5 mV. The components of complex capacitance $C_S = C_S' - iC_S''$ were calculated using Eqs. 3 and 4.

$$C_S' = Z''/\omega|Z|^2 S \tag{3}$$

$$C_S'' = Z'/\omega|Z|^2 S \tag{4}$$

where $\omega = 2\pi f$ (f-frequency).

3. Results and discussion

Fig. 1 shows X-ray diffraction patterns of as prepared ceramic materials. The X-ray diffraction pattern of FeOOH exhibited very broad peaks, corresponding to the JCPDS file 29-713 of α-FeOOH. The XRD patterns for Mn_3O_4 and ZnO showed well defined peaks, corresponding to JCPDS files 24-0734 and 36-1451, respectively. The MnO_2 sample showed broad peaks of birnessite, corresponding to the JCPDS file 23-1046.

OG was used as an extractor for MnO_2, Mn_3O_4, FeOOH and ZnO particles. Fig. 2 shows chemical structure of OG, which includes an anchoring galloyl group and a hydrophobic hydrocarbon chain. It is suggested that adsorption mechanism of OG is similar to that of gallic acid. This mechanism can involve bridging or chelating bidentate bonding (Fig. 2).

The strong adsorption of OG on the particle surface at the water-*n*-butanol interface allowed for particle extraction to the n-butanol phase (Fig. 3). The OG adsorption on the particles was confirmed by the results of FTIR studies (Fig. 4).

The FTIR spectra of extracted materials showed absorptions in the range of 2800-3000 cm^{-1}, which were attributed to the asymmetric and symmetric stretching vibrations [8,29] of the CH_2 and CH_3 groups

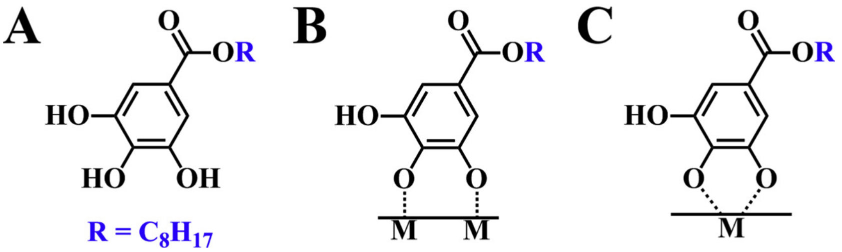

Fig. 2. (A) Chemical structure of OG, (B) bridging adsorption mechanism, and (C) chelating adsorption mechanism, involving metal atoms (M) on the particle surface.

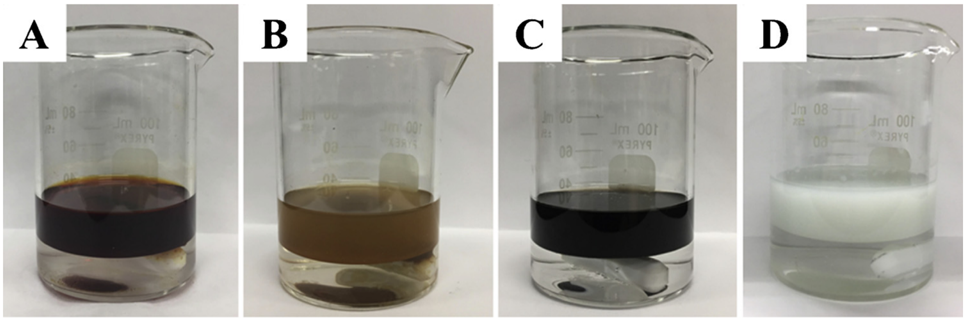

Fig. 3. Extracted materials: (A) FeOOH, (B) Mn_3O_4, (C) MnO_2, (D) ZnO.

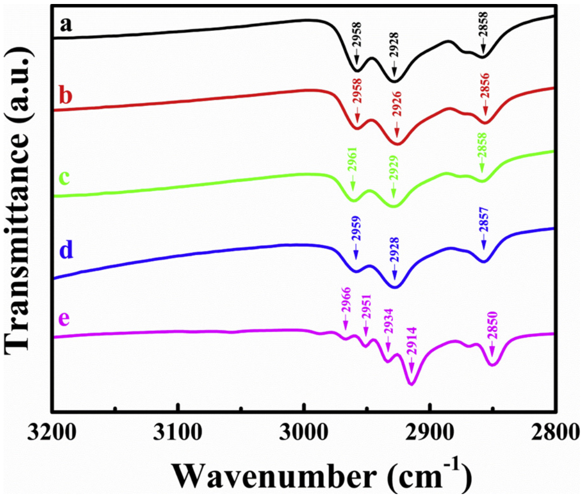

Fig. 4. FTIR spectra of extracted (a) FeOOH, (b) Mn_3O_4, (c) MnO_2, (d) ZnO and as-received (e) OG.

of adsorbed OG. Similar absorptions were observed in the spectrum of as-received OG.

The suspensions of extracted FeOOH, Mn_3O_4 and MnO_2 were used for the fabrication of electrodes of electrochemical supercapacitors. FeOOH is currently under investigation for the charge storage in the negative electrodes [30,31]. It is known that Mn_3O_4 and MnO_2 are promising materials for the positive electrodes [8]. Recent studies suggested that active mass loadings above 10–20 mg cm^{-2} are necessary for practical applications [32,33]. However, specific capacitance decreases drastically with increasing active mass [34] due to low electronic and ionic conductivities of the oxide and hydroxide materials. In this investigation the active mass of the electrodes was 36 mg cm^{-2}. The use of PELLI allowed reduced particle agglomeration, which facilitated electrolyte access to the particle surface. Moreover, reduced agglomeration allowed improved mixing of the oxide or hydroxide materials with conductive MWCNT additives. Fig. 5 shows microstructures of the electrodes, which were obtained by impregnation of Ni foam current collectors with active materials and pressing to 30% of original Ni foam thickness. The SEM images showed porous microstructures, which were beneficial for the electrolyte access to the metal oxide or hydroxide nanoparticles. MWCNT formed a secondary conductivity network inside the conductive Ni foam current collectors.

Fig. 6A shows CV for the FeOOH-MWCNT electrode. The CV deviates from the ideal box shape. However, the large area of the CV indicated relatively high capacitance. The highest capacitance of 2.4 F cm^{-2} was obtained (Fig. 6B) at a scan rate of 2 mV s^{-1}. The capacitance decreased with increasing scan rate due to diffusion limitation of electrolyte in pores.

The slope of the Nyquist plot of complex impedance was close to 45°, which indicated significant influence of Warburg impedance (Fig. 7A). The capacitance calculated from the impedance data

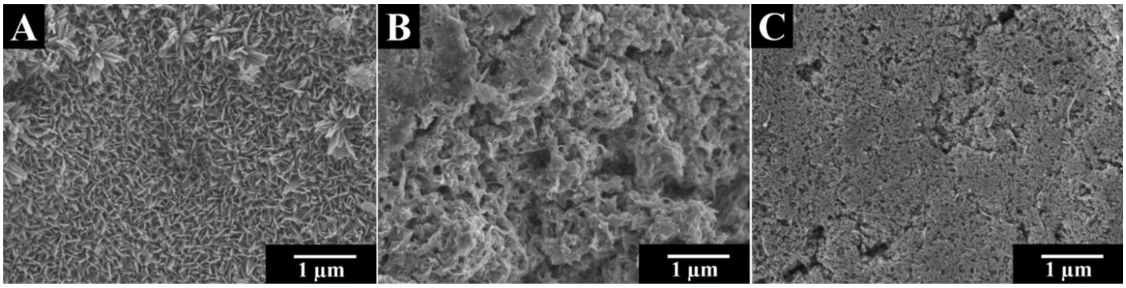

Fig. 5. SEM images of electrode surface for (A) FeOOH-MWCNT, (B) Mn_3O_4-MWCNT, and (C) MnO_2-MWCNT.

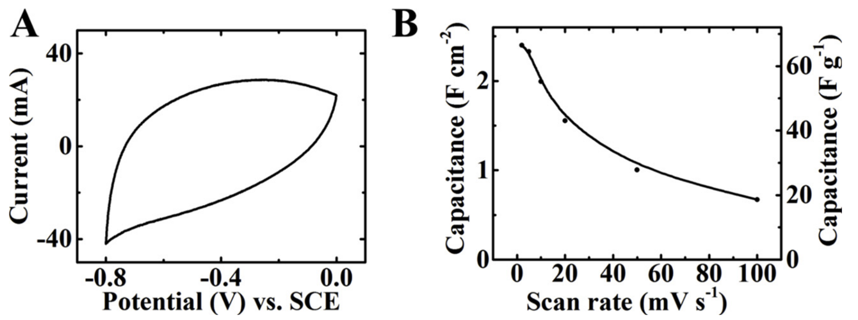

Fig. 6. (A) CV at a scan rate of 10 mVs^{-1} and (B) capacitance versus scan rate for FeOOH electrode.

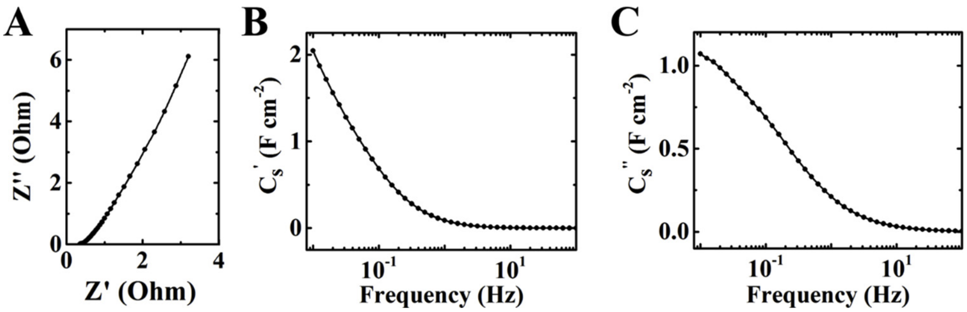

Fig. 7. (A) Nyquist plot of complex impedance and frequency dependences of (B) C_S' and (C) C_S'' calculated from the impedance data for FeOOH-MWCNT electrode.

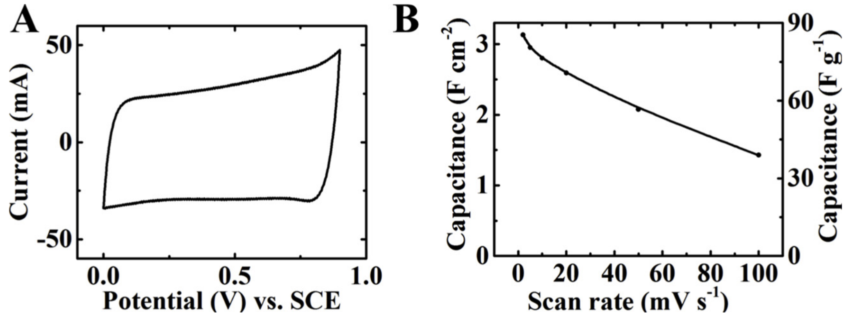

Fig. 8. (A) CV at a scan rate of 10 mVs^{-1} and (B) capacitance versus scan rate for the Mn_3O_4 –MWCNT electrode.

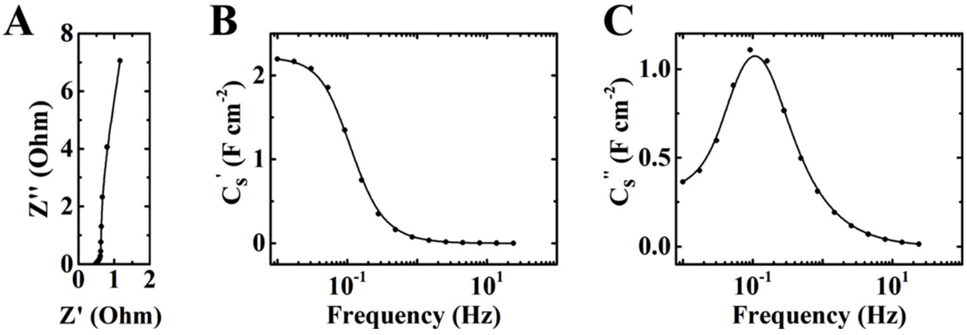

Fig. 9. (A) Nyquist plot of complex impedance and frequency dependences of (B) C_S' and (C) C_S'' calculated from the impedance data for Mn_3O_4 –MWCNT electrode.

decreased with increasing frequency. The real component of complex capacitance, measured at low frequencies, was comparable with capacitance calculated from the CV data at low scan rates.

Fig. 8A shows CV for the Mn_3O_4 –MWCNT electrode. The nearly box shape of the CV indicated good capacitive behavior. A capacitance of 3.1 Fcm^{-2} was achieved (Fig. 8B) at a scan rate of 2 mV s^{-1}. The capacitance retention at 100 mV s^{-1} was 48%. The relatively high capacitance retention at high scan rates resulted from enhanced mixing of Mn_3O_4 prepared usng PELLI, with conductive MWCNT additive.

The slope of the Nyquist plot of complex impedance was close to 90° and indicated good capacitive behavior (Fig. 9A). Of particular importance was low resistance R = Z´, which was achieved at high active mass loading. The frequency dependences of $C_S´$ and $C_S´´$ showed characteristics of relaxation type dispersion (Fig. 9B,C), such as reduction of $C_S´$ with frequency and relaxation maximum in $C_S´´$.

Fig. 10A shows CV for MnO_2 –MWCNT electrode. The CV has a nearly ideal box shape and relatively large area, which indicated high capacitance. The capacitance of the MnO_2 –MWCNT electrode showed the highest capacitance of 5.7 F cm^{-2} at a scan rate of 2 mV s^{-1} (Fig. 10 B). The capacitance retention at 100 mV s^{-1} was about 30%. The slope

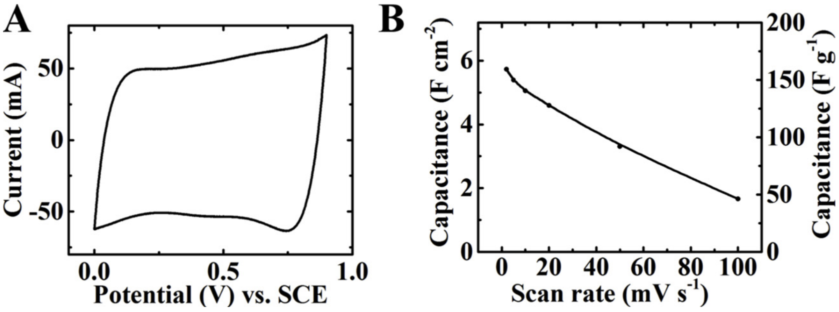

Fig. 10. (A) CV at a scan rate of 10 mVs^{-1} and (B) capacitance versus scan rate for the MnO_2 –MWCNT electrode.

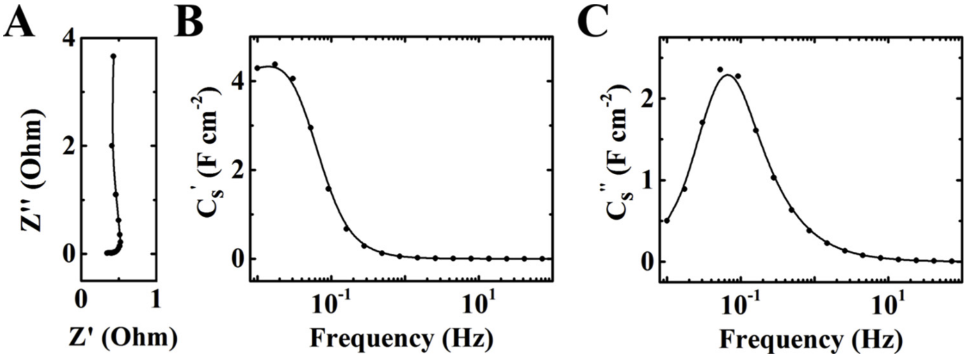

Fig. 11. (A) Nyquist plot of complex impedance and frequency dependences of (B) C_S' and (C) C_S'' calculated from the impedance data for MnO_2 –MWCNT electrode.

of the Nyquist plot of complex impedance was close to 90° and electrode resistance R = Z´ was relatively low (Fig. 11A). The frequency dependences of the components of complex capacitance showed a relaxation type dispersion and relatively high C_S of 4.2 F cm^{-2} was obtained at low scan rates. Therefore, impedance data confirmed good capacitive behavior of the MnO_2 –MWCNT electrodes. It is important to note that at low scan rates the MnO_2 –MWCNT electrodes showed significantly higher capacitance, compared to the capacitance of Mn_3O_4–MWCNT electrodes. However, the electrodes showed comparable capacitances at a scan rate of 100 mV s^{-1}. The capacitances of positive MnO_2–MWCNT and Mn_3O_4–MWCNT electrodes were higher, compared to the capacitance of FeOOH-MWCNT electrodes at the same active mass loading and in the same electrolyte. Therefore, further progress is necessary in the development of negative electrodes for the optimization of the device performance.

The use of PELLI allowed the development of electrodes with relatively high areal capacitances. This was attributed to reduced agglomeration of the ceramic nanoparticles and improved mixing of the nanoparticles with MWCNT. As a result, in comparison with literature data [35–41] good electrochemical performance was achieved at high active mass loadings. The high frequency resistance was below 0.5 O for all the electrodes studied.

OG is a versatile extractor material, which allowed efficient extraction of FeOOH, MnO_2, Mn_3O_4 and ZnO. The use of PELLI is promising for applications of ZnO in biosensors. The co-extraction of different oxide materials using OG can potentially result in the development of advanced ceramic composites. It is expected that PELLI can be used for extraction of other ceramic materials for advanced applications. Moreover, our investigations revealed interesting properties of OG, which can be used for the application of PELLI for the fabrication of ceramic-metal composites. The experimental data presented in the supporting information indicated that galloyl groups of OG can reduce Ag^+ ions to Ag at the interface of aqueous $AgNO_3$ solutions and n-butanol and simultaneously extract the Ag particles to the n-butanol phase. Therefore, the interface synthesis of Ag and co-extraction with ceramic particles can result in the development of advanced composites, containing Ag nanoparticles in ceramic matrix. Such composites are currently under investigation for catalysis [42], photocatalysis [43], supercapacitors [44], sensors [45], biomedical devices [46], batteries [47] and antimicrobial agents [48]. It is expected that the use of PELLI will facilitate the fabrication of such nanocomposites, reduce agglomeration and improve mixing of the individual components.

4. Conclusions

OG is a versatile and efficient extracting agent for the liquid-liquid extraction of various ceramic materials. The anchoring galloyl groups of OG allowed for strong OG adsorption on MnO_2, Mn_3O_4, FeOOH and ZnO particles and facilitated particle transfer from the aqueous syntheses medium to the n-butanol phase. The use of OG is promising for the fabrication of ceramic-ceramic, ceramic-metal and ceramic-MWCNT composites. FeOOH-MWCNT, MnO_2-MWCNT, and Mn_3O_4-MWCNT composites were prepared and tested for electrodes of electrochemical supercapacitors. The problems related to particle agglomeration were avoided using the PELLI method, which allowed the fabrication of electrodes with high active mass loadings. Reduced particle agglomeration allowed improved electrolyte access to the particle surface and facilitated mixing of the ceramic materials and MWCNT. As a result, the supercapacitor electrodes with high active mass loadings showed relatively high areal capacitances.

Acknowledgment

The authors gratefully acknowledge the financial support of the Natural Sciences and Engineering Research Council of Canada.

References

[1] J.-P. Jolivet, S. Cassaignon, C. Chaneac, D. Chiche, E. Tronc, Design of oxide nanoparticles by aqueous chemistry, J. Sol-Gel Sci. Technol. 46 (2008) 299–305.

[2] A. Abbasi, M. Hamadanian, M. Salavati-Niasari, S. Mortazavi-Derazkola, Facile size-controlled preparation of highly photocatalytically active $ZnCr_2O_4$ and $ZnCr_2O_4$/Ag

nanostructures for removal of organic contaminants, J. Colloid Interface Sci. 500 (2017) 276–284.
[3] Z. Huang, Y. Zhao, Y. Song, J. Zhao, Synthesis of Co_3O_4 nanoclusters via an EDTANa4-assisted route for enhanced electrochemical application, J. Colloid Interface Sci. 500 (2017) 142–149.
[4] Y. Su, I. Zhitomirsky, Hybrid MnO_2/carbon nanotube-VN/carbon nanotube supercapacitors, J. Power Sources 267 (2014) 235–242.
[5] Y. Xu, J. Sheng, X. Yin, J. Yu, B. Ding, Functional modification of breathable polyacrylonitrile/polyurethane/TiO_2 nanofibrous membranes with robust ultraviolet resistant and waterproof performance, J. Colloid Interface Sci. 508 (2017) 508–516.
[6] S. Sirohi, R. Singh, N. Jain, B. Pani, K. Dutt, R. Nain, Synthesis and characterization of multifunctional ZnO/polyester green composite films, J. Polym. Res. 24 (193) (2017) 191-110.
[7] J.-Y. Chung, J.-G. Lee, Y.-K. Baek, P.-W. Shin, Y.-K. Kim, Magnetic field-induced enhancement of thermal conductivities in polymer composites by linear clustering of spherical particles, Compos. Part B: Eng. 136 (2018) 215–221.
[8] J. Milne, I. Zhitomirsky, Application of octanohydroxamic acid for liquid-liquid extraction of manganese oxides and fabrication of supercapacitor electrodes, J. Colloid Interface Sci. 515 (2018) 50–57.
[9] Y. Hou, C. Hou, Y. Fan, F. Dang, B.-W. Li, Biphasic liquid interface derived magnetite nanocrystals: synthesis, properties and growth mechanism, Mater. Res. Express 4 (2017) 125028.
[10] B. Basly, D. Felder-Flesch, P. Perriat, G. Pourroy, S. Begin-Colin, Properties and suspension stability of dendronized iron oxide nanoparticles for MRI applications, Contrast Media Mol. Imaging 6 (2011) 132–138.
[11] R. Bhandary, J. Alauzun, P. Hesemann, A. Stocco, M. In, P.H. Mutin, Phase transfer of TiO_2 nanoparticles from water to ionic liquid triggered by phosphonic acid grafting, Small 13 (2017) 8023–8026.
[12] Cl.Schmitt Pauly, A.-C. Genix, J.G. Alauzun, G. Guerrero, M.-S. Appavou, J. Perez, J. Oberdisse, P.H. Mutin, Simultaneous phase transfer and surface modification of TiO_2 nanoparticles using alkylphosphonic acids: optimization and structure of the organosols, Langmuir 31 (2015) 10966–10974.
[13] B.P. Lee, P.B. Messersmith, J.N. Israelachvili, J.H. Waite, Mussel-inspired adhesives and coatings, Annu. Rev. Mater. Res. 41 (2011) 99–132.
[14] H. Lee, S.M. Dellatore, W.M. Miller, P.B. Messersmith, Mussel-inspired surface chemistry for multifunctional coatings, Science 318 (2007) 426–430.
[15] H. Lee, B.P. Lee, P.B. Messersmith, A reversible wet/dry adhesive inspired by mussels and geckos, Nature 448 (2007) 338–341.
[16] H. Lee, N.F. Scherer, P.B. Messersmith, Single-molecule mechanics of mussel adhesion, Proc. Natl. Acad. Sci. 103 (2006) 12999–13003.
[17] L. Petrone, Molecular surface chemistry in marine bioadhesion, Adv. Colloid Interface Sci. 195–196 (2013) 1–18.
[18] Q. Ye, F. Zhou, W. Liu, Bioinspired catecholic chemistry for surface modification, Chem. Soc. Rev. 40 (2011) 4244–4258.
[19] M. Ata, Y. Liu, I. Zhitomirsky, A review of new methods of surface chemical modification, dispersion and electrophoretic deposition of metal oxide particles, RSC Adv. 4 (2014) 22716–22732.
[20] K.V. Korpany, F. Habib, M. Murugesu, A.S. Blum, Stable water-soluble iron oxide nanoparticles using tiron, Mater. Chem. Phys. 138 (2013) 29–37.
[21] S. Varaganti, G. Ramakrishna, Dynamics of interfacial charge transfer emission in small molecule sensitized TiO_2 nanoparticles: Is it localized or delocalized? J. Phys. Chem. C 114 (2010) 13917–13925.
[22] X. Zhang, Y. Hou, P. Hu, C. Hong, Dispersion and interaction of ZrB_2 nanopowders with gallic acid in n-butanol, J. Eur. Ceram. Soc. 32 (2012) 3463–3468.
[23] Y. Wang, I. Zhitomirsky, Effect of phenolic molecules on electrophoretic deposition of manganese dioxide-carbon nanotube nanocomposites, Colloids Surf. A 369 (2010) 211–217.
[24] A. Hayat, D. Andreescu, G. Bulbul, S. Andreescu, Redox reactivity of cerium oxide nanoparticles against dopamine, J. Colloid Interface Sci. 418 (2014) 240–245.
[25] E. Tombacz, I.Y. Toth, D. Nesztor, E. Illes, A. Hajdu, M. Szekeres, L. Vekas, Adsorption of organic acids on magnetite nanoparticles, pH-dependent colloidal stability and salt tolerance, Colloids Surf. A: Physicochem. Eng. Aspects 435 (2013) 91–96.
[26] L. Zhao, J. Hu, B. He, Effect of electrical characteristics modification on viscosity of kaolin suspension, Adv. Mater. Res. 335–336 (2011) 1262–1266.
[27] K. Wu, Y. Wang, I. Zhitomirsky, Electrophoretic deposition of TiO_2 and composite TiO_2-MnO_2 films using benzoic acid and phenolic molecules as charging additives, J. Colloid Interface Sci. 352 (2010) 371–378.
[28] J.A. Arguello, A. Cerpa, M.H. Alanbari, J.C. Farinas, R. Moreno, Preparation of manganese oxide - graphite electrodes by electrophoretic deposition, Ceram. Int. 43 (2017) 3231–3237.
[29] M. Giza, P. Thissen, G. Grundmeier, Adsorption kinetics of organophosphonic acids on plasma-modified oxide-covered aluminum surfaces, Langmuir 24 (2008) 8688–8694.
[30] R. Barik, B.K. Jena, M. Mohapatra, Metal doped mesoporous FeOOH nanorods for high performance supercapacitors, RSC Adv. 7 (2017) 49083–49090.
[31] Z.C. Li, S.S. Chen, A.J. Gu, Z.X. Wang, X.H. Chen, Facile hydrothermal synthesis and electrochemical properties of hollow urchin-like α-FeOOH, IET Micro Nano Lett. 7 (2012) 757–761.
[32] Y. Gogotsi, P. Simon, True performance metrics in electrochemical energy storage, Science 334 (2011) 917–918.
[33] L. Wei, G. Yushin, Nanostructured activated carbons from natural precursors for electrical double layer capacitors, Nano Energy 1 (2012) 552–565.
[34] Y. He, W. Chen, X. Li, Z. Zhang, J. Fu, C. Zhao, E. Xie, Freestanding three-dimensional graphene/MnO_2 composite networks as ultralight and flexible supercapacitor electrodes, ACS Nano 7 (2012) 174–182.
[35] J. Cao, X. Li, Y. Wang, F.C. Walsh, J.-H. Ouyang, D. Jia, Y. Zhou, Materials and fabrication of electrode scaffolds for deposition of MnO_2 and their true performance in supercapacitors, J. Power Sources 293 (2015) 657–674.
[36] J.-G. Wang, F. Kang, B. Wei, Engineering of MnO_2-based nanocomposites for high-performance supercapacitors, Prog. Mater Sci. 74 (2015) 51–124.
[37] Q. Xia, M. Xu, H. Xia, J. Xie, Nanostructured iron Oxide/Hydroxide-based electrode materials for supercapacitors, ChemMedChem 2 (2016) 588–600.
[38] S. Yu, V.M.H. Ng, F. Wang, Z. Xiao, C. Li, L.B. Kong, W. Que, K. Zhou, Synthesis and application of iron-based nanomaterials as anodes of lithium-ion batteries and supercapacitors, J. Mater. Chemistry A 6 (2018) 9332–9367.
[39] Y. Zeng, M. Yu, Y. Meng, P. Fang, X. Lu, Y. Tong, Iron-based supercapacitor electrodes: advances and challenges, Adv. Energy Mater. 6 (2016) 1601053.
[40] W. Wei, X. Cui, W. Chen, D.G. Ivey, Manganese oxide-based materials as electrochemical supercapacitor electrodes, Chem. Soc. Rev. 40 (2011) 1697–1721.
[41] S. Zhang, G.Z. Chen, Manganese oxide based materials for supercapacitors, Energy Mater. 3 (2008) 186–200.
[42] R. Xu, X. Wang, D. Wang, K. Zhou, Y. Li, Surface structure effects in nanocrystal MnO_2 and Ag/MnO_2 catalytic oxidation of CO, J. Catal. 237 (2006) 426–430.
[43] S.A. Alzahrani, S.A. Al-Thabaiti, W.S. Al-Arjan, M.A. Malik, Z. Khan, Preparation of ultra long α-MnO2 and Ag@MnO2 nanoparticles by seedless approach and their photocatalytic performance, J. Mol. Struct. 1137 (2017) 495–505.
[44] Z. Guo, Y. Guan, C. Dai, J. Mu, H. Che, G. Wang, X. Zhang, Z. Zhang, X. Zhang, Ag/MnO_2 nanorod as electrode material for High-performance electrochemical supercapacitors, J. Nanosci. Nanotechnol. 18 (2018) 4904–4909.
[45] Q. Han, P. Ni, Z. Liu, X. Dong, Y. Wang, Z. Li, Z. Liu, Enhanced hydrogen peroxide sensing by incorporating manganese dioxide nanowire with silver nanoparticles, Electrochem. Commun. 38 (2014) 110–113.
[46] J. Ramalingam, M.-A. Vaali-Mohammed, H.A. Al-Lohedan, J.N. Appaturi, Synthesis and bio-physical characterization of Silver nanoparticle and Ag-mesoporous MnO_2 nanocomposite for anti-microbial and anti-cancer activity, J. Mol. Liq. 243 (2017) 348–357.
[47] S. Wang, J. Xie, T. Zhang, V.K. Varadan, Silver decorated γ-manganese dioxide nanorods for alkaline battery cathode, J. Power Sources 186 (2009) 532–538.
[48] Y.-W. Wang, C.-W. Chen, J. Hsieh, W.J. Tseng, Preparation of Ag/TiO_2 composite foams via Pickering emulsion for bactericide and photocatalysis, Ceram. Int. 43 (2017) S797–S801.

Chapter 6: Application of Octanohydroxamic Acid for Liquid-Liquid Extraction of Manganese Oxides and Fabrication of Supercapacitor Electrodes

Reprinted article with permission from J. Milne and I. Zhitomirsky, "Application of octanohydroxamic acid for liquid-liquid extraction of manganese oxides and fabrication of supercapacitor electrodes," *J. Colloid Interface Sci.*, vol. 515, pp. 50–57, 2018. DOI: 10.1016/j.jcis.2018.01.021

Author's Contributions

- Synthesis of electrode materials
- Electrochemical testing of electrodes
- FTIR and XRD of materials
- SEM imaging of electrode material
- Literature evaluation
- Preparation of manuscript draft

Journal of Colloid and Interface Science 515 (2018) 50–57

Contents lists available at ScienceDirect

Journal of Colloid and Interface Science

journal homepage: www.elsevier.com/locate/jcis

Regular Article

Application of octanohydroxamic acid for liquid-liquid extraction of manganese oxides and fabrication of supercapacitor electrodes

J. Milne, I. Zhitomirsky *

Department of Materials Science and Engineering, McMaster University, 1280 Main Street West, Hamilton, Ontario L8S 4L7, Canada

GRAPHICAL ABSTRACT

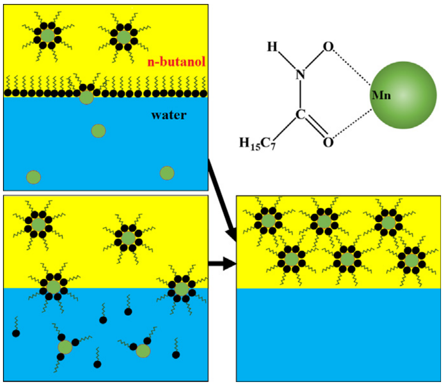

ARTICLE INFO

Article history:
Received 30 November 2017
Revised 30 December 2017
Accepted 5 January 2018
Available online 6 January 2018

Keywords:
Manganese oxide
Supercapacitor
Adsorption
Extraction
Carbon nanotube
Composite

ABSTRACT

MnO_2 and Mn_3O_4 particles were prepared by wet chemical methods and efficiently dispersed and mixed with multiwalled carbon nanotubes (MWCNT) for the fabrication of composite MnO_2-MWCNT and Mn_3O_4-MWCNT electrodes for electrochemical supercapacitors (ES). The problem of particle agglomeration was addressed by particle extraction through a liquid-liquid interface (PELLI) using octanohydroxamic acid (OHA) as a new extractor. OHA exhibited remarkable adsorption on particles due to a bidentate bonding mechanism. The use of OHA broadened the application of PELLI technology, because it allowed good extraction of particles from an aqueous phase at high pH. Moreover, OHA allowed efficient extraction by strong adsorption on particles not only at the liquid-liquid interface, but also in the bulk of an aqueous phase. Building on the advantages offered by the PELLI method and OHA as an extractor we found that Mn_3O_4-MWCNT electrodes exhibited a remarkably high capacitance of 4.2F cm^{-2}. Another major finding was that capacitance of Mn_3O_4-MWCNT electrodes was higher than that of MnO_2-MWCNT electrodes at active mass of 33 mg cm^{-2}. This finding showed processing advantages of PELLI and paved the way for applications of novel colloidal and surface modification strategies for the development of advanced ES. A conceptually new approach has been proposed based on the use of hydroxamic acids as capping agents for synthesis and extractor molecules for PELLI.

1. Introduction

Aqueous synthesis techniques are widely used for the fabrication of metal oxide and hydroxide particles, quantum dots and

---

* Corresponding author.
E-mail address: zhitom@mcmaster.ca (I. Zhitomirsky).

https://doi.org/10.1016/j.jcis.2018.01.021

nanoparticles of metals [1–5]. In many applications [6–10], the particles formed in an aqueous phase are transferred to an organic solvent, containing dissolved polymers and other functional components for the fabrication of composite materials. The use of polymers, which are soluble only in organic solvents, facilitates the fabrication of composites for applications in devices with improved moisture stability. The use of organic solvents is critical for the manufacturing of materials and devices, which require stable operation in aqueous environment, such as electrodes of supercapacitors and batteries, protective coatings, implants and other composite materials and devices containing water insoluble polymers as binders or functional components [11,12]. Organic solvents offer many advantages for tape casting and other colloidal techniques, due to superior binding properties of polymers that are soluble in organic solvents, compared to water soluble polymer binders. Organic solvents are beneficial for various film deposition methods, such as spin casting [13], electrophoretic deposition [14,15], spray deposition [16] and dip coating [17]. Therefore, for many advanced applications the particles formed in an aqueous phase must be washed, dried and then re-dispersed in an organic phase. However, drying procedure introduces problems related to particle agglomeration. The reduction of surface energy of particles and condensation reactions of surface OH groups are major reasons of the agglomeration.

Particle extraction through liquid-liquid interface (PELLI) [18] provides the capability of transferring particles from an aqueous synthesis medium directly to an organic phase, thus avoiding the drying procedure and agglomeration of the particles. Studies in this area focused on the development of extractor molecules with specific anchoring groups, selection of receiving solvents and development of new extraction mechanisms. Nanoparticles of gold [19,20], silver [21] and quantum dots [22] were transferred to organic media using fatty acid, alkanethiol and alkylamine molecules as extractors. Fatty acids were investigated for the extraction of magnetite [23]. Various co-solvents were used in order to enhance the extraction efficiency [22,24]. The extraction mechanisms involved various extractor-particle interactions, such as covalent [20,21], electrostatic [25] and ion-pair interactions [26].

PELLI is especially attractive for agglomerate free processing of oxide and hydroxide materials. A relatively recent development is the application of lauryl gallate [27–29] and alkylphosphonic acids [29–31] for the extraction of metal oxides and hydroxides. These new extractors offered an advantage of strong polydentate bonding to the particle surface. Top-down and bottom-up PELLI methods were developed [18]. In another approach [18,28,32] particles were modified in-situ during synthesis with aldehyde molecules, containing anchoring catechol groups and then in a Schiff base formation reaction with extractor molecules at the interface of two immiscible liquids. From these prior investigations, it appears that PELLI can be used for the development of advanced metal oxide-polymer nanocomposites.

The choice of anchoring groups of the extractor molecules plays a crucial role in controlling the extractor adsorption on particles. So far PELLI was applied to a limited number of oxide materials. It is important to note that alkanethiols do not adsorb on the surfaces of oxides [33]. Fatty acids and alkylphosphonic acids showed relatively weak adsorption on oxides [33]. The important task is to develop a larger pool of extractor molecules and find more efficient extractors, which allow strong adsorption on various inorganic materials for PELLI applications. Understanding the extraction mechanisms and development of new extraction strategies are critical factors for the further advances in the PELLI methods.

The goal of this study was the application of octanohydroxamic acid (OHA) as a new extractor for PELLI and analysis of fundamental extraction mechanisms. Another target of this investigation was the application of OHA as an extractor in the PELLI method for the development of ES. We explored different extraction strategies and proposed extraction mechanisms. In contrast to previous studies, which involved the lauryl gallate and alkylphosphonic acids adsorption on particles at the interface of two immiscible liquids, we found that OHA can penetrate the interface. We provided experimental evidence that OHA adsorbed on the particles not only at the interface but also in the bulk of an aqueous phase. This finding indicated that long chain extractors from the hydroxamic acid family can potentially be used as capping agents for synthesis in an aqueous phase and extractors in the PELLI method. We discussed benefits of OHA and related molecules for the fabrication of advanced nanocomposites by PELLI method. Another important finding of this investigation was the development of advanced ES electrodes. The experimental results described below indicated that OHA allowed efficient extraction of MnO_2 and Mn_3O_4 and fabrication of composite electrodes, which showed promising performance for ES applications.

2. Experimental procedures

Reagent grade purity $KMnO_4$, $Mn(NO_3)_2$, poly(vinyl butyral-*co*-vinyl alcohol-*co*-vinyl acetate) (PVB, average Mw = 50,000–80,000), NaOH, *n*-butanol (Aldrich, Canada), octanohydroxamic acid (OHA) (TCI America) were used. Multiwalled carbon nanotubes (MWCNT, ID 4 nm, OD13 nm, length 1–2 μm, 98% purity) were supplied by Bayer, Germany. Ni foams with 95% porosity were provided by Vale Limited Company.

For the fabrication of MnO_2 particles, 1 g $KMnO_4$ was dissolved in 30 mL of water and then 20 mL of *n*-butanol was added. The reduction of Mn^{7+} species by *n*-butanol [27] resulted in the formation of MnO_2 particles, which precipitated in the aqueous phase. The procedure for synthesis of Mn_3O_4 particles was described in a previous investigation [28]. OHA was used as a new extractor for PELLI method. The MnO_2 and Mn_3O_4 particles, synthesized in aqueous solutions, were transferred to *n*-butanol using OHA as an extractor.

The suspensions for electrode fabrication contained 80% MnO_2 or Mn_3O_4, extracted from the aqueous phase, and 20% MWCNT in *n*-butanol. PVB binder, dissolved in ethanol was added to the mixture, the PVB content was 3% of the total mass of the MnO_2-MWCNT or Mn_3O_4-MWCNT electrodes. The obtained slurries were used for the impregnation of Ni foam current collectors. The total mass of the impregnated material was 33 mg cm^{-2}. Materials characterization and electrochemical testing techniques were described in previous investigations [28,34].

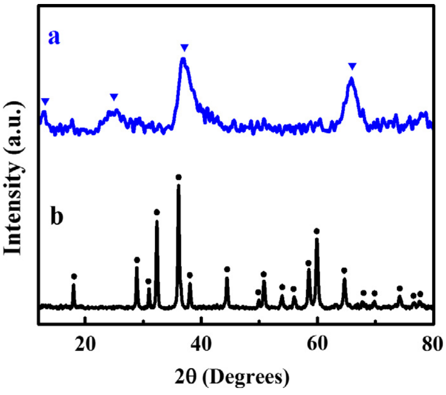

Fig. 1. X-ray diffraction patterns of (a) MnO_2 (▼-JCPDS file 00-023-1046) and (b) Mn_3O_4 (●-JCPDS file 04-007-1841).

3. Results and discussion

Fig. 1 presents X-ray diffraction patterns of MnO_2 and Mn_3O_4. The diffractogram of MnO_2 showed peaks, corresponding to the JCPDS file 00-023-1046. However, the material exhibited poor crystallinity. The diffractogram of Mn_3O_4 showed peaks, corresponding to the JCPDS file 04-007-1841. The dried powders, used for XRD were agglomerated. Therefore, a PELLI method has been developed for the extraction of as-precipitated powders from water directly to an organic phase in order to avoid particle agglomeration during the drying process.

This work represents the first attempt to use hydroxamic acids for the extraction of particles in the PELLI method. We were inspired by strong complexing properties of various hydroxamic acids, such as OHA. Therefore, OHA was investigated as a new extractor for the extraction of MnO_2 and Mn_3O_4 in the PELLI method. Water immiscible *n*-butanol was used as a receiving solvent, which has a density lower than water. The addition of OHA solution in *n*-butanol to the aqueous phase resulted in extraction of particles from the aqueous to *n*-butanol phase (Fig. 2). The mass ratio of manganese oxide: extractor was 3:1. It was suggested that OHA adsorbed on manganese oxide particles and facilitated their transfer to the organic phase.

OHA belongs to the family of hydroxamic acids. Fig. 3A shows a chemical structure of OHA, which includes a carbonyl group, alkyl chain and NOH_2 group. According to the literature, hydroxamic acids, such as OHA formed complexes with metal atoms and showed significantly larger metal complexation constants, compared to carboxylic acids [33]. It was found that hydroxamic acids formed stable monolayers on various oxides and showed significantly stronger adsorption, compared to other acids [33]. The adsorption mechanism of hydroxamic acids was based on the complexation of metal atoms on the particle surface. The complex formation [35] involved the replacement of H^+ by the metal ion and ring closure via the carbonyl oxygen (Fig. 3B). As a result, the hydroxamic acid adsorption involved strong bidentate bonding [36]. Hydroxamic acids showed enhanced adsorption on oxides at high pH, especially at pH > isoelectric point, despite the electrostatic repulsion of anionic hydroxamic acids and negatively charged oxide surfaces [36–38]. It will be shown below that such unique behavior opens interesting opportunities in the PELLI technology.

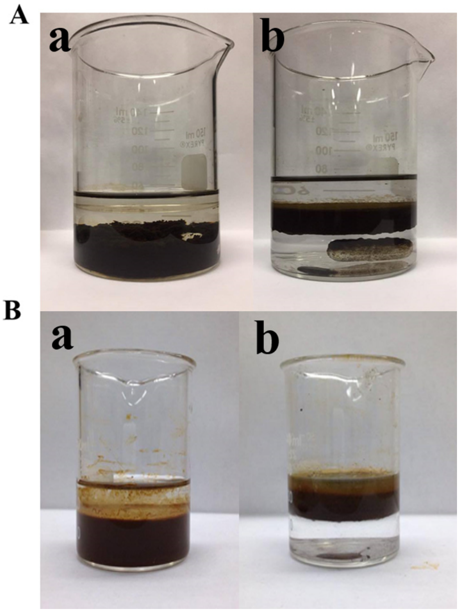

Fig. 2. (A) MnO_2 and (B) Mn_3O_4: (a) as-precipitated and (b) extracted.

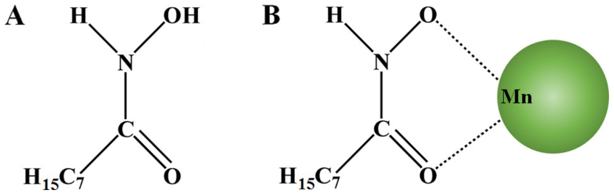

Fig. 3. (A) Chemical structure of OHA and (B) adsorption mechanism of OHA, involving complexation of Mn atoms on the particle surface.

Two different mechanisms of extraction were suggested. In the A-B1-C mechanism (Fig. 4), an extractor was accumulated at the water-*n*-butanol interface (Fig. 4B1) with the hydrophilic groups exposed to water and the hydrophobic tail extended out of the water phase into the *n*-butanol phase. The orientation and accumulation of the extractor molecules at the interface of two liquids promoted their adsorption on particles (Fig. 4B1), which were then transferred to the *n*-butanol (Fig. 4C). A similar mechanism was proposed in experiments, involving lauryl gallate and alkylphosphonic acids extractors [27,28,30]. However, OHA is soluble in water at high pH and similar to other hydroxamic acids can be adsorbed on particles even at pH > isoelectric point [36–38]. Therefore, A-B2-C mechanism (Fig. 4) can also be suggested. In such mechanism OHA penetrated the *n*-butanol-water interface and dissolved in the aqueous phase at a high pH. It was suggested that OHA was adsorbed on particles in the aqueous phase (Fig. 4B2) and then the particles were transferred to the *n*-butanol phase (Fig. 4C).

In order to prove the feasibility of the A-B2-C mechanism, an additional experiment was performed, which was illustrated in Fig. 5. In this experiment, OHA was dissolved in aqueous NaOH solution (Fig. 5A) and added to $Mn(NO_3)_2$ solution (Fig. 5B). The final pH of the mixed solution was pH = 10. In this case, OHA modified Mn_3O_4 particles were formed in the aqueous phase (Fig. 5C). The addition of *n*-butanol, followed by stirring resulted in particle extraction to the *n*-butanol phase (Fig. 5D). Therefore, this experiment showed the feasibility of the A-B2-C mechanism. Moreover, the experiment described in Fig. 5 indicated that hydroxamic acids with larger size can potentially be used as capping agents for synthesis of nanoparticles and extractors for the nanoparticle extraction in the PELLI method.

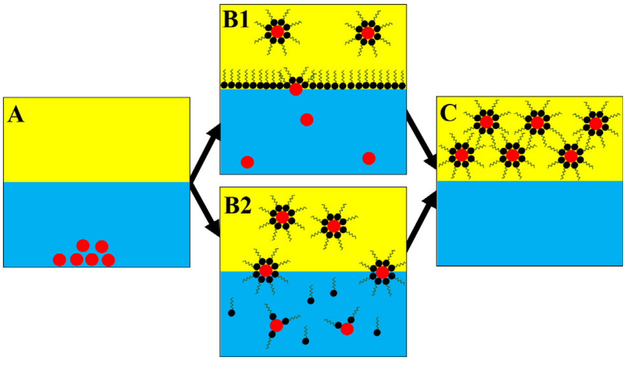

Fig. 4. Suggested mechanisms A-B1-C and A-B2-C for the extraction: (A) precipitation of Mn_3O_4 particles in an aqueous phase, (B1) OHA is accumulated at the water-*n*-butanol interface and adsorbed on particles, the modified particles are transferred to *n*-butanol, (B2) OHA penetrates the water-*n*-butanol interface, dissolves in the aqueous phase at high pH, and adsorbs on the particles, the modified particles are transferred to the *n*-butanol, (C) particles, containing adsorbed OHA, completely transferred to *n*-butanol.

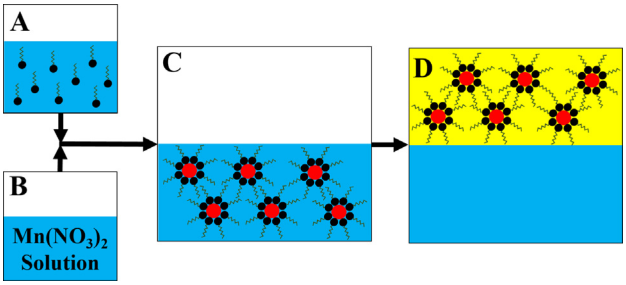

Fig. 5. Schematic of the extraction experiment: (A) OHA is dissolved in alkali and added to (B) $Mn(NO_3)_2$ solution, (C) Mn_3O_4 particles, modified with OHA are formed and (D) after addition of *n*-butanol the modified particles are transferred to the *n*-butanol phase.

The OHA adsorption on Mn_3O_4 was confirmed by the FTIR analysis of the extracted particles. The absorptions in the spectrum of OHA in the range of 2800–3000 cm^{-1} (Fig. 6a) were attributed to vibrations of CH_2 and CH_3 groups [39,40]. Similar adsorptions were observed in the spectra of extracted MnO_2 and Mn_3O_4 (Fig. 6b,c). Such absorptions indicated that extracted MnO_2 and Mn_3O_4 contained adsorbed OHA.

The suspensions of MnO_2 and Mn_3O_4 particles in *n*-butanol, prepared by synthesis in aqueous solutions and extracted to *n*-butanol using PELLI were utilized for the fabrication of electrodes of electrochemical supercapacitors. Fig. 7A shows CVs for MnO_2-MWCNT electrodes at different scan rates. The nearly box shapes of the CVs indicated good capacitive behavior. The MnO_2-MWCNT electrodes showed (Fig. 7B) a specific capacitance of 3.84F cm^{-2} at a scan rate of 2 mV s^{-1}. The capacitance decreased with increasing scan rate due to the diffusion limitations in the electrode. The capacitance of 1.42F cm^{-2} was obtained at a scan rate of 100 mV s^{-1}.

The analysis of the impedance data (Fig. 8A) showed relatively low electrode resistance Z′. The slope of the Nyquist plot was close to 90 °C, indicating good pseudocapacitive behavior. The analysis of frequency dependences of the components of the complex capacitance (Fig. 8B,C), derived from the impedance data showed a relaxation type dispersion [41], as indicated by the reduction of the real component of capacitance with frequency and corresponding maximum in the frequency dependence of the imaginary part. The real part of the capacitance, calculated from the impedance data at low frequencies (Fig. 8B) was comparable with capacitance, calculated from the CV data at low scan rates (Fig. 7B).

Mn_3O_4 showed an activation behavior [42], which resulted in capacitance increase of the Mn_3O_4-MWCNT composites during initial cycling. It is known [42,43] that activation behavior is attributed to surface oxidation of Mn_3O_4. Typical testing procedure (TP), involved CV testing at 2, 5, 10, 20, 50 and 100 mV s^{-1}. During the initial TPs the areas of CVs increased, indicating activation behavior, and remained practically unchanged after the 3rd TP. Fig. 9A shows CVs at different scan rates for TP4. The nearly box shapes of the CVs and increase in current with increasing scan rate indicated good capacitive behavior. The capacitances were calculated from the CVs and presented in Fig. 9B. The maximum in the capacitance versus scan rate dependence for the 1st TP and capacitance increase during the TPs 1–3 were attributed to the activation process. TP2 showed capacitance of 3.81F cm^{-2} at a scan rate of 2 mV s^{-1}, which was very close to the capacitance of MnO_2 –MWCNT electrodes. The capacitance of 4.20F cm^{-2} of Mn_3O_4-MWCNT electrodes was obtained for TP4 at a scan rate of 2 mV s^{-1}. The capacitance decreased to the value of 1.67F cm^{-2} at a scan rate of 100 mV s^{-1}.

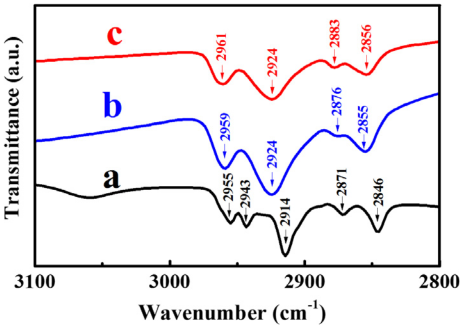

Fig. 6. FTIR spectra of (a) as-received OHA (b) MnO_2 extracted using OHA and (c) Mn_3O_4 extracted using OHA.

The analysis of the impedance data for the Mn_3O_4-MWCNT composites after TP4 showed (Fig. 10A) low resistance Z′. The Nyquist plot slope was close to 90° and indicated good pseudocapacitive behavior. The real and imaginary components of capacitance were calculated from the impedance data and plotted in the Bode plots in Fig. 10B,C. The frequency dependences of the AC capacitance components showed a relaxation type dispersion, due to the reduction of C′ with frequency and observed relaxation maximum in the corresponding C″ plot. The low frequency capacitance C′ of the Mn_3O_4-MWCNT electrodes was higher than that of MnO_2-MWCNT electrodes. This observation correlated with corresponding CV data.

The testing results presented above indicated that the activation of the Mn_3O_4-MWCNT electrodes resulted in enhanced electrochemical performance. Therefore, the electrode material was analyzed using XPS and SEM before and after the activation in order to obtain additional information on changes in the material resulting from cycling. The comparison of the XPS data (Fig. 11) for as-prepared electrodes and after TP4 revealed reduction in Mn^{2+} and Mn^{3+} content and increase in the Mn^{4+} content in the tested material. This observation is in agreement with literature data [43,44], which indicated that cycling in the Na_2SO_4 solutions resulted in the oxidation of surface Mn_3O_4 layer. The oxidation of Mn^{2+} and Mn^{3+} to form Mn^{4+} in the surface layer resulted in the variation of the capacitance of Mn_3O_4 during the initial cycling. SEM studies of the electrode microstructure before testing showed that electrode contained Mn_3O_4 primary nanoparticles mixed with MWCNT (Fig. 12A). Cycling resulted in drastic changes in the electrode microstructure. The tested electrode showed flaky porous morphology, which facilitated the electrolyte access to the capacitive material (Fig. 12B).

The results of this investigation showed that OHA can be successfully used for application in the PELLI technique. In this strategy the drying stage and related particle agglomeration were avoided. Reduced agglomeration is important for the fabrication of electrodes with high capacitance, because it allows good electrolyte access to the particle surface. However, it should be noted that several investigations [45–48] have shown that the capacitance does not correlate with the BET surface area, since very small pores are inaccessible by ions of the electrolyte. However, PELLI allowed the formation of dispersed particles and facilitated their mixing with conductive MWCNT. It was demonstrated in this investigation that OHA allowed good extraction of Mn_3O_4 particles at pH = 10. Therefore, OHA is a promising extractor for the extraction of other materials, which require high pH for chemical precipitation. This finding significantly broadened the range of PELLI applications.

The ability of OHA to adsorb on particles not only at the interface of the two liquids, but also in the bulk of an aqueous phase facilitated the extraction process. We suggested that OHA formed water-insoluble complexes with metal atoms on the particle surface and allowed for their extraction to the *n*-butanol phase. There

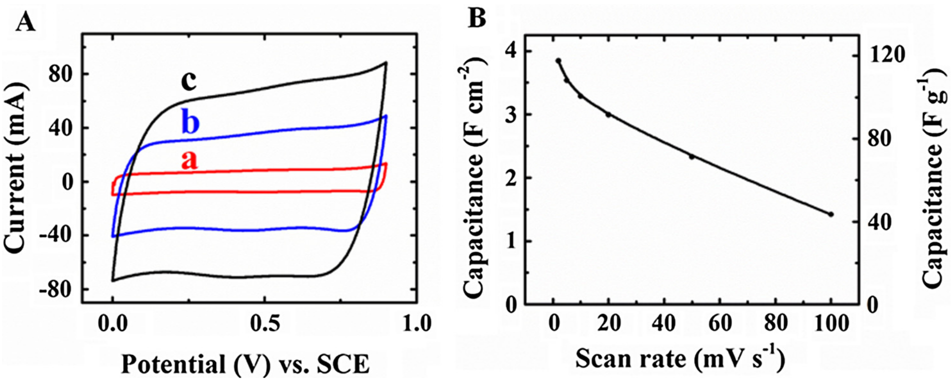

Fig. 7. (A) CVs at scan rates of (a) 2, (b) 10, and (c) 20 mV s^{-1}, (B) C_s and C_m, calculated from the CV data for MnO_2-MWCNT composites.

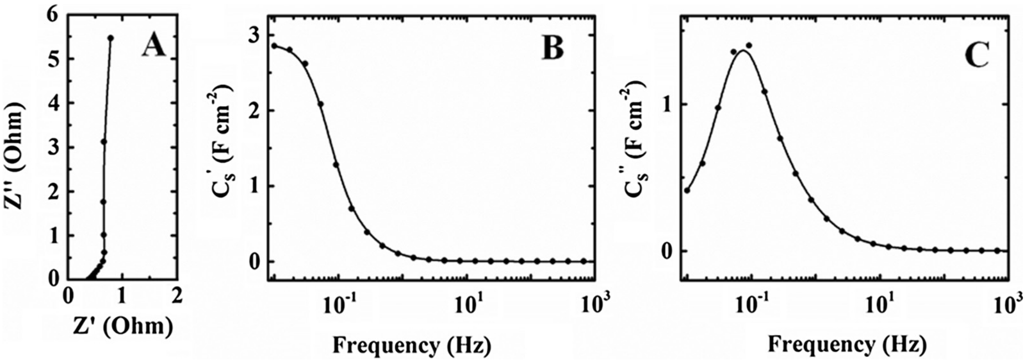

Fig. 8. (A) Nyquist plot of complex impedance and frequency dependences of (B) C'_s and (C) C''_s calculated from the impedance data for MnO_2-MWCNT composites.

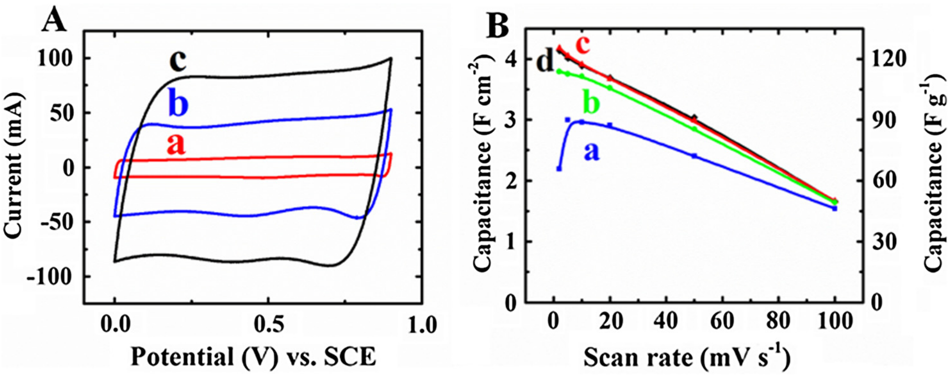

Fig. 9. (A) CVs at scan rates of (a) 2, (b) 10, and (c) 20 mV s^{-1} for TP4, (B) C_s and C_m, calculated from the CV data at different scan rates for (a) TP1, (b) TP2, (c) TP3 and (d) TP4 for Mn_3O_4-MWCNT composites.

is a good reason to expect that larger molecules from the hydroxamic acids family can be used as capping agents for the particle synthesis and extractors for their extraction to an organic phase. It is important to note that MnO_2 is usually synthesized by reduction of Mn^{7+} species in the $KMnO_4$ or $NaMnO_4$ solutions. It is known that permanganates react with many organic molecules and selection of capping agents for MnO_2 synthesis presents difficulties. In contrast, Mn_3O_4 is prepared from Mn^{2+} solutions, and various capping agents can be used for the control of particle size.

The use of OHA as an advanced extractor for PELLI allowed the extraction of non-agglomerated Mn_3O_4 particles, which improved Mn_3O_4 mixing with MWCNT and facilitated electrochemical activation. As a result, the areal capacitance of Mn_3O_4-MWCNT electrodes was higher, compared to the literature data. The areal capacitances, reported in the literature [49–56] were typically below 1F cm^{-2}. Higher capacitance of 1.7F cm^{-2} was achieved for electrodes, prepared by dip casting of Mn_3O_4 on CNT array [57]. In a previous investigation, we reported a capacitance of 2.8F cm^{-2} for the Mn_3O_4-MWCNT electrodes, prepared by an electrostatic heterocoagulation technique [42]. The areal capacitance of Mn_3O_4-MWCNT electrodes [28] with active mass loading of 30.4 mg cm^{-2}, prepared using PELLI technique and lauryl gallate extractor, was found to be 2.63F cm^{-2}. In this investigation we achieved a capacitance of 4.2F cm^{-2} for the Mn_3O_4–MWCNT composites which was higher than the capacitances reported in the previous studies. It is important to note that we achieved significantly lower impedance, compared to the previous investigations [49,54,55], despite the larger active mass loading of our electrodes. The capac-

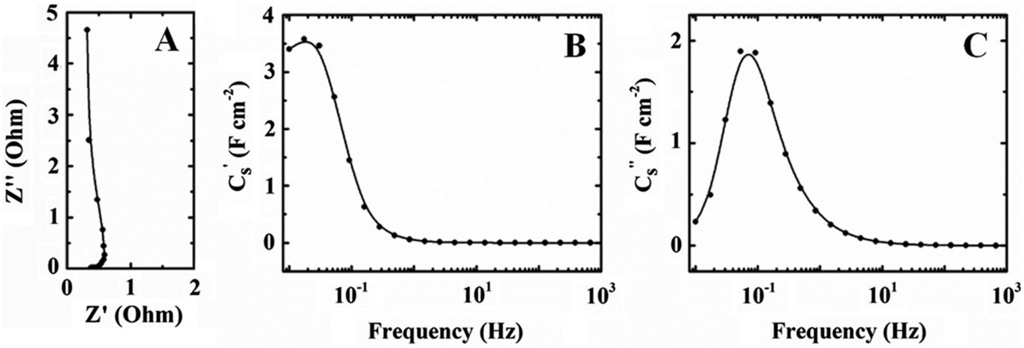

Fig. 10. (A) Nyquist plot of complex impedance and frequency dependences of (B) C'_s and (C) C''_s calculated from the impedance data for Mn_3O_4-MWCNT composites after TP4.

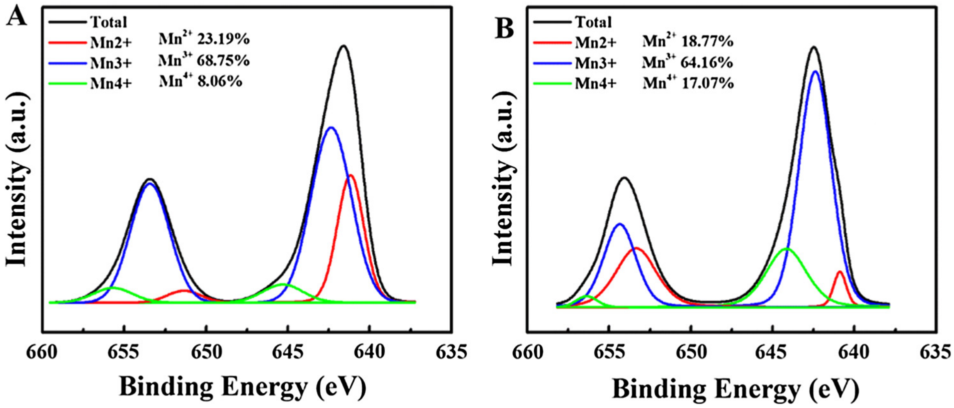

Fig. 11. XPS data for Mn_3O_4-MWCNT electrodes (A) before testing and (B) after TP4.

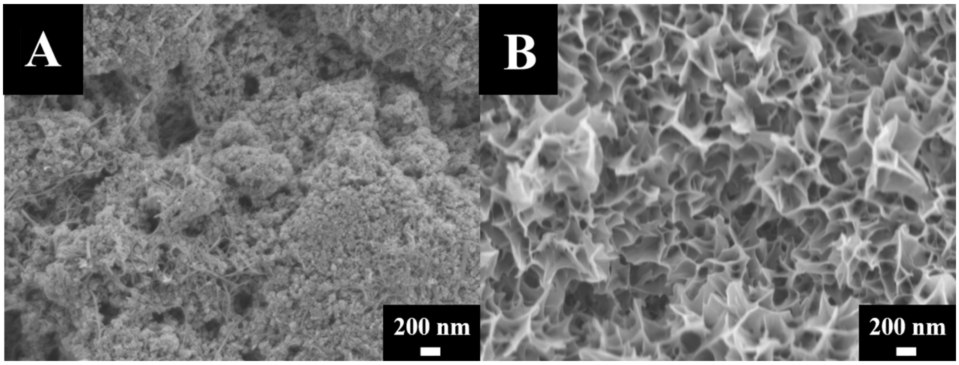

Fig. 12. SEM images of Mn_3O_4-MWCNT electrodes (A) before testing and (B) after TP4.

itances of MnO_2-MWCNT and Mn_3O_4-MWCNT electrodes, obtained at low scan rates, were comparable with capacitances, calculated from the impedance data at low frequencies.

Previous investigations showed that the capacitances of Mn_3O_4 based electrodes were typically significantly lower than capacitances of MnO_2 based electrodes. In contrast, in this investigation we achieved higher capacitance of Mn_3O_4-MWCNT electrodes, compared to MnO_2-MWCNT, prepared at similar conditions and at the same active mass loadings. It is suggested that reduced agglomeration of Mn_3O_4 particles, achieved using PELLI, allowed for better utilization of capacitive properties of this material. This result indicated that Mn_3O_4 is a promising charge storage material for ES and the development of new colloidal and surface modification techniques can potentially enhance the capacitive performance of Mn_3O_4-MWCNT electrodes. Therefore, it is expected that further development of PELLI and the use of other hydroxamic acids and derivatives as capping agents and extractors will allow further progress in the development of Mn_3O_4-MWCNT electrodes. As pointed out above, the application of organic dispersing and capping agents for the MnO_2 synthesis from permanganate solutions presents difficulties due to the highly reactive nature of the permanganate precursors.

4. Conclusions

OHA exhibited remarkable adsorption on MnO_2 and Mn_3O_4 particles due to a bidentate bonding mechanism. The feasibility of the application of OHA as an extractor for PELLI has been demonstrated. This has opened a path towards new applications of PELLI technology, because OHA allowed good extraction of particles from an aqueous phase at high pH. Moreover, OHA allowed efficient extraction by strong adsorption on particles not only at the water-*n*-butanol interface, but also in the bulk of an aqueous phase. The problem of particle agglomeration was avoided using PELLI method and OHA as a new extractor. The use of OHA for PELLI facilitated efficient dispersion of particles and their mixing with MWCNT, which allowed enhanced electrochemical performance. Moreover, reduced agglomeration facilitated electrochemical activation of Mn_3O_4. Mn_3O_4-MWCNT electrodes showed a high capacitance of 4.2F cm^{-2}. The high capacitance was achieved at low impedance and high active mass loadings, which are beneficial for supercapacitor applications. Another major finding was that capacitance of Mn_3O_4-MWCNT electrodes was higher than that of MnO_2-MWCNT electrodes at active mass of 33 mg cm^{-2}. This finding indicated promising performance of Mn_3O_4-MWCNT electrodes and paved the way for further advances in the supercapacitor technology. It provides evidence that processing advantages of Mn^{2+} precursors for Mn_3O_4 synthesis and mixing with MWCNT, can be combined with benefits of PELLI and other colloidal techniques for the fabrication of advanced ES. Especially promising for future applications in nanotechnology of composites is a conceptually new technique, which involved the use of hydroxamic acids as capping agents for particle synthesis and extractors for PELLI. We believe that the further applications of OHA and other hydroxamic acids for PELLI offer a versatile strategy for agglomerate free processing of other oxide and hydroxide materials, especially for the materials, which require synthesis at high pH.

Acknowledgements

We acknowledge NSERC Canada for the financial support.

References

[1] R. Pourfaraj, S.J. Fatemi, S.Y. Kazemi, P. Biparva, Synthesis of hexagonal mesoporous MgAl LDH nanoplatelets adsorbent for the effective adsorption of brilliant yellow, J. Colloid Interface Sci. 508 (2017) 65–74.

[2] A. Abbasi, M. Hamadanian, M. Salavati-Niasari, S. Mortazavi-Derazkola, Facile size-controlled preparation of highly photocatalytically active $ZnCr_2O_4$ and $ZnCr_2O_4$/Ag nanostructures for removal of organic contaminants, J. Colloid Interface Sci. 500 (2017) 276–284.

[3] B. Khodadadi, M. Bordbar, M. Nasrollahzadeh, Green synthesis of Pd nanoparticles at *Apricot kernel* shell substrate using *Salvia hydrangea* extract: catalytic activity for reduction of organic dyes, J. Colloid Interface Sci. 490 (2017) 1–10.

[4] Z. Huang, Y. Zhao, Y. Song, J. Zhao, Synthesis of Co_3O_4 nanoclusters via an EDTANa4-assisted route for enhanced electrochemical application, J. Colloid Interface Sci. 500 (2017) 142–149.

[5] M.-T. Liu, L.-X. Chen, D.-N. Li, A.-J. Wang, Q.-L. Zhang, J.-J. Feng, One-pot controlled synthesis of AuPd@Pd core-shell nanocrystals with enhanced electrocatalytic performances for formic acid oxidation and glycerol oxidation, J. Colloid Interface Sci. 508 (2017) 551–558.

[6] Y. Xu, J. Sheng, X. Yin, J. Yu, B. Ding, Functional modification of breathable polyacrylonitrile/polyurethane/TiO_2 nanofibrous membranes with robust ultraviolet resistant and waterproof performance, J. Colloid Interface Sci. 508 (2017) 508–516.

[7] R. Jin, Y. Cui, Q. Wang, G. Li, Facile fabrication of CNTs@C@$MoSe_2$@Se hybrids with amorphous structure for high performance anode in lithium-ion batteries, J. Colloid Interface Sci. 508 (2017) 435–442.

[8] D. Santos, D.M. Silva, P.S. Gomes, M.H. Fernandes, J.D. Santos, V. Sencadas, Multifunctional PLLA-ceramic fiber membranes for bone regeneration applications, J. Colloid Interface Sci. 504 (2017) 101–110.

[9] S. Sirohi, R. Singh, N. Jain, B. Pani, K. Dutt, R. Nain, Synthesis and characterization of multifunctional ZnO/polyester green composite films, J. Polym. Res. 24 (2017) 193 (1-10).

[10] J.-Y. Chung, J.-G. Lee, Y.-K. Baek, P.-W. Shin, Y.-K. Kim, Magnetic field-induced enhancement of thermal conductivities in polymer composites by linear clustering of spherical particles, Compos. Part B: Eng. 136 (2018) 215–221.

[11] Y. Su, I. Zhitomirsky, Hybrid MnO_2/carbon nanotube-VN/carbon nanotube supercapacitors, J. Power Sources 267 (2014) 235–242.

[12] K. Rezwan, Q.Z. Chen, J.J. Blaker, A.R. Boccaccini, Biodegradable and bioactive porous polymer/inorganic composite scaffolds for bone tissue engineering, Biomaterials 27 (2006) 3413–3431.

[13] T. Wang, J.L. Keddie, Design and fabrication of colloidal polymer nanocomposites, Adv. Colloid Interface Sci. 147–148 (2009) 319–332.

[14] I. Zhitomirsky, L. Gal-Or, Formation of hollow fibers by electrophoretic deposition, Mater. Lett. 38 (1999) 10–17.

[15] O.O. Van der Biest, L.J. Vandeperre, Electrophoretic deposition of materials, Annu. Rev. Mater. Sci. 29 (1999) 327–352.

[16] X. Zhao, C. Hinchliffe, C. Johnston, P.J. Dobson, P.S. Grant, Spray deposition of polymer nanocomposite films for dielectric applications, Mater. Sci. Eng. B: Solid-State Mater. Adv. Technol. 151 (2008) 140–145.

[17] F. Mauvy, P. Lenormand, C. Lalanne, F. Ansart, J.M. Bassat, J.C. Grenier, Electrochemical characterization of YSZ thick films deposited by dip-coating process, J. Power Sources 171 (2007) 783–788.

[18] R. Chen, M.S. Ata, X. Zhao, A. Clifford, I. Puri, I. Zhitomirsky, Strategies for liquid-liquid extraction of oxide particles for applications in supercapacitor electrodes and thin films, J. Colloid Interface Sci. 499 (2017) 1–8.

[19] K.S. Mayya, F. Caruso, Phase transfer of surface-modified gold nanoparticles by hydrophobization with alkylamines, Langmuir 19 (2003) 6987–6993.

[20] M. Karg, N. Schelero, C. Oppel, M. Gradzielski, T. Hellweg, R. von Klitzing, Versatile phase transfer of gold nanoparticles from aqueous media to different organic media, Chem.-A Euro. J. 17 (2011) 4648–4654.

[21] A. Kumar, H. Joshi, R. Pasricha, A. Mandale, M. Sastry, Phase transfer of silver nanoparticles from aqueous to organic solutions using fatty amine molecules, J. Colloid Interface Sci. 264 (2003) 396–401.

[22] N. Gaponik, D.V. Talapin, A.L. Rogach, A. Eychmuller, H. Weller, Efficient phase transfer of luminescent thiol-capped nanocrystals: from water to nonpolar organic solvents, Nano Lett. 2 (2002) 803–806.

[23] J. Erler, S. Machunsky, P. Grimm, H.-J. Schmid, U.A. Peuker, Liquid-liquid phase transfer of magnetite nanoparticles-evaluation of surfactants, Powder Technol. 247 (2013) 265–269.

[24] B. Hu, Y. Nakahiro, T. Wakamatsu, The effect of organic solvents on the recovery of fine mineral particles by liquid-liquid extraction, Miner. Eng. 6 (1993) 731–742.

[25] W. Cheng, E. Wang, Size-dependent phase transfer of gold nanoparticles from water into toluene by tetraoctylammonium cations: a wholly electrostatic interaction, J. Phys. Chem. B 108 (2004) 24–26.

[26] H. Yao, O. Momozawa, T. Hamatani, K. Kimura, Phase transfer of gold nanoparticles across a water/oil interface by stoichiometric ion-pair formation on particle surfaces, Bull. Chem. Soc. Jpn. 73 (2000) 2675–2678.

[27] C. Wallar, T. Zhang, K. Shi, I. Zhitomirsky, Synthesis of metal and metal oxide nanoparticles, liquid-liquid extraction and application in supercapacitors, Colloids Surf. A: Physicochem. Eng. Aspects 500 (2016) 195–202.

[28] R. Poon, X. Zhao, M. Ata, A. Clifford, I. Zhitomirsky, Phase transfer of oxide particles for application in thin films and supercapacitors, Ceram. Int. 43 (2017) 8314–8320.

[29] A. Clifford, M. Ata, I. Zhitomirsky, Synthesis, liquid-liquid extraction and deposition of hydroxyapatite nanorod composites, Mater. Lett. 201 (2017) 140–143.

[30] R. Chen, R. Poon, R.P. Sahu, I.K. Puri, I. Zhitomirsky, MnO_2-carbon nanotube electrodes for supercapacitors with high active mass loadings, J. Electrochem. Soc. 164 (2017) A1673–A1678.

[31] R. Chen, M.S. Ata, X. Zhao, I. Puri, I. Zhitomirsky, Liquid-liquid extraction of oxide particles and application in supercapacitors, J. Mater. Res. 32 (2017) 1–9.

[32] T. Zhang, X. Zhao, R. Poon, A. Clifford, R. Mathews, I. Zhitomirsky, Synthesis and liquid-liquid extraction of non-agglomerated Al $(OH)_3$ particles for deposition of cellulose matrix composite films, J. Colloid Interface Sci. 508 (2017) 49–55.

[33] J.P. Folkers, C.B. Gorman, P.E. Laibinis, S. Buchholz, G.M. Whitesides, R.G. Nuzzo, Self-assembled monolayers of long-chain hydroxamic acids on the native oxide of metals, Langmuir 11 (1995) 813–824.

[34] C. Wallar, R. Poon, I. Zhitomirsky, High areal capacitance of V_2O_3-carbon nanotube electrodes, J. Electrochem. Soc. 164 (2017) A3620–A3627.

[35] J. Wang, H.-W. Cheng, H.-B. Zhao, W.-Q. Qin, G.-Z. Qiu, Flotation behavior and mechanism of rutile with nonyl hydroxamic acid, Rare Met. 35 (2016) 419–424.

[36] A. Sarvaramini, D. Azizi, F. Larachi, Hydroxamic acid interactions with solvated cerium hydroxides in the flotation of monazite and bastnasite-experiments and DFT study, Appl. Surf. Sci. 387 (2016) 986–995.

[37] J. Eisenlauer, E. Matijevic, Interactions of metal hydrous oxides with chelating agents. II. α-Fe_2O_3—low molecular and polymeric hydroxamic acid species, J. Colloid Interface Sci. 75 (1980) 199–211.

[38] R. Natarajan, D. Fuerstenau, Adsorption and flotation behavior of manganese dioxide in the presence of octyl hydroxamate, Int. J. Miner. Process. 11 (1983) 139–153.

[39] M. Giza, P. Thissen, G. Grundmeier, Adsorption kinetics of organophosphonic acids on plasma-modified oxide-covered aluminum surfaces, Langmuir 24 (2008) 8688–8694.

[40] E.S. Dzunuzovic, J.V. Dzunuzovic, A.D. Marinkovic, M.T. Marinovic-Cincovic, K. B. Jeremic, J.M. Nedeljkovic, Influence of surface modified TiO_2 nanoparticles by gallates on the properties of PMMA/TiO_2 nanocomposites, Eur. Polym. J. 48 (2012) 1385–1393.

[41] K. Shi, I. Zhitomirsky, Influence of current collector on capacitive behavior and cycling stability of Tiron doped polypyrrole electrodes, J. Power Sources 240 (2013) 42–49.

[42] M. Ata, J. Milne, I. Zhitomirsky, Fabrication of Mn_3O_4-carbon nanotube composites with high areal capacitance using cationic and anionic dispersants, J. Colloid Interface Sci. 512 (2018) 758–766.

[43] P. Suktha, N. Phattharasupakun, P. Dittanet, M. Sawangphruk, Charge storage mechanisms of electrospun Mn_3O_4 nanofibres for high-performance supercapacitors, RSC Adv. 7 (2017) 9958–9963.

[44] B.G.S. Raj, A.M. Asiri, J.J. Wu, S. Anandan, Synthesis of Mn_3O_4 nanoparticles via chemical precipitation approach for supercapacitor application, J. Alloys Compd. 636 (2015) 234–240.

[45] W. Dong, J.S. Sakamoto, B. Dunn, Electrochemical properties of vanadium oxide aerogels, Sci. Technol. Adv. Mater. 4 (2003) 3–11.

[46] W. Dong, D.R. Rolison, B. Dunn, Electrochemical properties of high surface area vanadium oxide aerogels, Electrochem. Solid-State Lett. 3 (2000) 457–459.

[47] Y.U. Jeong, A. Manthiram, Nanocrystalline manganese oxides for electrochemical capacitors with neutral electrolytes, J. Electrochem. Soc. 149 (2002) A1419–A1422.

[48] R.N. Reddy, R.G. Reddy, Sol-gel MnO_2 as an electrode material for electrochemical capacitors, J. Power Sources 124 (2003) 330–337.

[49] A.A. Yadav, Influence of electrode mass-loading on the properties of spray deposited Mn_3O_4 thin films for electrochemical supercapacitors, Thin Solid Films 608 (2016) 88–96.

[50] H. Cheng, H.M. Duong, D. Jewell, Three dimensional manganese oxide on carbon nanotube hydrogels for asymmetric supercapacitors, RSC Adv. 6 (2016) 36954–36960.

[51] X.-J. Li, Z.-W. Song, Y. Zhao, Y. Wang, X.-C. Zhao, M. Liang, W.-G. Chu, P. Jiang, Y. Liu, Vertically porous nickel thin film supported Mn_3O_4 for enhanced energy storage performance, J. Colloid Interface Sci. 483 (2016) 17–25.

[52] D. Dubal, D. Dhawale, R. Salunkhe, V. Fulari, C. Lokhande, Chemical synthesis and characterization of Mn_3O_4 thin films for supercapacitor application, J. Alloys Compd. 497 (2010) 166–170.

[53] A. Radhamani, R. Rao, Tunable supercapacitance of electrospun Mn_3O_4 beaded chains via charge-discharge cycling and control parameters, Appl. Surf. Sci. 403 (2017) 601–611.

[54] Y. Hu, C. Guan, G. Feng, Q. Ke, X. Huang, J. Wang, Flexible asymmetric supercapacitor based on structure-optimized Mn_3O_4/reduced graphene oxide nanohybrid paper with high energy and power density, Adv. Funct. Mater. 25 (2015) 7291–7299.

[55] Y. Qiao, Q. Sun, J. Xi, H. Cui, Y. Tang, X. Wang, A modified solvothermal synthesis of porous Mn_3O_4 for supercapacitor with excellent rate capability and long cycle life, J. Alloys Compd. 660 (2016) 416–422.

[56] M.P. Clark, W. Qu, D.G. Ivey, Nanostructured manganese oxide and manganese oxide/polyethylenedioxythiophene rods electrodeposited onto nickel foam for supercapacitor applications, J. Appl. Electrochem. 47 (2017) 39–49.

[57] X. Cui, F. Hu, W. Wei, W. Chen, Dense and long carbon nanotube arrays decorated with Mn_3O_4 nanoparticles for electrodes of electrochemical supercapacitors, Carbon 49 (2011) 1225–1234.

Chapter 7: Phase Transfer of Oxide Particles Using Hydroxamic Acid Derivatives and Application for Supercapacitors

Reprinted article with permission from J. Milne, R. M. E. Silva, Z. Z. Wang, and I. Zhitomirsky, "Phase transfer of oxide particles using hydroxamic acid derivatives and application for supercapacitors," *Ceram. Int.*, vol. 45, no. 2, pp. 2498–2503, 2018. DOI: 10.1016/j.ceramint.2018.10.177

Author's Contributions

- Synthesis of electrode materials
- Electrochemical testing of electrodes
- FTIR and XRD of materials
- Literature evaluation
- Preparation of manuscript draft

Ceramics International 45 (2019) 2498–2503

Contents lists available at ScienceDirect

Ceramics International

journal homepage: www.elsevier.com/locate/ceramint

Phase transfer of oxide particles using hydroxamic acid derivatives and application for supercapacitors

J. Milne, R.M.E. Silva, Z.Z. Wang, I. Zhitomirsky

Department of Materials Science and Engineering, McMaster University, Hamilton, Ontario, Canada L8S4L7

ARTICLE INFO

Keywords:
Supercapacitor
Cerium oxide
Zinc oxide
Iron hydroxide
Extraction
Dispersion

ABSTRACT

Particle extraction through liquid-liquid interface (PELLI) methods are developed for the colloidal processing of ZnO, CeO_2 and FeOOH particles. The direct transfer of the particles from an aqueous synthesis medium to a device processing medium allows for reduced nanoparticle agglomeration, because drying and re-dispersion processes are avoided. Different PELLI methods are developed, which are based on the use of chelating hydroxamates molecules, such as octanohydroxamic acid (OCHA) and bufexamac (BFXM) as extractors. OCHA and BFXM show strong adsorption on the ZnO, CeO_2 and FeOOH particles due to chelating bonding mechanisms and allow for efficient particle extraction from water to organic solvents. Bottom–up and top-down methods are used, depending on the density of the organic solvents. OCHA shows improved extraction of particles, compared to BFXM due to the difference in the chemical structure. The unique feature of hydroxamates is related to their pH-dependent solubility and their strong adsorption on particles at high pH, despite the electrostatic repulsion of the negatively charged particles and dissociated hydroxamic acids. It is found that OCHA can be used as a capping agent for particle synthesis and an extractor for their extraction to an organic phase. The advantages of PELLI methods are demonstrated by the fabrication and testing of FeOOH-carbon nanotube electrodes for supercapacitors, which show enhanced performance and high capacitance at high active mass loading. The enhanced electrochemical performance is achieved due to reduced particle agglomeration, which allows improved particle mixing with conductive carbon nanotubes. The capacitive properties are investigated at different charge-discharge rates. The impedance spectroscopy data shows dependence of capacitance on electrode potential and provides an insight into the strategies for further improvement of electrode performance.

1. Introduction

Liquid-liquid interface (LLI) phenomena have attracted significant attention for surface modification and colloidal processing of ceramic materials. LLI presents a unique environment for controlled synthesis of nanostructured oxides and hydroxides, such as MnO_2 [1], CuO [2,3], TiO_2 [4], ZnO [2,3], and Fe_2O_3 [2]. Moreover, LLI is a versatile platform for self-assembly of oxide nanoparticles [5] and formation of ordered 2-D structures. LLI allows easy access of organic surfactants to the nanoparticle surface and facilitates the formation of modified particles. Of particular interest are particle extraction through liquid-liquid interface (PELLI) methods, which are now being investigated for the direct transfer of particles synthesized in aqueous solutions to various organic solvents [1,6–9].

The development of PELLI has been motivated by the need to avoid the formation of hard agglomerates. It is in this regard that many processing technologies involve synthesis of particles in aqueous solutions of metal salts and then particle transfer to organic solvents for the fabrication of films and devices. A traditional approach involves drying of the synthesized particles and their re-dispersion in an organic solvent. However, particle drying usually causes agglomeration, which is governed by the reduction of surface energy and condensation of surface OH groups. In contrast, PELLI allows direct particle transfer from a synthesis medium to a device processing medium. The non-aqueous suspensions of transferred particles were used for the manufacturing of nanostructured composites [1,6,7]. From the previous studies it is evident that the dispersion of non-agglomerated particles in organic solvents facilitated their mixing with various water-insoluble additives and polymers for the fabrication of advanced thin film and bulk devices [1].

It was recognized that PELLI applications require the use of extractor molecules, which must be strongly adsorbed on particles [1,6,7]. The adsorption mechanisms are based on ion-pair [10], electrostatic [11] and covalent interactions [12]. The most promising results were obtained using chelating extractors, which created strong bi- or tri-dentate bonds [1,13]. Therefore, the general focus of PELLI

E-mail address: zhitom@mcmaster.ca (I. Zhitomirsky).

https://doi.org/10.1016/j.ceramint.2018.10.177
Received 20 September 2018; Received in revised form 18 October 2018; Accepted 19 October 2018

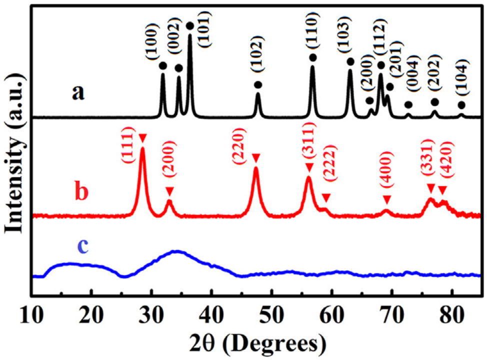

Fig. 1. X-ray diffraction patterns of (a) ZnO (• - JCPDS file 36–1451), (b) CeO_2 (▼ - JCPDS file 34–0394), (c) FeOOH.

development has been on the search for efficient chelating molecules and analysis of their adsorption on various materials.

Hydroxamic acids and their derivatives are promising molecules for the use as extractors for PELLI. Hydroxamates exhibited strong adsorption on rare earth oxides [14], titania [15,16], zirconia [17], ceria [18], copper [17] and iron oxides [19,20]. The unique adsorption properties of hydroxamates were used in the mineral flotation [14,21–23], where various hydroxamate molecules served as collectors. Hydroxamates adsorb chemically on inorganic surfaces, forming stable complexes with surface metal cations [24]. The strong interaction of hydroxamic acids with mineral particles allowed high flotation efficiency and selectivity [25]. Investigations revealed the influence of molecular structure of the hydroxamic acid derivatives on the flotation efficiency [26]. The comparison of different long chain (C18) hydroxamic acids as collectors showed that the flotation yield is dependent on the number of double bonds in the chemical structure of the collector molecules [26]. At low concentrations, the interactions of hydroxamic acids with different inorganic surfaces can result in vertically or horizontally oriented monolayers [27]. Density functional theory (DFT) simulations were performed to analyze the adsorption mechanisms [18]. DFT studies showed the influence of the molecular structure of hydroxamates on their adsorption on particles [28]. The minerals flotation literature examined hydroxamate behavior at water-air interface [29]. The application of hydroxamates for PELLI requires understanding of their behavior at the interface of immiscible fluids, such as water and organic solvents.

Hydroxamates are especially promising materials for PELLI applications, because they show strong adsorption on metal oxide surfaces at high pH [30–32] above the isoelectric points of various oxide materials, despite the electrostatic repulsion of the negatively charged particles and hydroxamic acids. Therefore, inorganic particles precipitated from aqueous solutions at high pH can potentially be extracted by PELLI using hydroxamate extractors. Recently, octanohydroxamic acid (OCHA) was used for extraction of manganese oxides [33]. These studies have generated interest in the application of OCHA for extraction of various functional oxide and hydroxide materials and investigation of other hydroxamate molecules for PELLI applications. It is important to note that adsorbed hydroxamates imparted advanced functional properties to ceramic particles and allowed the fabrication of materials with enhanced hydrophobicity and wear resistance [34], advanced photovoltaic and charge transfer properties [35–38].

The goal of this investigation was the synthesis and extraction of ZnO, CeO_2 and FeOOH using hydroxamate molecules, such as OCHA and bufexamac (BFXM). We analyzed the influence of the molecular structure of OCHA and BFXM on the particle extraction and proposed different extraction methods and mechanisms. Bottom-up (BU) and top-down (TD) strategies were used. The FeOOH material showed promising performance for the fabrication of FeOOH – multiwalled carbon nanotube (MCNT) supercapacitor (SCap) electrodes for operation in a negative potential window. The use of PELLI allowed good electrochemical performance at high active mass (AM).

2. Experimental procedures

OCHA and BFXM (TCI America), 1-butanol, dichloromethane, polyvinylbutyral, $Zn(NO_3)_2{\cdot}6H_2O$, $Ce(NO_3)_3{\cdot}6H_2O$, Na_2SO_4, NaOH, $FeCl_3{\cdot}6H_2O$ (Aldrich), MCNT (4 nm ID, 13 nm OD, 1–2 µm length, Bayer, Germany), and Ni foam current collectors (Vale Canada, 95% porosity) were used. ZnO and CeO_2 were prepared from $Zn(NO_3)_2$ and $Ce(NO_3)_3$ solutions, respectively, as it was described in the previous investigation [6]. The procedure for the fabrication of FeOOH was based on a chemical precipitation method [39] using 0.05 M $FeCl_3$ solutions. The pH of the solution was adjusted to pH = 7 by 0.01 M aqueous NaOH solution.

1-butanol and dichloromethane were used as particle-receiving organic liquids for the BU and TD PELLI methods, respectively. In the extraction method 1 (EMT1), the extractor molecules were dissolved in the organic liquids and added to the aqueous phase, containing as-precipitated ZnO, CeO_2 and FeOOH particles. After stirring, the particles were transferred to the organic solvents. In the extraction method 2 (EMT2), the extractor molecules were dissolved in aqueous NaOH solutions, which were added to the solutions of metal salts. In this method, the synthesis and particle modification were performed in one-step procedure, where the extractor molecules were used as capping agents for the synthesis. The addition of the organic solvent resulted in the particle transfer to the organic phase.

X-ray diffraction (XRD) studies were performed using a Nicolet I2 diffractometer and CuK$_\alpha$ radiation. FTIR studies of powder samples were carried out using a Bruker Vertex 70 spectrometer. The equipment and procedures for the investigation of capacitive properties were described in a previous investigation [6]. The active mass (AM) of

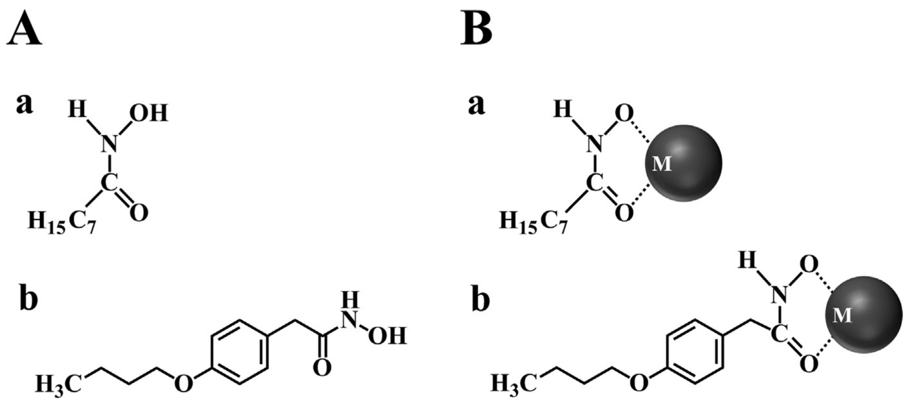

Fig. 2. (A) Structures of (a) OCHA and (b) BFXM and (B) adsorption of (a) OCHA and (b) BF on particles, involving chelation of surface metal atoms (M).

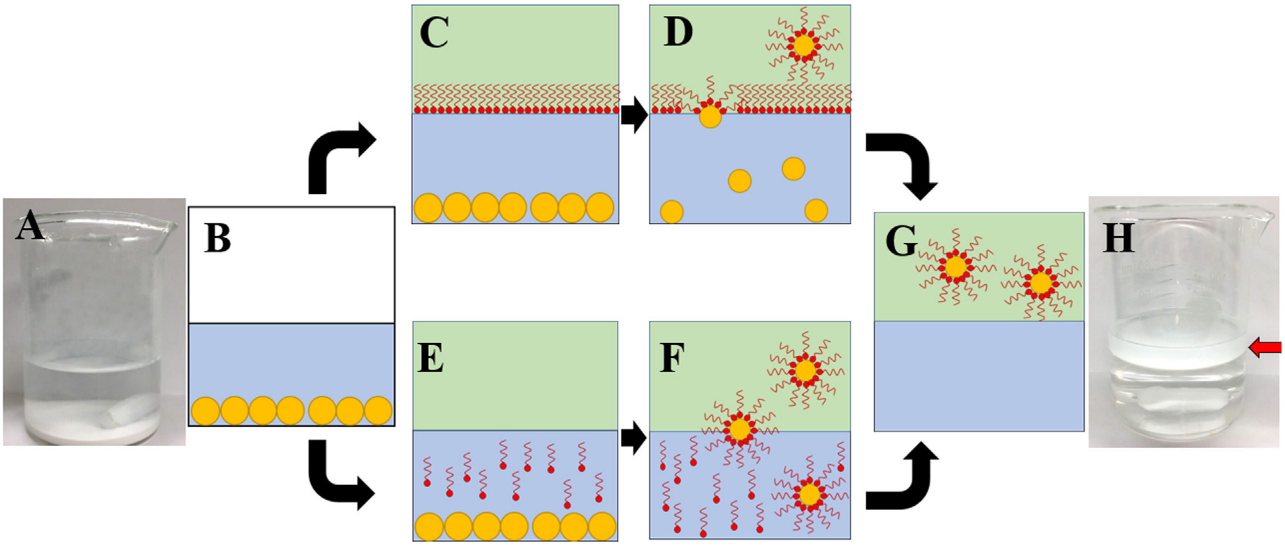

Fig. 3. (A) As-precipitated ZnO, (B-G) schematic of EMT1: (B-C-D-G) EMC 1 and (B-E-F-G) EMC 2, (H) extracted ZnO, arrow shows LLI.

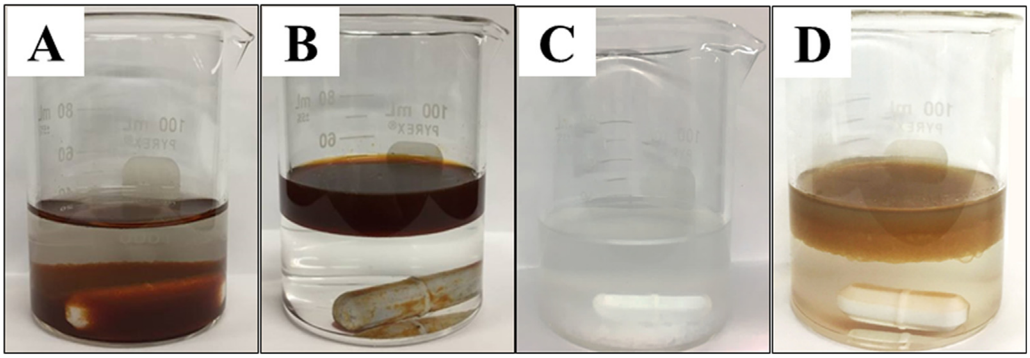

Fig. 4. (A) As-precipitated FeOOH and (B) FeOOH extracted by EMT1; (C) as-precipitated CeO_2 and (D) CeO_2 extracted by EMT1.

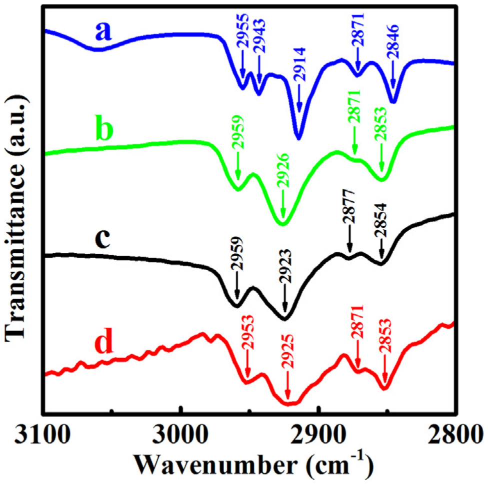

Fig. 5. FTIR spectra of (a) as-received OCHA, and materials extracted by EMT1 (b) ZnO, (c) CeO_2 and (d) FeOOH.

electrodes and electrode area were 39.6 mg cm^{-2} and 1 cm^2, respectively.

3. Results and discussion

X-ray diffraction studies revealed the formation of crystalline ZnO and CeO_2 phases, whereas FeOOH was amorphous (Fig. 1). OCHA and BFXM were used as extractors for PELLI. The chemical structures of OCHA and BFXM include a carbonyl group and NOH_2 group (Fig. 2A(a,b)). The structure of OCHA contains a hydrophobic alkyl group, whereas the structure of BFXM contains an aromatic group and a shorter alkyl group. The mechanism of hydroxamates adsorption on materials has been described in the literature [15]. It is based on the chelation chemistry and involves carbonyl and NOH_2 groups. Fig. 2B (a,b) shows adsorption of OCHA and BFXM on metal oxide particles.

ZnO, CeO_2 and FeOOH were extracted by EMT1 using OCHA and BFXM. Fig. 3 shows extraction of ZnO by EMT1 using OCHA. The suspensions of as-prepared ZnO were unstable (Fig. 3A,B) and showed fast particle precipitation immediately after stirring. The extraction can be based on two different mechanisms or a combination of both. It should be noted that similar to other head-tail surfactants, the OCHA and BFXM molecules can be accumulated at the liquid-liquid interface. In the extraction mechanism1 (EMC1), the extractor molecules were accumulated at the LLI (Fig. 3C) and adsorbed on the particles (Fig. 3D), which were then extracted to the organic phase (Fig. 3G,H). In the extraction mechanism 2 (EMC2), the extractor molecules penetrated the LLI (Fig. 3E), adsorbed on the particles in the aqueous phase (Fig. 3F) and then extracted to the organic phase (Fig. 3G,H). Fig. 4 shows that CeO_2 and FeOOH can also be extracted by EMT1 using OCHA. EMT1 has also been utilized for the extraction of ZnO, CeO_2 and FeOOH using BFXM (Supplementary information, Fig. S1). However, OCHA showed higher extraction efficiency, which was close to 100%. It is important to note that the OCHA and BFXM molecules exhibit a pH-dependent solubility. The solubility of such molecules increases with increasing pH. The synthesis of ZnO, CeO_2 and FeOOH was performed

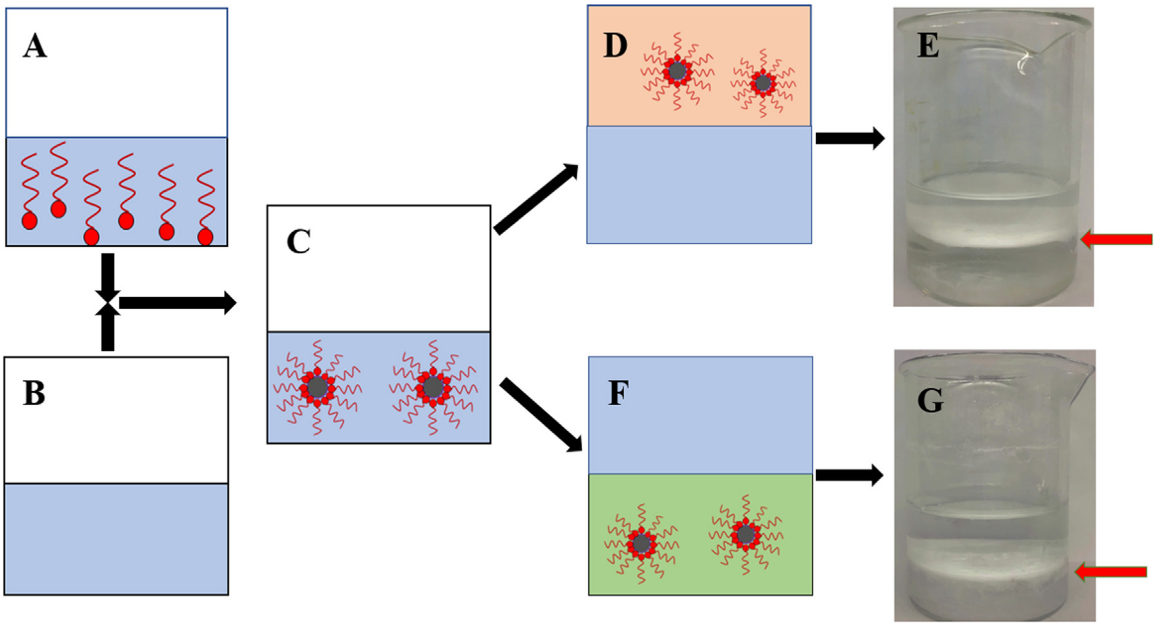

Fig. 6. (A-G) Extraction of ZnO by EMT2: (A-C) schematic of synthesis in aqueous phase by addition of (A) OCHA solution in alkali to (B) aqueous solution of Zn $(NO_3)_2$, (C) formation of ZnO particles, containing adsorbed OCHA, (C,D) schematic of down-up extraction and (E) image of extracted ZnO, arrow shows LLI (C, F) schematic of top-down extraction and (G) image of extracted ZnO, arrow shows LLI.

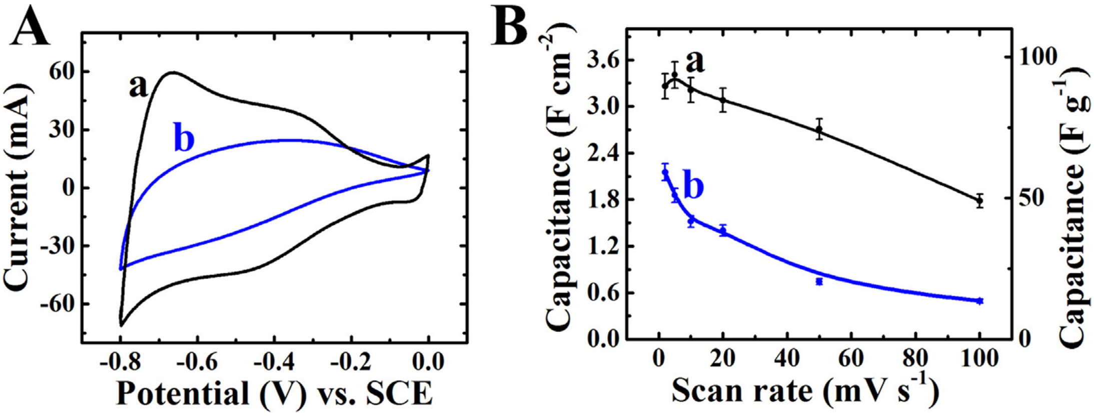

Fig. 7. (A) CV at 10 mV s^{-1} and (B) capacitance for FeOOH- MCNT electrodes with AM of 39.6 mg cm^{-2} prepared (a) using PELLI and (b) by traditional drying and re-dispersion method.

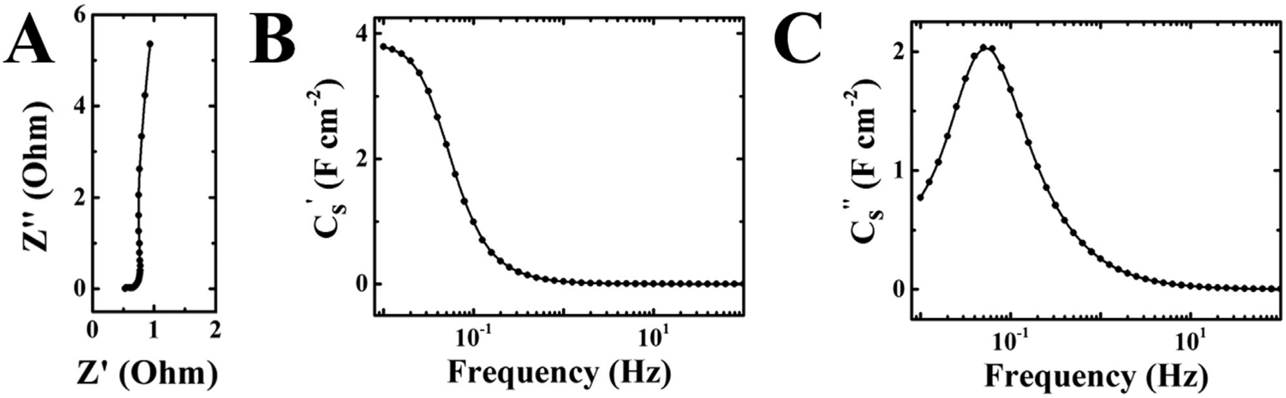

Fig. 8. (A) Nyquist and (B, C) Bode diagrams of (A) impedance and (B, C) components of complex capacitance for FeOOH- MCNT electrode with AM of 39.6 mg cm^{-2} at open circuit conditions.

at pH 10, 11 and 7, respectively. Therefore, the extraction of ZnO, CeO_2 and FeOOH in EMT1 involved different contributions of EMC1 and EMC2. It is important to note that CeO_2 was extracted at relatively high pH (pH = 11) which was far above the isoelectric point of CeO_2 (pH = 6) [40] despite the electrostatic repulsion of negatively charged hydroxamic acids and CeO_2 particles. This observation indicates strong

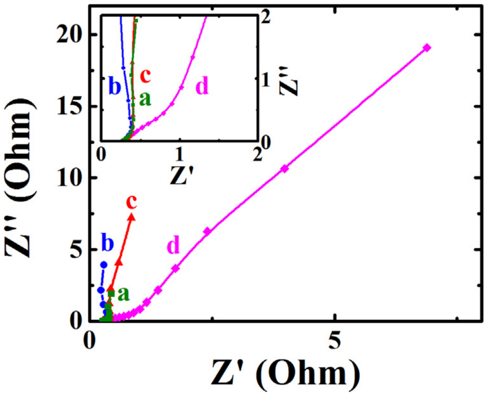

Fig. 9. Nyquist diagrams for FeOOH-MCNT electrode with AM of 39.6 $\mathrm{mg\,cm^{-2}}$ at electrode potentials of (a) -0.8, (b) -0.5, (c) -0.2 and (d) 0.0 V versus SCE, inset shows high frequency range.

adsorption of the hydroxamic acids on the particles, which results from the chelating properties of the molecules.

The adsorption of the extractor molecules was confirmed by the FTIR analysis of the extracted particles. The spectra of OCHA (Fig. 5) and BFXM (Supplementary information, Fig. S2) showed absorptions in the range of 2800–3000 $\mathrm{cm^{-1}}$, which resulted from vibrations of CH_3 and CH_2 groups [33]. The particles of ZnO, CeO_2 and FeOOH, extracted using OCHA (Fig. 5) and BFXM (Supplementary information, Fig. S2) showed similar absorptions, which confirmed OCHA and BFXM adsorption.

The solubility of OCHA and BFXM in alkali allowed PELLI using EMT2. Fig. 6 shows different steps in the EMT2, which is based on dissolution of OCHA in alkali and precipitation of ZnO in the presence of OCHA. In this approach OCHA served as a capping agent for the synthesis and phase transfer agent in the extraction. Fig. 6 indicates that BU and TD strategies can be used, depending on the solvent density.

The FeOOH particles, extracted by EMT1, were used for the fabrication of supercapacitor electrodes. For comparison, the electrodes of similar composition and mass were prepared by the traditional strategy, which involved drying of the precipitated FeOOH particles and their redispersion in an organic phase, containing dissolved binder and MCNT. It should be noted that the dissolution of a water insoluble polymer binder in an organic solvent is critical for the fabrication of composites for aqueous SCap electrodes with reduced binder content. We found that drying of the FeOOH particles resulted in the formation of hard agglomerates, which was attributed to the condensation of OH groups on the particle surface and formation of oxo-bridges. Another driving force for particle agglomeration is the reduction of surface area and surface energy. The mixing of agglomerated particles with MCNT presented difficulties. However, good dispersion of FeOOH and their mixing with MCNT is important for the fabrication of electrodes with high capacitance and low resistance. In the PELLI method, the particles were transferred directly from the aqueous phase to the organic phase and the drying stage was avoided.

Fig. 7A shows cyclic voltammetry data for the FeOOH-MCNT (20% MCNT) composites. The integral capacitance was calculated in the window of 0.0–0.8 V versus saturated calomel electrode (Fig. 7B). Testing results showed that a significant improvement of the capacitive behavior can be achieved using PELLI. The composite electrodes prepared using PELLI showed the highest areal capacitance of 3.3 $\mathrm{F\,cm^{-2}}$ at low scan rates. The electrodes showed good capacitance retention at high scan rate, which was about 50% at a scan rate of 100 $\mathrm{mV\,s^{-1}}$. In, contrast, the electrodes, prepared by traditional drying and re-dispersion method showed significantly lower CV area and lower capacitance, especially at high scan rates (Fig. 7).

The capacitive behavior of the electrodes has also been tested using impedance spectroscopy. Such measurements are usually performed at open circuit potential conditions at low AC voltages [41–43]. The analysis of the Nyquist plot (Fig. 8A) showed low resistance, which is beneficial for SCap applications. The slop in the plot was close to 90° and indicated capacitive behavior. The real and imaginary parts of the complex AC capacitance (Fig. 8B,C) showed a relaxation type dispersion, which resulted in the reduction of the real part of capacitance (C_S') with increasing frequency and a relaxation maximum in the imaginary part (C_S''). Turning again to the CV data (Fig. 7A(a)), it should be noted that differential AC capacitance is dependent on the electrode potential, because the CV shape deviates significantly from the ideal box shape. Therefore, impedance measurements have also been performed at different electrode potentials. The electrodes tested at applied potentials of -0.8 to 0.2 V versus SCE showed relatively low resistance $R = Z'$, however significantly higher resistance was obtained at 0.0 V versus SCE (Fig. 9). The differential AC capacitance C_S', measured at low frequencies decreased with increasing electrode potential (Fig. 10A) from -0.8 to 0.0 V versus SCE. The frequency dependences of the components of complex capacitance showed relaxation type dispersions. The relaxation frequency, corresponding to maximum in C_S'' increased with increasing electrode potential in the range of -0.8 to 0.2 V versus SCE (Fig. 10B). Testing results indicated that behavior of the electrodes must be improved in the potential range of -0.2 to 0.0 V versus SCE. This problem can potentially be addressed by the development of composites. The application of PELLI for different materials can be used for their co-extraction and improved mixing.

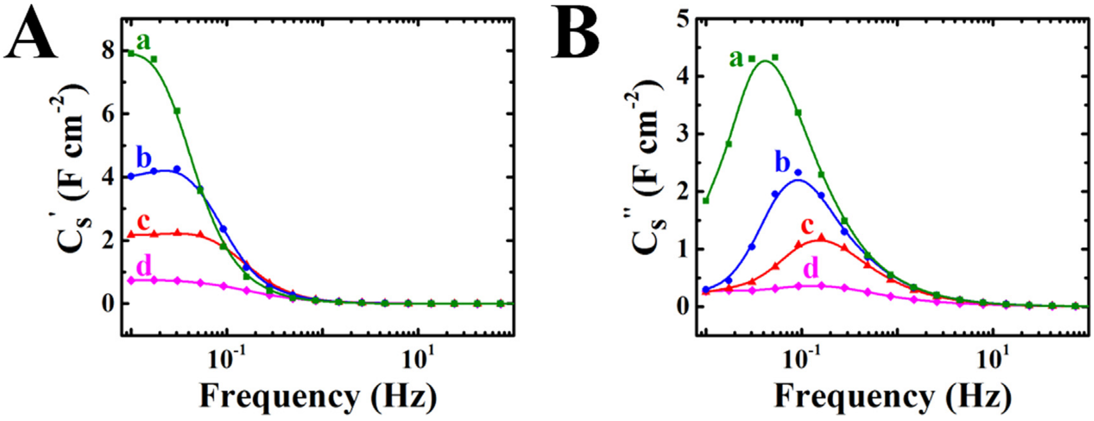

Fig. 10. Bode diagrams of complex capacitance for FeOOH-MCNT electrode with AM of 39.6 $\mathrm{mg\,cm^{-2}}$ at electrode potentials of (a) -0.8, (b) -0.5, (c) -0.2 and (d) 0.0 V versus SCE.

4. Conclusions

OCHA and BFXM allowed extraction of ZnO, CeO_2 and FeOOH particles from water to organic solvents. OCHA showed enhanced extraction efficiency, compared to BFXM, due to the difference in their chemical structure. EMT1 and EMT2 were developed, which are based on different mechanisms. PELLI methods allowed for BU and TD extractions. The use of hydroxamates allowed for efficient extraction from aqueous suspensions at high pH, despite of electrostatic repulsion of the negatively charged dissociated hydroxamate molecules and negatively charged particles. It was found that OCHA can be used as a capping agent for particle synthesis and as an extractor for their extraction from water to an organic phase. The advantages of PELLI have been demonstrated by the comparison of the electrochemical performance of FeOOH-MCNT electrodes, prepared using PELLI and by a traditional drying and re-dispersion method. The electrodes, prepared using PELLI showed improved capacitive behavior due to reduced FeOOH agglomeration, which facilitated FeOOH mixing with conductive MCNT. The FeOOH-MCNT composites showed promising performance for application in negative electrodes of SCap. The CV data, coupled with impedance analysis at different electrode potentials showed that electrochemical performance must be improved in the potential range of -0.2 to 0.0 V versus SCE. PELLI is a promising method for the fabrication of composites with improved performance.

Acknowledgements

The authors gratefully acknowledge the Natural Sciences and Engineering Research Council of Canada for the financial support.

Appendix A. Supporting information

Supplementary data associated with this article can be found in the online version at doi:10.1016/j.ceramint.2018.10.177.

References

[1] C. Wallar, T. Zhang, K. Shi, I. Zhitomirsky, Synthesis of metal and metal oxide nanoparticles, liquid–liquid extraction and application in supercapacitors, Colloids Surf. A: Physicochem. Eng. Asp. 500 (2016) 195–202.

[2] C. Rao, S. Vivekchand, K. Biswas, A. Govindaraj, Synthesis of inorganic nanomaterials, Dalton Trans. (2007) 3728–3749.

[3] C. Rao, K. Kalyanikutty, The liquid–liquid interface as a medium to generate nanocrystalline films of inorganic materials, Acc. Chem. Res. 41 (2008) 489–499.

[4] T. Narabe, M. Hagiwara, S. Fujihara, A biphasic sol–gel route to synthesize anatase TiO_2 particles under controlled conditions and their DSSC application, J. Asian Ceram. Soc. 5 (2017) 427–435.

[5] A. Toor, T. Feng, T.P. Russell, Self-assembly of nanomaterials at fluid interfaces, Eur. Phys. J. E 39 (2016) 57.

[6] R. Chen, Z.Z. Wang, R.P. Sahu, I.K. Puri, I. Zhitomirsky, Influence of molecular structure of extractor molecules on liquid-liquid extraction of oxide particles and properties of composites, Ceram. Int. 44 (2018) 15714–15720.

[7] R. Poon, X. Zhao, M. Ata, A. Clifford, I. Zhitomirsky, Phase transfer of oxide particles for application in thin films and supercapacitors, Ceram. Int. 43 (2017) 8314–8320.

[8] J. Erler, S. Machunsky, P. Grimm, H.-J. Schmid, U.A. Peuker, Liquid–liquid phase transfer of magnetite nanoparticles—evaluation of surfactants, Powder Technol. 247 (2013) 265–269.

[9] R. Bhandary, J. Alauzun, P. Hesemann, A. Stocco, M. In, P.H. Mutin, Phase transfer of TiO_2 nanoparticles from water to ionic liquid triggered by phosphonic acid grafting, Soft Matter 13 (2017) 8023–8026.

[10] H. Yao, O. Momozawa, T. Hamatani, K. Kimura, Phase transfer of gold nanoparticles across a water/oil interface by stoichiometric ion-pair formation on particle surfaces, Bull. Chem. Soc. Jpn. 73 (2000) 2675–2678.

[11] W. Cheng, E. Wang, Size-dependent phase transfer of gold nanoparticles from water into toluene by tetraoctylammonium cations: a wholly electrostatic interaction, J. Phys. Chem. B. 108 (2004) 24–26.

[12] M. Karg, N. Schelero, C. Oppel, M. Gradzielski, T. Hellweg, R. von Klitzing, Versatile phase transfer of gold nanoparticles from aqueous media to different organic media, Chem.-A Eur. J. 17 (2011) 4648–4654.

[13] R. Chen, R. Poon, R.P. Sahu, I.K. Puri, I. Zhitomirsky, MnO_2-carbon nanotube electrodes for supercapacitors with high active mass loadings, J. Electrochem. Soc. 164 (2017) A1673–A1678.

[14] J. Cui, G.A. Hope, A.N. Buckley, Spectroscopic investigation of the interaction of hydroxamate with bastnaesite (cerium) and rare earth oxides, Miner. Eng. 36 (2012) 91–99.

[15] J. Wang, H.-W. Cheng, H.-B. Zhao, W.-Q. Qin, G.-Z. Qiu, Flotation behavior and mechanism of rutile with nonyl hydroxamic acid, Rare Met. 35 (2016) 419–424.

[16] B. Rudshteyn, C.F. Negre, R.S. Oliboni, A. Monti, J. Chen, R.H. Crabtree, L.G. Rego, V.S. Batista, Inferring Protonation States of Hydroxamate Adsorbates on TiO_2 Surfaces, J. Phys. Chem. C 121 (2017) 11985–11990.

[17] J.P. Folkers, C.B. Gorman, P.E. Laibinis, S. Buchholz, G.M. Whitesides, R.G. Nuzzo, Self-assembled monolayers of long-chain hydroxamic acids on the native oxide of metals, Langmuir 11 (1995) 813–824.

[18] A. Sarvaramini, D. Azizi, F. Larachi, Hydroxamic acid interactions with solvated cerium hydroxides in the flotation of monazite and bastnäsite—experiments and DFT study, Appl. Surf. Sci. 387 (2016) 986–995.

[19] A.N. Buckley, G.K. Parker, Adsorption of n-octanohydroxamate collector on iron oxides, Int. J. Mineral. Process. 121 (2013) 70–89.

[20] J. Eisenlauer, E. Matijević, Interactions of metal hydrous oxides with chelating agents. II. α-Fe2O3—low molecular and polymeric hydroxamic acid species, J. Colloid Interface Sci. 75 (1980) 199–211, https://doi.org/10.1016/0021-9797(80)90362-8.

[21] Y. Gao, Z. Gao, W. Sun, Y. Hu, Selective flotation of scheelite from calcite: a novel reagent scheme, Int. J. Mineral. Process. 154 (2016) 10–15.

[22] X. Zhang, H. Du, X. Wang, J. Miller, Surface chemistry aspects of bastnaesite flotation with octyl hydroxamate, Int. J. Mineral. Process. 133 (2014) 29–38.

[23] C. Marion, A. Jordens, R. Li, M. Rudolph, K.E. Waters, An evaluation of hydroxamate collectors for malachite flotation, Sep. Purif. Technol. 183 (2017) 258–269.

[24] G.B. Abaka-Wood, J. Addai-Mensah, W. Skinner, A study of flotation characteristics of monazite, hematite, and quartz using anionic collectors, Int. J. Mineral. Process. 158 (2017) 55–62.

[25] F. Zhou, T. Chen, C. Yan, H. Liang, T. Chen, D. Li, Q. Wang, The flotation of low-grade manganese ore using a novel linoleate hydroxamic acid, Colloids Surf. A: Physicochem. Eng. Asp. 466 (2015) 1–9.

[26] F. Zhou, C. Yan, H. Wang, Q. Sun, Q. Wang, A. Alshameri, Flotation behavior of four C18 hydroxamic acids as collectors of rhodochrosite, Miner. Eng. 78 (2015) 15–20.

[27] X. Ni, Q. Liu, The adsorption and configuration of octyl hydroxamic acid on pyrochlore and calcite, Colloids and Surfaces A: physicochemical and Engineering Aspects, 411 (2012) 80–86.

[28] G. Zhao, H. Zhong, X. Qiu, S. Wang, Y. Gao, Z. Dai, J. Huang, G. Liu, The DFT study of cyclohexyl hydroxamic acid as a collector in scheelite flotation, Miner. Eng. 49 (2013) 54–60.

[29] A.N. Buckley, J.A. Denman, G.A. Hope, The adsorption of n-octanohydroxamate collector on Cu and Fe oxide minerals investigated by static secondary ion mass spectrometry, Minerals 2 (2012) 493–515.

[30] G. Hope, A. Buckley, G. Parker, A. Numprasanthai, R. Woods, J. McLean, The interaction of n-octanohydroxamate with chrysocolla and oxide copper surfaces, Miner. Eng. 36 (2012) 2–11.

[31] Q. Meng, Q. Feng, Q. Shi, L. Ou, Studies on interaction mechanism of fine wolframite with octyl hydroxamic acid, Miner. Eng. 79 (2015) 133–138.

[32] G.K. Parker, A.N. Buckley, R. Woods, G.A. Hope, The interaction of the flotation reagent, n-octanohydroxamate, with sulfide minerals, Miner. Eng. 36 (2012) 81–90.

[33] J. Milne, I. Zhitomirsky, Application of octanohydroxamic acid for liquid-liquid extraction of manganese oxides and fabrication of supercapacitor electrodes, J. Colloid Interface Sci. 515 (2018) 50–57.

[34] M. Hemgesberg, S. Schütz, C. Müller, M. Schlörholz, H. Latzel, Y. Sun, C. Ziegler, W.R. Thiel, Ultra-fast photo-patterning of hydroxamic acid layers adsorbed on TiAlN: the challenge of modeling thermally induced desorption, Appl. Surf. Sci. 259 (2012) 406–415.

[35] W. Li, L.G. Rego, F.-Q. Bai, J. Wang, R. Jia, L.-M. Xie, H.-X. Zhang, What makes hydroxamate a promising anchoring group in dye-sensitized solar cells? Insights from theoretical investigation, J. Phys. Chem. Lett. 5 (2014) 3992–3999.

[36] W. Li, L.G. Rego, F.-Q. Bai, C.-P. Kong, H.-X. Zhang, Theoretical investigation of the adsorption, IR, and electron injection of hydroxamate anchor at the TiO_2 anatase (1 0 1) surface, RSC Adv. 4 (2014) 19690–19693.

[37] T.P. Brewster, S.J. Konezny, S.W. Sheehan, L.A. Martini, C.A. Schmuttenmaer, V.S. Batista, R.H. Crabtree, Hydroxamate anchors for improved photoconversion in dye-sensitized solar cells, Inorg. Chem. 52 (2013) 6752–6764.

[38] B.J. Brennan, J. Chen, B. Rudshteyn, S. Chaudhuri, B.Q. Mercado, V.S. Batista, R.H. Crabtree, G.W. Brudvig, Molecular titanium–hydroxamate complexes as models for TiO_2 surface binding, Chem. Commun. 52 (2016) 2972–2975.

[39] G.N. Subbanna, C. Sudakar, T.R.N. Kutty, Precipitation of acicular hydrogoethite (-FeOOH 0.1 x 0.22) using morphology controlling cationic additives, Mater. Chem. Phys. 78 (2003) 43–50.

[40] M. Kosmulski, pH-dependent surface charging and points of zero charge: III. Update, J. Colloid Interface Sci. 298 (2006) 730–741.

[41] R.B. Pujari, A.C. Lokhande, T.T. Ghogare, S.B. Kale, C.D. Lokhande, Hydrothermally synthesized monoclinic Yb_2S_3 thin films for supercapacitive application, J. Mater. Sci.: Mater. Electron. 29 (2018) 14116–14121.

[42] P.M. Kharade, J.V. Thombare, A.R. Babar, R.N. Bulakhe, S.B. Kulkarni, D.J. Salunkhe, Electrodeposited nanoflakes like hydrophilic Co3O4 as a supercapacitor electrode, J. Phys. Chem. Solids 120 (2018) 207–210.

[43] K. Shi, I. Zhitomirsky, Polypyrrole nanofiber–carbon nanotube electrodes for supercapacitors with high mass loading obtained using an organic dye as a co-dispersant, J. Mater. Chem. A 1 (2013) 11614–11622.

Chapter 8: Development of a Cyclically Stable FeOOH Negative Electrode Using Zn as a Dopant

8.1 Introduction

In order to further increase power and energy density, lower fabrication costs, and use environmentally benign materials, advanced electrode materials must be developed or the device operating voltage must be increased. Nano-sized materials and/or materials with nanostructures have been extensively researched as these materials can provide more active surface area for double-layer capacitance or pseudocapacitance[102]–[104]. Organic electrolytes can be utilized to increase the operating voltage due to their stability at higher voltages. However, organic electrolytes suffer from safety hazards as well as high fabrication costs due to the water-free assembly environment that is required. This has led many researchers to focus on positive and negative electrode materials that have large oxygen and hydrogen evolution overpotentials in aqueous electrolytes. Ideally, this asymmetric electrode configuration can increase the overall operating voltage well beyond the thermodynamic breakdown voltage of water, with some devices reported operating up to 2 V[105].

Currently, the typical asymmetric supercapacitor configuration consists of a pseudocapacitive positive electrode paired with an EDLC negative electrode. Examples of such devices in research are: MnO_2/AC system with a voltage window of 0–2.2 V[106], a double-layer hydroxide of CoAl/AC device with an operating voltage of 0.9–1.6 V[107], and a RuO_2/AC device with a voltage range of 0–1.4 V[108]. Activated carbon is commercially used in EDLC supercapacitors as well as for the negative electrode in asymmetric supercapacitors as discussed previously. Activated carbon provides great power density but lacks in energy density due to the EDLC nature of the material, hindering the overall device performance. Therefore, it is of critical importance to develop pseudocapacitive materials with enhanced capacitive properties instead of relying on activated carbon systems. Unfortunately, the implementation of metal oxides as negative electrode materials for asymmetric supercapacitors is seldomly reported[4].

A material of interest for high performance negative electrodes is FeOOH. FeOOH has shown impressive electrochemical properties and cyclic stability in highly basic electrolytes such as 1M KOH[109]. Despite the desirable performance characteristics reported in KOH, using such an electrolyte can be a safety concern as well as limiting to positive electrode selection as materials such as MnO_2[31]. However, when tested in a neutral aqueous electrolyte, Li_2SO_4, FeOOH displayed poor cyclic stability as capacitance retention was less than 55% after just 100 cycles[110]. It should be known that a retention of less than 80% is considered device failure in a commercial context. It was reported that the poor cyclic stability in neutral aqueous electrolytes was a product of electrode material dissolution[110]. This chapter focuses on the performance of FeOOH-based negative supercapacitor electrodes in neutral aqueous electrolytes and the development of a novel solution to the cyclic stability problem. The goal of the investigation was to improve the stability of FeOOH in neutral electrolyte while maintaining high capacitance and low ESR.

8.2 Results and Discussion

A baseline FeOOH-MWCNT negative electrode with a mass loading of 40 mg was fabricated using a facile synthesis method. FeOOH was precipitated from $FeCl_3$ dissolved in deionized (DI) water using 4M NaOH. The FeOOH particles were rinsed with DI water then mixed with dispersed MWCNT. Figure 8-1A shows CVs for FeOOH-MWCNT at different scan rates. The shapes of the curves are close to the ideal box shape, indicating good pseudocapacitive behaviour. An impressive capacitance of 4.5 F cm^{-2} was achieved at 2 mV s^{-1} (Figure 8-1B). The capacitance decreased with increasing scan rate as a result of diffusion limitations of electrolyte into the electrode.

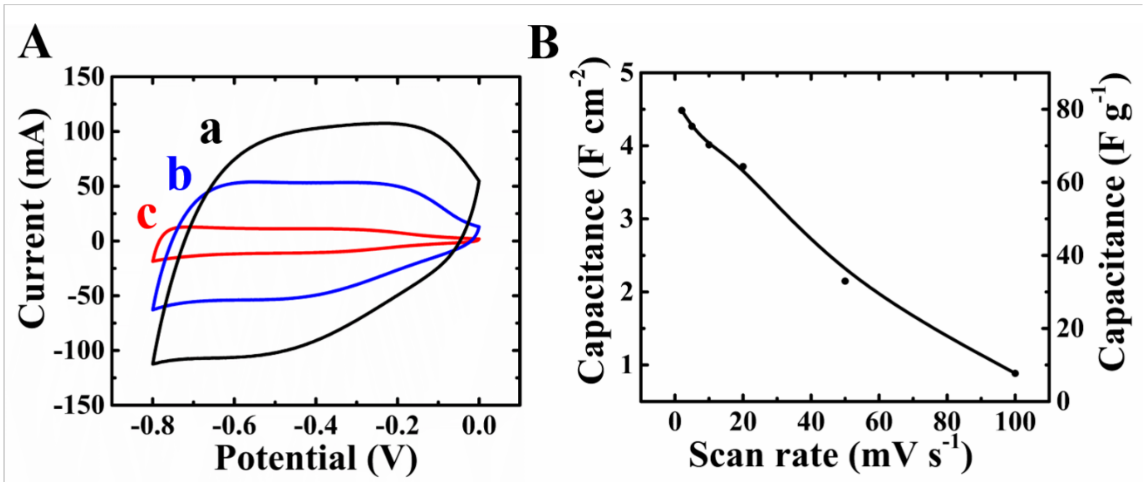

Figure 8-1: (A) CVs at scan rates of (a) 2, (b) 10, and (c) 20 mV s^{-1}, (B) Cs and Cm, calculated from the CV data for FeOOH-MWCNT composites.

Figure 8-2A is a Nyquist plot that shows relatively low electrode resistance, Z′. The slope of the Nyquist plot was almost 90°, again displaying good capacitive behavior. The examination of the complex capacitance (Figure 8-2B,C), derived from the EIS data showed a relaxation type dispersion by the decrease of the real capacitance (C′) with frequency and corresponding maximum in the frequency dependence of the imaginary part of capacitance, C″. The real part of the complex capacitance, calculated from the impedance data at low frequencies (Figure 8-28B) was agreeable with capacitance that was calculated from the CV data at low scan rates (Figure 8-1B).

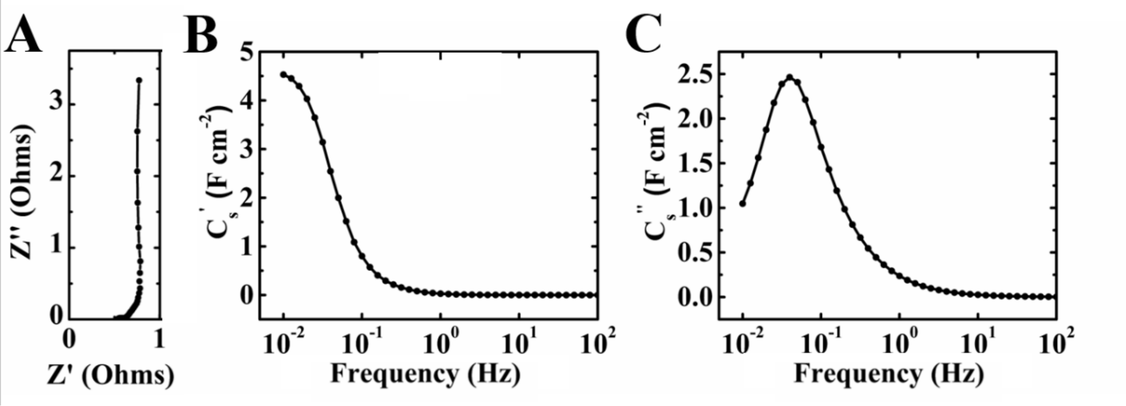

Figure 8-2: (A) Nyquist plot of complex impedance and frequency dependences of (B) C'_s and (C) C''_s calculated from the impedance data for FeOOH-MWCNT composites.

Figure 8-3 shows the cyclic stability of the electrode by plotting the capacitance retention over 1000 CV cycles at a scan rate of 50 mV s^{-1}. The first 200 cycles show activation type behavior which can be attributed to minor transformations in the microstructure giving rise to slight changes in capacitance. However, after 200 cycles a significant decrease in capacitance occurs. By 1000 cycles the capacitance retention is 64%.

It has been reported in literature that the poor cyclic stability is a result of Fe^{2+} dissolution into the electrolyte[110]. It has been shown[111] that after cycling FeOOH in 2.5M Li_2SO_4 ions of Fe^{2+} can be found in the electrolyte. The same issue is likely happening in this instigation as the Fe^{2+}/Fe^{3+} redox reaction takes place, dissolution of Fe^{2+} occurs hindering the cyclic stability.

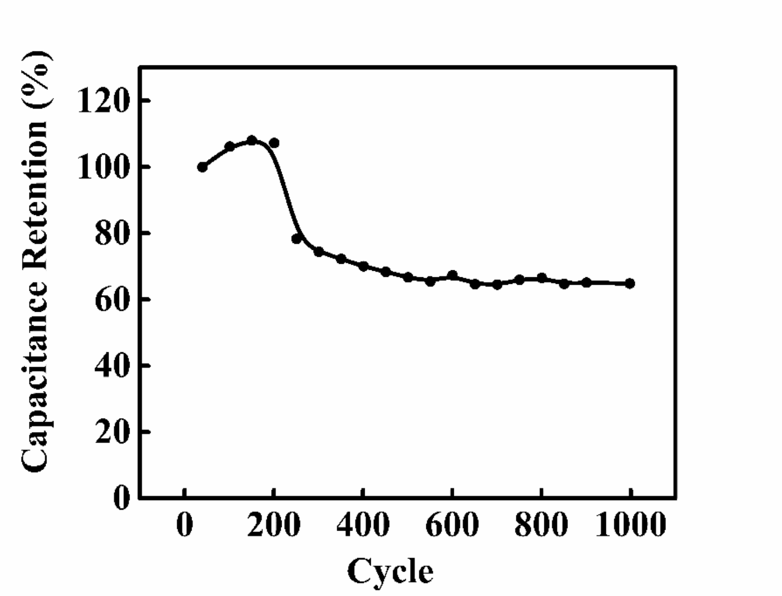

Figure 8-3: Capacitance retention over 1000 CV cycles at 50 mV s^{-1} for the FeOOH-MWCNT electrode.

It is known that the introduction of foreign metal ions during synthesis can change the structural and electrochemical properties of metal oxides[26]. A Zn doped FeOOH electrode was fabricated with a very similar method as the previous electrode except $ZnCl_2$ was present during synthesis with the aim to improve the cyclic stability of the electrode. The electrode was doped with 12 at% of Zn. Figure 8-3A,B shows very similar electrochemical performance and capacitance of the Zn/FeOOH-MWCNT electrode compared to the FeOOH-MWCNT electrode. Similar CV shapes indicate that the addition of the Zn^{2+} ions during synthesis does not have a significant impact on the redox capability of the FeOOH material. Both Zn/FeOOH-MWCNT and FeOOH-MWCNT electrodes show similar capacitance values at all scan rates justifying that the doping has no major effects on the capacitance.

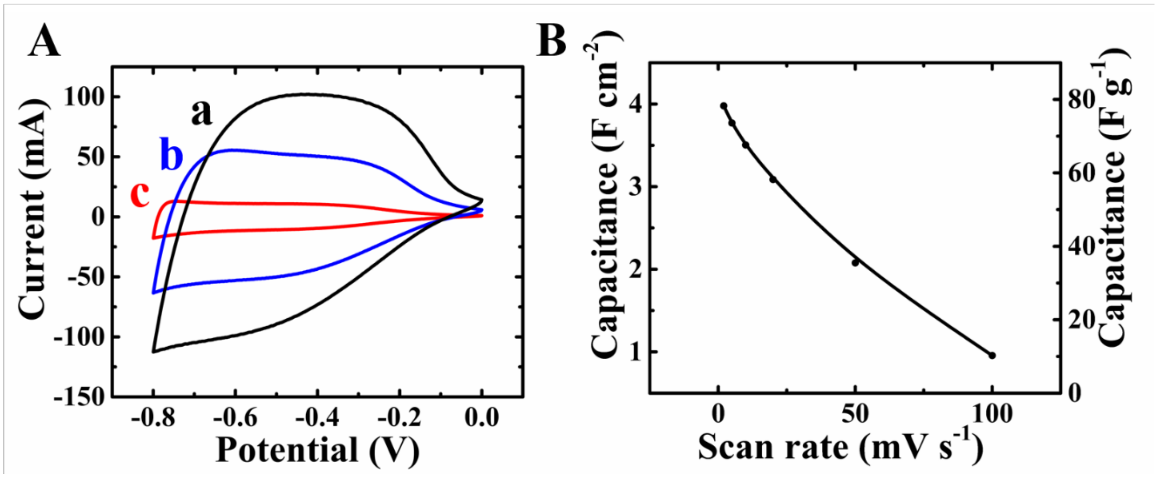

Figure 8-4: (A) CVs at scan rates of (a) 2, (b) 10, and (c) 20 mV s^{-1}, (B) Cs and Cm, calculated from the CV data for Zn/FeOOH-MWCNT composites.

Figure 8-4A is a Nyquist plot derived from EIS data. It shows very low internal resistance and is almost identical to that of the non-doped FeOOH-MWCNT electrode. The complex capacitance data (Figure 8-4B,C) shows values that correspond to that of the CV data with capacitance and a maximum at a similar frequency to that of the FeOOH-MWCNT. The strong agreement between the EIS data of the two electrodes verifies that the doping of Zn has no significant effects on the resistance of the electrode or impact on capacitance.

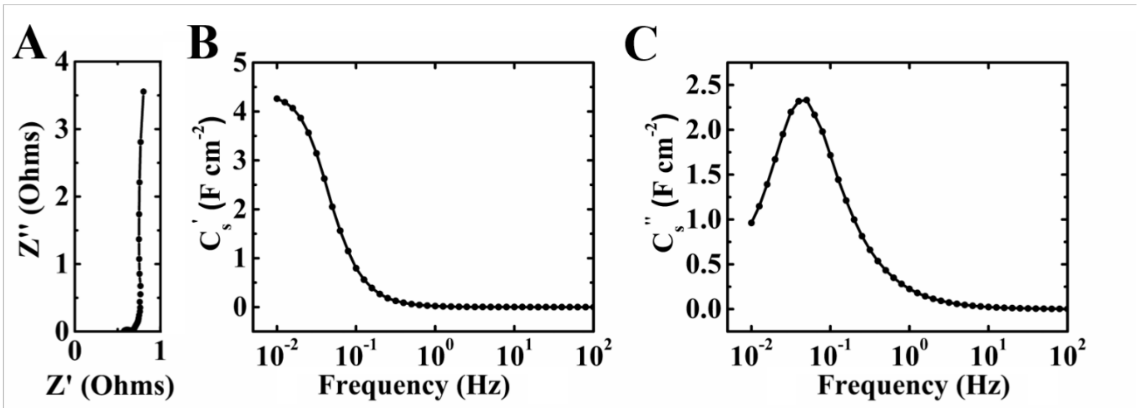

Figure 8-5: (A) Nyquist plot of complex impedance and frequency dependences of (B) C'_s and (C) C''_s calculated from the impedance data for Zn/FeOOH-MWCNT composites.

X-ray diffraction studies revealed information about the crystallinity and phases of the FeOOH and Zn/FeOOH materials. Figure 8-6A is the XRD pattern for the FeOOH electrode material which displays a mainly amorphous pattern exhibiting small broad peaks corresponding to α-FeOOH (JCPDS: 04-015-2898). Figure 8-6B displays the XRD spectra for the Zn/FeOOH sample which presents a mainly amorphous structure with small peaks of a (Fe,Zn)$_3$O$_4$ phase (JCPDS: 01-070-8731).

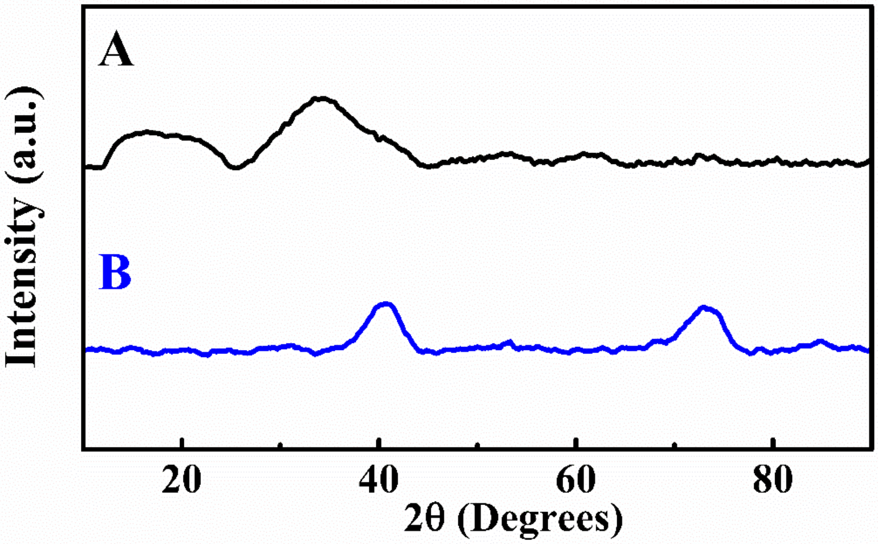

Figure 8-6: X-ray diffraction patterns of (A) FeOOH (B) Zn/FeOOH

The stability of the electrode over 1000 CV cycles at 50 mV s^{-1} is shown in Figure 8-7. It is clear that the addition of Zn has enhanced the cyclic stability of the electrode. Figure 8-3 shows the same minor increase in capacitance over the first 200 cycles as the FeOOH-MWCNT electrode did. This is likely a result of the occurrence of minor microstructure changes during electrochemical cycling as mentioned earlier. However, after 200 cycles the Zn/FeOOH electrode exhibits extremely stable behavior, retaining 98% of its original capacitance after 1000 cycles. The addition of Zn plays a crucial role in the stabilization of the electrode and the proposed mechanism is that Zn provides anodic protection and preferentially dissolves into the electrolyte preventing Fe^{2+} dissolution.

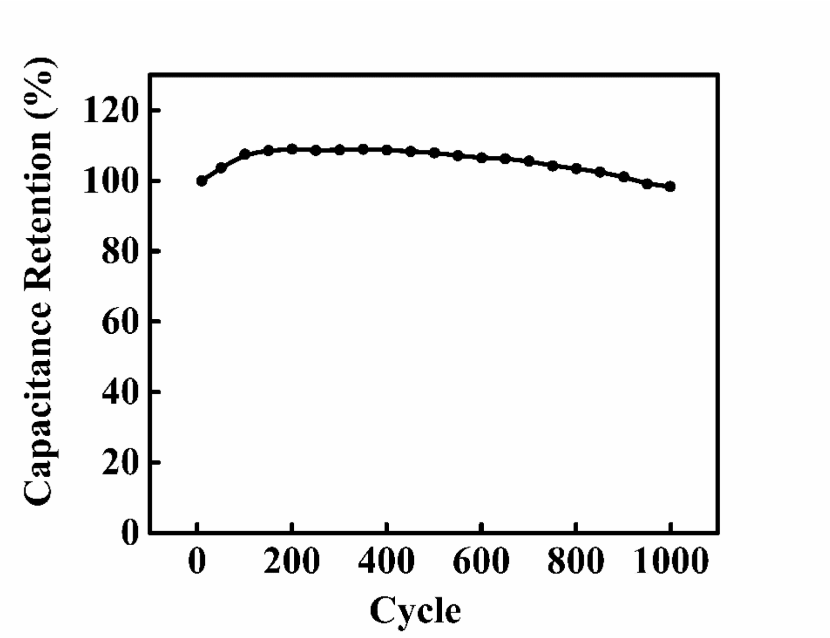

Figure 8-7: Capacitance retention over 1000 CV cycles at 5 mV s^{-1} for the Zn/FeOOH-MWCNT electrode.

8.3 Conclusion

An FeOOH-MWCNT electrode was fabricated and tested in an aqueous neutral electrolyte (0.5M $NaSO_4$) which displayed impressive capacitive behavior as well as low resistance. However, the cyclic stability of this material was less than 70% after 1000 cycles. To enhance the cyclic stability of the electrode, another electrode was fabricated with Zn as a dopant. The Zn/FeOOH-MWCNT electrode presented very similar capacitive properties as well as almost identical impedance results. More importantly, the cyclic stability was significantly improved, retaining 98% of the original capacitance over 1000 cycles.

Chapter 9: Final Conclusions and Future Work

An advanced particle extraction through the liquid-liquid interface (PELLI) technique was used with a versatile extracting molecule, OG. It was found that OG efficiently extracted a variety of materials including oxides, oxyhydroxides, and metals. The use of PELLI avoided the drying stage that occurs in many wet chemical synthesis methods. Electrode materials such as oxides and hydroxide form hard agglomerates when dried which is detrimental to the mixing with conductive additives. The drying of oxides and hydroxides also reduce the surface area of the material, hindering the electrochemical performance. Using OHA as a new extraction molecule, a novel PELLI technique was developed due to its solubility in aqueous solutions at high pH. This innovative method was based on the unique properties of OHA which allows it to be used as an extracting agent as well as a capping agent as it is soluble in alkaline solutions which are used in many chemical precipitation methods. A major finding was that capacitance of Mn_3O_4-MWCNT electrodes was higher than that of MnO_2-MWCNT electrodes using the new PELLI technique. Hydroxamates such as OHA and bufexamac were used to extract ZnO, CeO_2 and FeOOH reinforcing the advanced PELLI method feasibility. A unique feature of hydroxamates was that they show strong adsorption on particles at high pH, despite the electrostatic repulsion of the negatively charged particles and dissociated hydroxamic acids.

In addition, an investigation was started on an advanced negative electrode material for supercapacitors. FeOOH-MWCNT electrodes exhibited high capacitance but low cyclic stability. Zn^{2+} ions were introduced during synthesis forming a doped Zn/FeOOH electrode which showed a significant increase in cyclic stability without negatively impacting other electrochemical properties. More material analysis and characterizations are needed to complete this investigation.

Future studies should include SEM and EDS of the Zn/FeOOH electrode to give a qualitative analysis on the elements and phase present. XPS would provide a difference in Fe^{2+} of the undoped FeOOH electrode before and after cycling. In addition, a PELLI technique could further increase the capacitance of the Zn/FeOOH electrode and other electrochemical properties. Lastly, a device comprised of the Zn/FeOOH electrode and an Mn_3O_4 using the conceptually new PELLI approach should be fabricated and tested.

References

[1] M. Winter and R. J. Brodd, “What Are Batteries, Fuel Cells, and Supercapacitors?,” *Chem. Rev.*, vol. 104, no. 10, pp. 4245–4270, 2004.

[2] T. Chen and L. Dai, “Carbon nanomaterials for high-performance supercapacitors,” *Mater. Today*, vol. 16, no. 7–8, pp. 272–280, 2013.

[3] X. F. Lu, G. R. Li, and Y. X. Tong, “A review of negative electrode materials for electrochemical supercapacitors,” *Sci. China Technol. Sci.*, vol. 58, no. 11, pp. 1799–1808, 2015.

[4] W. H. Jin, G. T. Cao, and J. Y. Sun, “Hybrid supercapacitor based on MnO2 and columned FeOOH using Li2SO4 electrolyte solution,” *J. Power Sources*, vol. 175, no. 1, pp. 686–691, 2008.

[5] W. D. Callister and D. G. Rethwisch, *Materials science and Eng.* 2004.

[6] H. Pan, J. Li, and Y. P. Feng, “Carbon nanotubes for supercapacitor,” *Nanoscale Res. Lett.*, vol. 5, no. 3, pp. 654–668, 2010.

[7] Q. Ke and J. Wang, “Graphene-based materials for supercapacitor electrodes – A review,” *J. Mater.*, vol. 2, no. 1, pp. 37–54, 2016.

[8] D. C. Grahame, “The electrical double layer and the theory of electrocapillarity,” *Chem. Rev.*, vol. 41, no. 3, pp. 441–501, 1947.

[9] B. . Conway, *Electrochemical Supercapacitors-Scientific Fundamentals and Technological Applications*. Springer US, 1999.

[10] J. Cao *et al.*, “Materials and fabrication of electrode scaffolds for deposition of MnO 2 and their true performance in supercapacitors,” *J. Power Sources*, vol. 293, pp. 657–674, Oct. 2015.

[11] V. Augustyn, P. Simon, and B. Dunn, “Pseudocapacitive oxide materials for high-rate electrochemical energy storage,” *Energy Environ. Sci.*, vol. 7, no. 5, pp. 1597–1614, 2014.

[12] Y. Wang, J. Guo, T. Wang, J. Shao, D. Wang, and Y.-W. Yang, “Mesoporous Transition Metal Oxides for Supercapacitors,” *Nanomaterials*, vol. 5, no. 4, pp. 1667–1689, 2015.

[13] Q. Qu, S. Yang, and X. Feng, “2D sandwich-like sheets of iron oxide grown on graphene as high energy anode material for supercapacitors,” *Adv. Mater.*, vol. 23, no. 46, pp. 5574–5580, 2011.

[14] C. Julien and A. Mauger, “Nanostructured MnO2 as Electrode Materials for Energy Storage,” *Nanomaterials*, vol. 7, no. 11, p. 396, 2017.

[15] S.-C. Pang and M. Anderson, “Novel Electrode Materials for Ultracapacitors:Structural and Electrochemical Properties of Sol-Gel-Derived Manganese Dioxide Thin Films,” *MRS Proc.*, vol. 575, no. 2, p. 415, 1999.

[16] S. Wen, J. W. Lee, I. H. Yeo, J. Park, and S. Il Mho, “The role of cations of the electrolyte for the pseudocapacitive behavior of metal oxide electrodes, MnO2 and RuO2,” *Electrochim. Acta*, vol. 50, no. 2–3 SPEC. ISS., pp. 849–855, 2004.

[17] S. Devaraj and N. Munichandraiah, “Effect of crystallographic structure of MnO2 on its electrochemical capacitance properties,” *J. Phys. Chem. C*, vol. 112, no. 11, pp. 4406–4417, 2008.

[18] H. Kanoh, W. Tang, Y. Makita, and K. Ooi, “Electrochemical Intercalation of Alkali-Metal Ions into Birnessite-Type Manganese Oxide in Aqueous Solution,” *Langmuir*, vol. 13, no. 25, pp. 6845–6849, 1997.

[19] T. Brousse, M. Toupin, R. Dugas, L. Athouël, O. Crosnier, and D. Bélanger, “Crystalline MnO[sub 2] as Possible Alternatives to Amorphous Compounds in Electrochemical Supercapacitors,” *J. Electrochem. Soc.*, vol. 153, no. 12, p. A2171, 2006.

[20] C. Hu, Y. Wu, and K. Chang, “Single Crystals : Determinant Influence of Oxidants,” *Chem. Mater.*, no. 15, pp. 2890–2894, 2008.

[21] D. P. Dubal, D. S. Dhawale, R. R. Salunkhe, and C. D. Lokhande, “Conversion of interlocked cube-like Mn3O4into nanoflakes of layered birnessite MnO2during supercapacitive studies,” *J. Alloys Compd.*, vol. 496, no. 1–2, pp. 370–375, 2010.

[22] R. Agrawal, E. Adelowo, A. Baboukani, M. Villegas, A. Henriques, and C. Wang, “Electrostatic Spray Deposition-Based Manganese Oxide Films—From Pseudocapacitive Charge Storage Materials to Three-Dimensional Microelectrode Integrands,” *Nanomaterials*, vol. 7, no. 8, p. 198, 2017.

[23] M. Rajkumar, C. T. Hsu, T. H. Wu, M. G. Chen, and C. C. Hu, “Advanced materials for aqueous supercapacitors in the asymmetric design,” *Prog. Nat. Sci. Mater. Int.*, vol. 25, no. 6, pp. 527–544, 2015.

[24] Y. Zhao, C. Li, F. Li, Z. Shi, and S. Feng, “One-step synthesis of highly water-dispersible Mn3O4nanocrystals,” *Dalt. Trans.*, vol. 40, no. 3, pp. 583–588, 2011.

[25] H. Xu *et al.*, “Synthesis and super capacitance of goethite/reduced graphene oxide for supercapacitors,” *Mater. Chem. Phys.*, vol. 141, no. 1, pp. 310–317, 2013.

[26] R. Barik, B. K. Jena, and M. Mohapatra, “Metal doped mesoporous FeOOH nanorods for high performance supercapacitors,” *RSC Adv.*, vol. 7, no. 77, pp. 49083–49090, 2017.

[27] W. Jin, G. Cao, and J. Sun, “Hybrid supercapacitor based on MnO 2 and columned FeOOH using Li 2 SO 4 electrolyte solution,” vol. 175, pp. 686–691, 2008.

[28] L. Yang, Y. Liu, J. Li, and G. Du, “One-pot hydrothermal synthesis of amorphous FeOOH on Ni foam for high performance supercapacitors,” *J. Alloys Compd.*, vol. 763, pp. 134–140, 2018.

[29] H. B. Li *et al.*, “Amorphous nickel hydroxide nanospheres with ultrahigh capacitance and energy density as electrochemical pseudocapacitor materials,” *Nat.*

Commun., vol. 4, no. May, pp. 1–7, 2013.

[30] L. Cheng, H. Q. Li, and Y. Y. Xia, "A hybrid nonaqueous electrochemical supercapacitor using nano-sized iron oxyhydroxide and activated carbon," *J. Solid State Electrochem.*, vol. 10, no. 6, pp. 405–410, 2006.

[31] C. Zhong, Y. Deng, W. Hu, J. Qiao, L. Zhang, and J. Zhang, "A review of electrolyte materials and compositions for electrochemical supercapacitors," *Chem. Soc. Rev.*, vol. 44, no. 21, pp. 7484–7539, 2015.

[32] A. Cornell, "Ruthenium Dioxide as Cathode Material for Hydrogen Evolution in Hydroxide and Chlorate Solutions," *J. Electrochem. Soc.*, vol. 140, no. 11, p. 3123, 1993.

[33] M. C. Santos, A. J. Terezo, V. C. Fernandes, E. C. Pereira, and L. O. S. Bulhões, "An EQCM investigation of charging RuO2 thin films prepared by the polymeric precursor method," *J. Solid State Electrochem.*, vol. 9, no. 2, pp. 91–95, 2005.

[34] C. D. Lokhande, D. P. Dubal, and O. S. Joo, "Metal oxide thin film based supercapacitors," *Curr. Appl. Phys.*, vol. 11, no. 3, pp. 255–270, 2011.

[35] J. P. Zheng, "Hydrous Ruthenium Oxide as an Electrode Material for Electrochemical Capacitors," *J. Electrochem. Soc.*, vol. 142, no. 8, p. 2699, 1995.

[36] R. Thangappan, M. Arivanandhan, R. Dhinesh Kumar, and R. Jayavel, "Facile synthesis of RuO2nanoparticles anchored on graphene nanosheets for high performance composite electrode for supercapacitor applications," *J. Phys. Chem. Solids*, vol. 121, no. January, pp. 339–349, 2018.

[37] S. Park and S. Kim, "Effect of carbon blacks filler addition on electrochemical behaviors of Co3O4/graphene nanosheets as a supercapacitor electrodes," *Electrochim. Acta*, vol. 89, pp. 516–522, 2013.

[38] L. Wang, X. Liu, X. Wang, X. Yang, and L. Lu, "Electrochemical capacitance study on Co 3O 4 nanowires for super capacitors application," *J. Mater. Sci. Mater. Electron.*, vol. 22, no. 6, pp. 601–606, 2011.

[39] C. Xiang, M. Li, M. Zhi, A. Manivannan, and N. Wu, "A reduced graphene oxide/Co3O4composite for supercapacitor electrode," *J. Power Sources*, vol. 226, pp. 65–70, 2013.

[40] R. Kumar, H. J. Kim, S. Park, A. Srivastava, and I. K. Oh, "Graphene-wrapped and cobalt oxide-intercalated hybrid for extremely durable super-capacitor with ultrahigh energy and power densities," *Carbon N. Y.*, vol. 79, no. 1, pp. 192–202, 2014.

[41] A. M. Abdalla, R. P. Sahu, C. J. Wallar, R. Chen, I. Zhitomirsky, and I. K. Puri, "Nickel oxide nanotube synthesis using multiwalled carbon nanotubes as sacrificial templates for supercapacitor application," *Nanotechnology*, vol. 28, no. 7, 2017.

[42] H. Xiao, S. Yao, H. Liu, F. Qu, X. Zhang, and X. Wu, "NiO nanosheet assembles for supercapacitor electrode materials," *Prog. Nat. Sci. Mater. Int.*, vol. 26, no. 3,

pp. 271–275, 2016.

[43] H. Chai, X. Peng, T. Liu, X. Su, D. Jia, and W. Zhou, “High-performance supercapacitors based on conductive graphene combined with Ni(OH)2nanoflakes,” *RSC Adv.*, vol. 7, no. 58, pp. 36617–36622, 2017.

[44] V. Srinivasan and J. W. Weidner, “Studies on the Capacitance of Nickel Oxide Films: Effect of Heating Temperature and Electrolyte Concentration,” *J. Electrochem. Soc.*, vol. 147, no. 3, p. 880, 2000.

[45] K.-C. Liu, “Porous Nickel Oxide/Nickel Films for Electrochemical Capacitors,” *J. Electrochem. Soc.*, vol. 143, no. 1, p. 124, 1996.

[46] M. S. Yadav and S. K. Tripathi, “Synthesis and characterization of nanocomposite NiO/activated charcoal electrodes for supercapacitor application,” *Ionics (Kiel).*, vol. 23, no. 10, pp. 2919–2930, 2017.

[47] F. I. Dar, K. R. Moonooswamy, and M. Es-Souni, “Morphology and property control of NiO nanostructures for supercapacitor applications,” *Nanoscale Res. Lett.*, vol. 8, no. 1, pp. 1–7, 2013.

[48] Y. Yan, B. Li, W. Guo, H. Pang, and H. Xue, “Vanadium based materials as electrode materials for high performance supercapacitors,” *J. Power Sources*, vol. 329, pp. 148–169, 2016.

[49] Y. Wu *et al.*, “Controlled synthesis of V<inf>2</inf>O<inf>5</inf>/MWCNT core/shell hybrid aerogels through a mixed growth and self-assembly methodology for supercapacitors with high capacitance and ultralong cycle life,” *J. Mater. Chem. A*, vol. 3, no. 30, pp. 15692–15699, 2015.

[50] X. Pan, G. Ren, M. N. F. Hoque, S. Bayne, K. Zhu, and Z. Fan, “Fast supercapacitors based on graphene-bridged V2O3/VOx core-shell nanostructure electrodes with a power density of 1 MW kg-1,” *Adv. Mater. Interfaces*, vol. 1, no. 9, pp. 1–9, 2014.

[51] Z. Liu, H. Zhang, Q. Yang, and Y. Chen, “Graphene / V2O5 hybrid electrode for an asymmetric supercapacitor with high energy density in an organic electrolyte,” *Electrochim. Acta*, vol. 287, pp. 149–157, 2018.

[52] I. Shakir, Z. Ali, J. Bae, J. Park, and D. J. Kang, “Layer by layer assembly of ultrathin V2O5 anchored MWCNTs and graphene on textile fabrics for fabrication of high energy density flexible supercapacitor electrodes,” *Nanoscale*, vol. 6, no. 8, pp. 4125–4130, 2014.

[53] A. Borenstein, O. Hanna, R. Attias, S. Luski, T. Brousse, and D. Aurbach, “Carbon-based composite materials for supercapacitor electrodes: A review,” *J. Mater. Chem. A*, vol. 5, no. 25, pp. 12653–12672, 2017.

[54] Y. Zhu *et al.*, “Carbon-Based Supercapacitors,” *Science (80-.).*, vol. 332, no. June, pp. 1537–1542, 2011.

[55] L. L. Zhang and X. S. Zhao, “Carbon-based materials as supercapacitor

electrodes," *Chem. Soc. Rev.*, vol. 38, no. 9, pp. 2520–2531, 2009.

[56] T. Kim, G. Jung, S. Yoo, K. S. Suh, and R. S. Ruoff, "Activated graphene-based carbons as supercapacitor electrodes with macro- and mesopores," *ACS Nano*, vol. 7, no. 8, pp. 6899–6905, 2013.

[57] S. Pilathottathil, K. K. Thasneema, M. S. Thayyil, M. P. Pillai, and C. V. Niveditha, "A high voltage supercapacitor based on ionic liquid with an activated carbon electrode," *Mater. Res. Express*, vol. 4, no. 7, 2017.

[58] L. Clark, "An asymptotic expansion for the number of permutations with a certain number of inversions," *Electron. J. Comb.*, vol. 7, no. 1 R, pp. 1–11, 2000.

[59] M. Zhi, C. Xiang, J. Li, M. Li, and N. Wu, "Nanostructured carbon-metal oxide composite electrodes for supercapacitors: A review," *Nanoscale*, vol. 5, no. 1, pp. 72–88, 2013.

[60] Z. S. Wu *et al.*, "Anchoring hydrous RuO2 on graphene sheets for high-performance electrochemical capacitors," *Adv. Funct. Mater.*, vol. 20, no. 20, pp. 3595–3602, 2010.

[61] H. Jiang, J. Ma, and C. Li, "Mesoporous carbon incorporated metal oxide nanomaterials as supercapacitor electrodes," *Adv. Mater.*, vol. 24, no. 30, pp. 4197–4202, 2012.

[62] S. Saha, P. Samanta, N. C. Murmu, and T. Kuila, "A review on the heterostructure nanomaterials for supercapacitor application," *J. Energy Storage*, vol. 17, pp. 181–202, 2018.

[63] T. Yumak, D. Bragg, and E. M. Sabolsky, "Effect of synthesis methods on the surface and electrochemical characteristics of metal oxide/activated carbon composites for supercapacitor applications," *Appl. Surf. Sci.*, vol. 469, no. September 2018, pp. 983–993, 2019.

[64] Z. Fan *et al.*, "Asymmetric supercapacitors based on graphene/MnO2 and activated carbon nanofiber electrodes with high power and energy density," *Adv. Funct. Mater.*, vol. 21, no. 12, pp. 2366–2375, 2011.

[65] K. K. Lee *et al.*, "α-Fe 2O 3 nanotubes-reduced graphene oxide composites as synergistic electrochemical capacitor materials," *Nanoscale*, vol. 4, no. 9, pp. 2958–2961, 2012.

[66] B. Gao, C. Z. Yuan, L. H. Su, L. Chen, and X. G. Zhang, "Nickel oxide coated on ultrasonically pretreated carbon nanotubes for supercapacitor," *J. Solid State Electrochem.*, vol. 13, no. 8, pp. 1251–1257, 2009.

[67] B. Zhao *et al.*, "Monolayer graphene/NiO nanosheets with two-dimension structure for supercapacitors," *J. Mater. Chem.*, vol. 21, no. 46, pp. 18792–18798, 2011.

[68] R. T. Vinny, K. Chaitra, K. Venkatesh, N. Nagaraju, and N. Kathyayini, "An excellent cycle performance of asymmetric supercapacitor based on bristles like α-MnO2nanoparticles grown on multiwalled carbon nanotubes," *J. Power Sources*,

vol. 309, pp. 212–220, 2016.

[69] V. D. Nithya and N. S. Arul, “Review on a -Fe 2 O 3 based negative electrode for high performance supercapacitors,” *J. Power Sources*, vol. 327, pp. 297–318, 2016.

[70] X. Wang *et al.*, “RSC Advances Enhancing capacitance of supercapacitor with both a biomass-derived carbon †,” pp. 23859–23865, 2017.

[71] X. Wang, Y. Li, F. Lou, M. E. Melandsø Buan, E. Sheridan, and D. Chen, “Enhancing capacitance of supercapacitor with both organic electrolyte and ionic liquid electrolyte on a biomass-derived carbon,” *RSC Adv.*, vol. 7, no. 38, pp. 23859–23865, 2017.

[72] C. Yuan, “Recent progresses in high-energy-density all pseudocapacitive-electrode-materials-based asymmetric supercapacitors,” vol. 5, no. 20, 2017.

[73] L. L. and Y. W. Faxing Wang, Shiying Xiao, Yuyang Hou, Chenglin Hu, “Advances Electrode materials for aqueous asymmetric supercapacitors,” *RSC Adv.*, pp. 13059–13084, 2013.

[74] K. Wang, S. Gao, Z. Du, A. Yuan, W. Lu, and L. Chen, “MnO2-Carbon nanotube composite for high-areal-density supercapacitors with high rate performance,” *J. Power Sources*, vol. 305, pp. 30–36, 2016.

[75] J. Yang, L. Lian, H. Ruan, F. Xie, and M. Wei, “Nanostructured porous MnO2on Ni foam substrate with a high mass loading via a CV electrodeposition route for supercapacitor application,” *Electrochim. Acta*, vol. 136, pp. 189–194, 2014.

[76] R. Poon and I. Zhitomirsky, “Supercapacitor electrodes with high active mass loading,” *MRS Commun.*, vol. 8, no. 3, pp. 1135–1138, 2018.

[77] C. J. Wallar, R. Poon, and I. Zhitomirsky, “High Areal Capacitance of V_2O_3 – Carbon Nanotube Electrodes,” *J. Electrochem. Soc.*, vol. 164, no. 14, pp. A3620–A3627, 2017.

[78] C. Wallar, D. Luo, R. Poon, and I. Zhitomirsky, “Manganese dioxide–carbon nanotube composite electrodes with high active mass loading for electrochemical supercapacitors,” *J. Mater. Sci.*, vol. 52, no. 7, pp. 3687–3696, 2017.

[79] M. Beidaghi and Y. Gogotsi, “Capacitive energy storage in micro-scale devices: Recent advances in design and fabrication of micro-supercapacitors,” *Energy Environ. Sci.*, vol. 7, no. 3, pp. 867–884, 2014.

[80] O. O. Van der Biest and L. J. Vandeperre, “ELECTROPHORETIC DEPOSITION OF MATERIALS,” *Annu. Rev. Mater. Sci.*, vol. 29, no. 1, pp. 327–352, Aug. 1999.

[81] C. Du and N. Pan, “High power density supercapacitor electrodes of carbon nanotube films by electrophoretic deposition,” *Nanotechnology*, vol. 17, no. 21, pp. 5314–5318, 2006.

[82] S. J. An *et al.*, “Thin film fabrication and simultaneous anodic reduction of

deposited graphene oxide platelets by electrophoretic deposition," *J. Phys. Chem. Lett.*, vol. 1, no. 8, pp. 1259–1263, 2010.

[83] S. Park and R. S. Ruoff, "Chemical methods for the production of graphenes," *Nat. Nanotechnol.*, vol. 4, no. 4, pp. 217–224, 2009.

[84] Y. Wang and I. Zhitomirsky, "Effect of phenolic molecules on electrophoretic deposition of manganese dioxide-carbon nanotube nanocomposites," *Colloids Surfaces A Physicochem. Eng. Asp.*, vol. 369, no. 1–3, pp. 211–217, 2010.

[85] S. N. Pusawale, P. R. Deshmukh, J. L. Gunjakar, and C. D. Lokhande, "SnO2-RuO2 composite films by chemical deposition for supercapacitor application," *Mater. Chem. Phys.*, vol. 139, no. 2–3, pp. 416–422, 2013.

[86] U. M. Patil, K. V. Gurav, V. J. Fulari, C. D. Lokhande, and O. S. Joo, "Characterization of honeycomb-like 'β-Ni(OH)2' thin films synthesized by chemical bath deposition method and their supercapacitor application," *J. Power Sources*, vol. 188, no. 1, pp. 338–342, 2009.

[87] R. S. Mane and C. D. Lokhande, "Chemical deposition method for metal chalcogenide thin films," *Mater. Chem. Phys.*, vol. 65, no. 1, pp. 1–31, 2000.

[88] F. Zhao, W. Huang, and D. Zhou, "Chemical bath deposition synthesis of nickel cobalt oxides/sulfides for high-performance supercapacitors electrode materials," *J. Alloys Compd.*, vol. 755, pp. 15–23, 2018.

[89] Y. Hu, H. Zhu, J. Wang, and Z. Chen, "Synthesis of layered birnessite-type manganese oxide thin films on plastic substrates by chemical bath deposition for flexible transparent supercapacitors," *J. Alloys Compd.*, vol. 509, no. 42, pp. 10234–10240, 2011.

[90] A. Nirmalesh Naveen and S. Selladurai, "Fabrication and performance evaluation of symmetrical supercapacitor based on manganese oxide nanorods-PANI composite," *Mater. Sci. Semicond. Process.*, vol. 40, pp. 468–478, 2015.

[91] P. R. Deshmukh, S. N. Pusawale, V. S. Jamadade, U. M. Patil, and C. D. Lokhande, "Microwave assisted chemical bath deposited polyaniline films for supercapacitor application," *J. Alloys Compd.*, vol. 509, no. 16, pp. 5064–5069, 2011.

[92] Y. Liu, K. Shi, and I. Zhitomirsky, "New colloidal route for electrostatic assembly of oxide nanoparticle - carbon nanotube composites," *Colloids Surfaces A Physicochem. Eng. Asp.*, vol. 446, pp. 15–22, 2014.

[93] A. R. Boccaccini, J. Cho, J. A. Roether, B. J. C. Thomas, E. Jane Minay, and M. S. P. Shaffer, "Electrophoretic deposition of carbon nanotubes," *Carbon N. Y.*, vol. 44, no. 15, pp. 3149–3160, 2006.

[94] M. S. Ata, J. Milne, and I. Zhitomirsky, "Fabrication of Mn3O4–carbon nanotube composites with high areal capacitance using cationic and anionic dispersants," *J. Colloid Interface Sci.*, vol. 512, pp. 758–766, 2018.

[95] R. A. W. Dryfe, A. Uehara, and S. G. Booth, “Metal Deposition at the Liquid – Liquid Interface,” *Chem. Rec.*, pp. 1013–1023, 2014.

[96] R. Chen, R. Poon, R. P. Sahu, I. K. Puri, and I. Zhitomirsky, “MnO 2 -Carbon Nanotube Electrodes for Supercapacitors with High Active Mass Loadings,” *J. Electrochem. Soc.*, vol. 164, no. 7, pp. A1673–A1678, 2017.

[97] R. M. E. Silva, R. Poon, J. Milne, A. Syed, and I. Zhitomirsky, “New developments in liquid-liquid extraction, surface modification and agglomerate-free processing of inorganic particles,” *Adv. Colloid Interface Sci.*, vol. 261, pp. 15–27, 2018.

[98] C. Wallar, T. Zhang, K. Shi, and I. Zhitomirsky, “Synthesis of metal and metal oxide nanoparticles , liquid – liquid extraction and application in supercapacitors,” *Colloids Surfaces A Physicochem. Eng. Asp.*, vol. 500, pp. 195–202, 2016.

[99] R. Chen, Z. Z. Wang, R. P. Sahu, I. K. Puri, and I. Zhitomirsky, “Influence of molecular structure of extractor molecules on liquid-liquid extraction of oxide particles and properties of composites,” *Ceram. Int.*, vol. 44, no. 13, pp. 15714–15720, 2018.

[100] S. Zhang and N. Pan, “Supercapacitors Performance Evaluation,” *Adv. Energy Mater.*, pp. 1–19, 2015.

[101] P. Navalpotro, M. Anderson, R. Marcilla, and J. Palma, “Electrochimica Acta Insights into the energy storage mechanism of hybrid supercapacitors with redox electrolytes by Electrochemical Impedance Spectroscopy,” *Electrochim. Acta*, vol. 263, pp. 110–117, 2018.

[102] Y. R. Ahn, C. R. Park, S. M. Jo, and D. Y. Kim, “Enhanced charge-discharge characteristics of Ru O2 supercapacitors on heat-treated Ti O2 nanorods,” *Appl. Phys. Lett.*, vol. 90, no. 12, 2007.

[103] C.-L. Xu, X.-H. Li, H.-L. Li, D.-D. Zhao, and T. Xue, “Electrodeposition of mesoporous manganese dioxide supercapacitor electrodes through self-assembled triblock copolymer templates,” *J. Power Sources*, vol. 164, no. 2, pp. 953–958, 2006.

[104] V. Subramanian, H. Zhu, R. Vajtai, P. M. Ajayan, and B. Wei, “Hydrothermal synthesis and pseudocapacitance properties of MnO 2 nanostructures,” *J. Phys. Chem. B*, vol. 109, no. 43, pp. 20207–20214, 2005.

[105] and J. W. L. D. Bélanger, T. Brousse, “Manganese Oxides: Battery Materials Make the Leap to Electrochemical Capacitors,” *Electrochem. Soc. Interface*, vol. 17, no. 1, pp. 49–52, 2008.

[106] M. Nakayama, K. Kaneshige, and K. Komine, “Direct Growth of Birnessite-Type MnO 2 on Activated Carbon Cloth for a Flexible Supercapacitor,” *ECS Trans.*, vol. 75, no. 36, pp. 19–32, Jan. 2017.

[107] Y. G. Wang, L. Cheng, and Y. Y. Xia, “Electrochemical profile of nano-particle CoAl double hydroxide/active carbon supercapacitor using KOH electrolyte

solution," *J. Power Sources*, vol. 153, no. 1, pp. 191–196, 2006.

[108] Y. G. Wang, Z. D. Wang, and Y. Y. Xia, "An asymmetric supercapacitor using RuO2/TiO2 nanotube composite and activated carbon electrodes," *Electrochim. Acta*, vol. 50, no. 28, pp. 5641–5646, 2005.

[109] J. Yang, H. Wang, and R. Wang, "Facile synthesis of core–shell FeOOH@MnO2nanomaterials with excellent cycling stability for supercapacitor electrodes," *J. Mater. Sci. Mater. Electron.*, vol. 28, no. 9, pp. 6481–6487, 2017.

[110] L. O'Neill, C. Johnston, and P. S. Grant, "Enhancing the supercapacitor behaviour of novel Fe3O4/FeOOH nanowire hybrid electrodes in aqueous electrolytes," *J. Power Sources*, vol. 274, pp. 907–915, 2015.

[111] M. B. Sassin, A. N. Mansour, K. A. Pettigrew, D. R. Rolison, and J. W. Long, "Electroless Deposition of Conformal Nanoscale Iron Oxide on Carbon Charge Storage," *ACS Nano*, vol. 4, no. 8, pp. 4505–4514, 2010.